Summer 8-2015

Nanostructured Cerium Oxide Based Catalysts: Synthesis, Physical Properties, and Catalytic Performance

Yunyun Zhou
University of Nebraska-Lincoln, yunyun.zhou1986@huskers.unl.edu

nanostructured cerium oxide based catalysts: synthesis, physical properties, and catalytic performance

by

Yunyun Zhou

A DISSERTATION

Presented to the Faculty of

The Graduate College at the University of Nebraska

In Partial Fulfillment of Requirements

For the Degree of Doctor of Philosophy

Major: Chemistry

Under the Supervision of Professor Chin Li “Barry” Cheung

Lincoln, Nebraska

August, 2015

NANOSTRUCTURED CERIUM OXIDE BASED CATALYSTS: SYNTHESIS, PHYSICAL PROPERTIES, AND CATALYTIC PERFORMANCE

Yunyun Zhou, Ph. D.

University of Nebraska, 2015

Advisor: Chin Li "Barry" Cheung

Cerium oxide is an extensively used industrial catalyst with applications as diverse as catalysts for automobile exhaust, petroleum cracking and organic chemicals synthesis. The catalytic activity of cerium oxide is dependent upon its structural properties, especially the oxygen vacancy defects. While recent advances in characterization techniques have dramatically improved our understanding of cerium oxide functionality, many atomic features in cerium oxide contributing to the overall catalytic reactivity are not yet well-understood. This dissertation focuses on the structural studies of catalytically active cerium oxides with different compositions, phases and morphologies, and their utilizations to establish fundamental understandings of cerium oxide based catalyst systems.

Defect sites in reducible metal oxide nanomaterials such as cerium oxide play an important role in their catalytic activities. In this dissertation, nanostructured cerium oxides with different densities of oxygen vacancy defects have been synthesized. High density of oxygen vacancy defects has been shown to promote the dispersion, activity and self-regeneration ability of supported noble metal nanoparticles.

Strong interactions between metal particles and metal oxide supports induce changes in the electronic structures of metal particles, such as oxidation state and valence band structure. Two studies on the strong metal-support interactions, the alteration of oxidation states of supported palladium particles under different redox environments and *s-d* orbital hybridization of supported gold nanoclusters, are presented in this dissertation.

The morphology, size and shape of cerium oxide profoundly affect its reaction performance. Controlling the morphology of nanostructured catalyst allows selective exposure of reactive facets which improve catalytic activity, selectivity, and stability of the catalysts. This dissertation presents a study of the morphological effect of difference cerium oxide support structures on the catalytic activity of supported platinum particles towards alcohol electrooxidation.

Cerium oxide demonstrates catalytic activity of generating reactive oxygen species towards Fenton-like reaction with hydrogen peroxide. This dissertation presents a study of singlet oxygen generation, one of the reactive oxygen species, through hydrogen peroxide decomposition. Chemical trap reagent of singlet oxygen has been demonstrated to exhibit photobleaching under photo-irradiation. The study also includes investigation of kinetics of singlet oxygen generation and elucidation of reaction order with respect to hydrogen peroxide.

ACKNOWLEDGEMENT

First of all, I would like to acknowledge the financial support of funding agencies for my Ph.D. research:

- Army Research Office (W911NF-10–2–0099)
- NSF (CHE-1362916); NSF-EPSCoR (OIA-0701525)
- NASA Center of Advanced Nanoscale Materials (NNX10AQ17A)
- Nebraska Center for Energy Sciences

I gratefully acknowledge my advisor, Dr. Chin Li "Barry" Cheung. His support, guidance and training enable me to complete my doctoral studies at the University of Nebraska-Lincoln. He is an inspiring professor and he always has high standard for research work. I have learned a lot of invaluable research skills and more importantly positive work attitudes from him. I thank my committee members, Dr. Craig Eckhardt, Dr. Rebecca Lai, Dr. Gustavo Larsen, and Dr. Xiao Cheng Zeng for their support, inspiration, encouragement and helpful critiques on my research work.

I also thank my research collaborators: Dr. Yun-Liang Soo and Tai-Sing Wu (National Tsinghua University) for their synchrotron studies, Drs. Wai-Ning Mei, Lu Wang, and Renat Sabirianov (University of Nebraska -Omaha), Drs. Xiao Cheng Zeng and Yi Gao (University of Nebraska-Lincoln) for providing catalyst simulation support, Drs. Peter Dowben, Jing Liu and Lingmei Kong (University of Nebraska-Lincoln) for their helpful guidance in my synchrotron studies, and Dr. Carlos Cabrera, Christian Menedez, Juan Corchado (University of Puerto Rico- Rio Piedras) for their

electrocatalytic studies of my designed catalysts. With their contributions, I can successfully complete my thesis projects and move to the next step of my future.

Furthermore, I am grateful to my current group mates: Neil Lawrence, Zane Gernhart, Chris Marin, Anuja Bhalkikar, Tamra Fisher, and former group members Gonghua Wang, Dr. Mushtaq Dar, Keren Jiang and Hsin-Yu Liu for their help and support. I also thank my undergraduate students, Elizabeth Needels, Jessica Viegas, Michael Kellar, and Dominic Nguyen, who assisted me to accomplish a number of projects.

I would like to thank the UNL Chemistry Department, Nebraska Center for Materials and Nanoscience, and Center for Advanced Microstructure and Devices at the Louisiana State University for the use of their facilities. I am fortunate to learn from many analytical experts and receive their assistance in my research: Drs. You Zhou and Han Chen (Morrison Microscopy Core Research Facility), Johnny Goodwin (University of Alabama), Shah Valloppilly (NCMN), Nancy Bunce (University of North Texas), Jon Shu (Cornell University), Ling Yun Jin (Zhejiang Normal University), Chao Sun and Yanan Li (Beijing Builder Electronic Technology Co., Ltd.).

Finally, I would like to dedicate this dissertation to my beloved family, my parents, my sister and my friends who always trust and support me. They help me make the best decisions. Their love, encouragement and care enable me to finish my doctoral study.

Contents

CHAPTER 1

INTRODUCTION

Rare-earth oxides have been widely explored in catalysis, metallurgy, fuel cells, medical applications and ceramics. Cerium oxide is one of the most important rare earth oxides being actively investigated, especially its use in catalysis.[1] Recent advances in characterization techniques boosted the investigations of physicochemical properties of cerium oxides to improve their activity, selectivity and stability in various applications. However, the structural characteristics corresponding to physicochemical properties are not yet well-understood, which brings difficulties and challenges in designing cerium oxide for various applications.[2] Therefore, it is crucial and necessary to further improve the understanding and establish a solid background of structure-property relationship, and apply the obtained knowledge to design better catalytic systems. These are also the goals in my conducted research studies.

In this dissertation, the detailed studies of synthesis, characterization and catalytic performances of cerium oxide based materials are included to provide understanding of structure-activity relationship and reaction mechanism in different reaction-systems. Two commonly synthetic methods, hydrothermal and precipitation methods, are mainly employed in the synthesis of nanostructured cerium oxide based catalysts. Surfactants are excluded in those methods to avoid their effect on catalytic performance, which allows better analyzing and understanding the catalyst itself in the performance of catalytic reactions. Various techniques are combined to elucidate the physical and chemical properties of catalysts, including phases, lattice structures, chemical oxidation states and atomic environments. The characterization methods including electron microscopy, X-ray

diffraction, X-ray photoemission spectroscopy and X-ray fine structure are applied to analyze the physical properties of catalysts as well as the catalysts' changes during reactions. The structures of catalysts, such as morphology and defects, are probed and correlated with their catalytic performances in conventional and electrochemical reactions. For example, the cerium oxide with high density of oxygen vacancy defects demonstrates high catalytic activity and regenerative ability towards carbon monoxide oxidation. Nanoparticle shaped cerium oxide exhibits stronger interaction with supported noble metal clusters, and outperforms in methanol electrooxidation than that with rod shaped cerium oxide catalyst. Additionally, we also explore our catalysts in the application of radicals-producing reactions. Besides the study of structure-activity relationship, reaction kinetics and pathways have also been investigated utilizing experimental and computational ways.

1.1 Cerium Oxide

1.1.1 General Background of Cerium Oxide

Cerium is a well-known light rare earth element. Elemental cerium was first discovered from a mineral named "cerite" by Jons Jakob Berzelius and Wilhelm Hisinger in Sweden. [1] The rare earths are moderately abundant elements in earth's crust that occur in a large number of minerals. Cerium is the most abundant rare earth, which is even more plentiful than copper. However, the exact values of crustal abundance (average concentration in the earth's crust) are still controversial. For example, Kleber and Love reported 46 ppm for the cerium crustal abundance in 1963, while Jackson and Christiansen gave the value of 70 ppm in 1993; McGill reported a range from 20 to 46

ppm in 1997.[1] The value of 66.5 ppm reported by Lide in 1997, representing the median of the various reported values, was commonly accepted for present discussions.[1]

The rare earths occurring in discrete minerals are in the form of oxides in most cases. The content ranges from 10 to 300 ppm.[3] Light rare-earth metals occur mainly in the minerals of bastnasite (fluorocarbonate form) and monazite (phosphate form). The elemental distribution differs in both minerals and locations. The cerium content in bastnasite is 49.1% with respect to all the rare earth content from Mountain Pass, California, U.S.; while the content is 50.0% from bastnasite located in Bayan Obo, Inner Mongolia, China. In monazite minerals, cerium content is 45.8% at North Staradbroke, Australia and 47% in East Coast Brazil.[4]

Cerium is in the lanthanide group with an atomic number of 58. The electron configuration of cerium is [Xe] $4f^1 5d^1 6s^2$. Cerium has III and IV oxidation states. Cerium (IV) oxide (CeO_2) is an oxide form of cerium metal, usually obtained by heating cerium metal, $Ce(OH)_3$, or any of Ce (III) oxosalts such as oxalate, nitrate or carbonate in air or oxygen.[1] The dioxide CeO_2 has fluorite structure, with a face-centered cubic unit cell and space group of Fm-3m.[5] In each unit cell, the lattice constant is 5.411 Å; each cerium ion is surrounded by eight equivalent oxygen anions, and each anion is tetrahedrally coordinated by four cerium cations. (See Figure 1) The eight coordination sites are alternately empty and occupied by a cerium cation. This clearly shows that there are large vacant octahedral holes in the structure, and this feature plays an important role in the applications of cerium oxide, which will be discussed in sections of 1.1.4 and 1.1.5. The trivalent cerium (III) oxide (Ce_2O_3) also exists under certain conditions. Ce_2O_3 is unstable toward oxidation and is oxidized as pressure increases up to 10^{-40} atm of oxygen, where

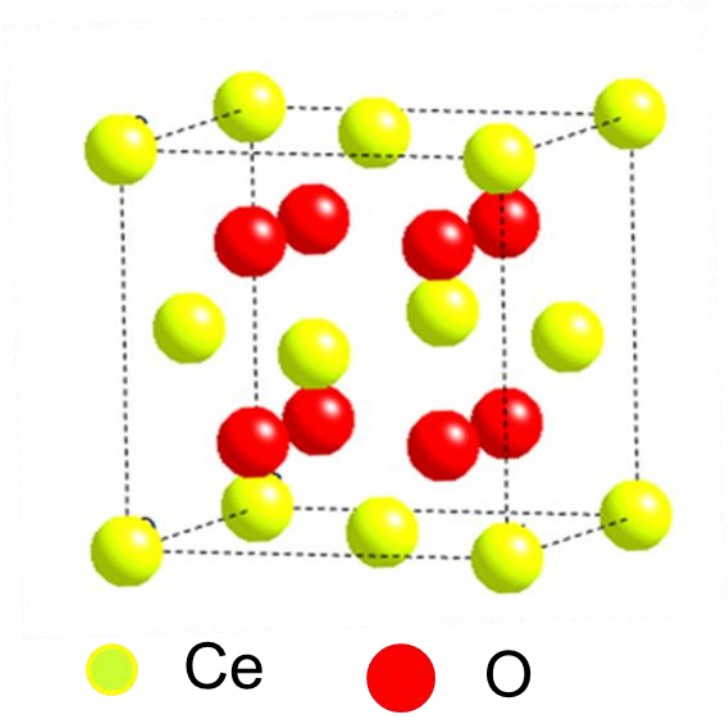

Figure 1.1 Atomic configuration for the unit cell of fluorite-structured CeO_2

CeO_2 starts to form.[5] Other phases of cerium oxide have also been observed and studied at different temperatures using X-ray diffraction. For instance, α-phase cerium oxide, a disordered non-stoichiometric fluorite-related phase, is stable above 685 °C (CeO_x, $1.714<x<2$).[6-8] A so-called β phase with a rhombohedral structure (CeO_x, $1.805<x<1.812$) forms at room temperature, and stays stable until 400 °C. [9, 10]

1.1.2 Morphology

The surface of materials is important in many chemical and physical processes that involve the reaction of inorganic oxides and their environment (adsorbents, temperature, pressure, etc.), such as catalysis and crystallization. Morphology plays a crucial role in influencing the surface properties of materials. Extensive studies have been conducted to unravel the morphology dependent performances of nanocrystals with uniform and well-defined materials. The crystal plane is one of the most common morphological parameters being considered in cerium oxide crystals.

CeO_2 in cubic fluorite structure possesses three low-index planes: (100), (110) and (111). The (100) planes consist of alternating charged planes which introduce a dipole moment perpendicular to the surface. These surfaces are not stable, however, they could be stabilized by defects or by charge-compensating species present, for example, ligands or surfactants. The (110) surfaces are charge neutral with stoichiometric proportions of anions and cations in each plane, which results in no dipole moment perpendicular to the surface. The (111) surfaces also exhibit no dipole moment perpendicular to the surface. Unlike the (110) planes, (111) surfaces consist of a neutral three-plane repeat unit terminated with a single anion plane.[11, 12]

The (111) plane is calculated as the most stable facet irrespective of different potentials used in simulation, both before and after relaxation according to the work done by Vyas.[11] The (110) plane is the next most stable facet, with a surface energy of 1.5 eV from Butler potential calculation while the (100) facet exhibits 2.0 eV of surface energy, the highest one among these three low-index facets.[11] The Butler potential model has the following features: (i) the ions in crystal are assumed to have integral charges. (ii) The short-range interionic forces for anion-anion interactions are calculated from a modified Born-Mayer potential model: $V(r) = Ae^{-r/\rho} - Cr^{-6}$. (iii) Ionic polarization is treated with a shell model.

Similar results have been obtained from Fronzi *et al*. They performed density functional theory (DFT) investigations on the three low-index surfaces of CeO_2. Different terminations including surface defects were also considered in their calculations. The most stable surface structure is the stoichiometric (111) surface under oxygen- rich conditions with a surface free energy of 0.060 eV/ $Å^2$ using the approach of "ab initio atomistic thermodynamics". In a reducing environment, the (111) surface with subsurface oxygen vacancies has been found to be the most stable one with a surface free energy of -0.001 eV/ $Å^2$. While in a highly reducing environment, a Ce-terminated (111) surface is the most stable one.[13] CeO_2 (110) surface with surface oxygen vacancies has 0.012 eV/ $Å^2$ surface free energy, which is 0.006 eV higher than CeO_2 (111) surface with same oxygen vacancies. The surface free energies of CeO_2 (100) surface having the same type and amount of surface oxygen vacancies terminated with oxygen and cerium are 0.575 and 0.016 eV/ $Å^2$ respectively, which are both larger than those of CeO_2 (111) and CeO_2 (110) surface.[13] Thus, with similar surface structures (*e.g.* defects) of cerium oxides,

although the ceria surfaces are calculated with different methods, the CeO_2 (111) surface stays as the most stable one, followed by (110) and (100) surfaces.

Other crystal planes of cerium oxides, such as (200), (220), (331) planes, etc., have also been investigated and characterized in both experimental and simulation studies.[11, 14] For example, {220} facets were found in a slightly truncated cerium oxide nanocubes with predominate (100) facets synthesized by Kaneko *et al*.[14] Sayle and co-workers reported the surface energies of 11.577 and 2.475 J/m^2 for (331) planes before and after relaxation through applying energy minimization code MIDAS.[12] Moreover, recent advances in materials science have improved the feasibility of tailoring the metal oxide morphology, and the desired crystal facets of the cerium oxide materials can be preferentially exposed through precise control of the growth kinetics.[5] However, these three low-index planes are the most commonly observed and the most studied facets on synthesized cerium oxide structures. They illustrate the facet functions in different applications of cerium oxides representatively. Thus only the three low-index surfaces are considered here and will be discussed in details in later chapters.

1.1.3 Nanostructures

The applications of nanostructured cerium oxides grow rapidly in different areas, including catalysts, fuel cells and microelectronics, reflecting their importance in enhancing the performances of those systems.[16-19] In these applications, various shapes of ceria nanoconstructs have been explored, for example, cubes, rods, octahedron, polyhedron, tube, etc. Ceria nanocrystals with different shapes possess different crystal

planes and surface properties, which can affect the interactions between the ceria surface and adsorbed molecules, and hence influence the performances in different systems.

Ceria nanocubes usually have exposed (100) facets on the surface according to transmission electron microscopy studies.[20, 21] Due to the high surface energy of (100) crystal planes, trace amounts of irregular shaped nanoparticles with (111) planes are usually formed during the process of hydrothermal growth and high temperature calcination.[20] However, ceria nanocubes exposing (100) facets with uniform size and well-defined shape can be achieved by using a surfactant (eg. tetramethylammonium hydroxide) in the synthetic procedures to decrease the surface energy.[21] Synthesis of ceria nanocubes is highly desirable because facets with high surface energies usually exhibit preferable activities due to the unsaturated coordination atoms, atomic steps and ledges.[22-24]

Ceria nanorods have gained extensive interest due to their tremendously higher activities than those of ceria with other shapes in many different reactions, such as CO oxidation, NO reductions and 1,2-dichloroethane and ethyl acetate oxidation.[25-27] The dominant planes exposed on ceria nanorods are (111) planes reported by several groups from literature.[20, 28] A few (100) planes were also observed in the materials synthesized by Wang et al. for catalytic conversion of CO_2 with methanol.[20] However, due to different synthetic procedures, ceria nanorods might expose other different facets on the surface. Mai and co-workers found that their as-synthesized ceria nanorods showed {100} and {110} crystal planes with a preferred growth direction along [110]. Those ceria nanorods demonstrated high oxygen storage capacity than that of their polyhedra and cubes counterparts due to the higher fraction of more reactive {100} and {110} planes.[29]

Ceria octahedra have been widely used and attracted much attention due to the dominant (111) planes exposed on their surfaces.[20] Various methods have been reported to synthesize this specifically morphological ceria, either with or without surfactant. With the most stable (111) planes on the surface, ceria octahedra demonstrated the least catalytic activity being studied when compared to the activities of nanocubes, nanorods and other shapes in many reactions, such as CO oxidation and ethyl acetate oxidation.[20, 27] Truncated octahedral nanocrystals with eight {111} and six {100} facets exposed have also been successfully synthesized with capping agent of polyvinyl pyrrolidone.[21]

Nanostructured ceria with other morphologies, such as nanotubes, spindles, nanosheets, etc. have been synthesized for particular usages.[20, 30, 31] Remarkable progress has been made to achieve these ceria nanomaterials. However, synthesizing these morphological nanostructures with well-controlled size and uniformity is still difficult due to their uncommon shapes. For example, it is difficult to prepare nanosheets due to their exceptionally small thickness and possible quantum size effects.[32] Fluorite-structured ceria nanotubes have been synthesized by controlled annealing of layered $Ce(OH)_3$ nanotubes and can possess the nanotubular morphology only in the presence of structural defects.[33] More efforts are still needed to develop these uncommonly shaped materials with well-controlled size and shape in the future.

1.1.4 Oxygen Vacancy Defects (OVDs)

Cerium oxide has a fluorite structure, with space group of Fm-3m. The intrinsic defects are present due to the alternative occupation and absence of cerium cation in the eight coordination sites. Those defects can also be created by reaction with solid or atmosphere.[5] Three different types of internal/subsurface defects observed in ceria

include Frenkel (cation) defect, anti-Frenkel (anion) defects, and Schottky defect. Frenkel (or interstitial) defect forms when an atom or ion leaves its place in the lattice, occupies an interstitial site in a nearby location and creates a vacancy at original site. While Schottky defect forms when oppositely charged ions leave their lattice sites, creating vacancy sites and these vacancies are formed according to stoichiometric units, to maintain an overall neutral charge in the ionic solid. (see Figure 1.2[34]) In ceria, the energies of cation Frenkel defects (8.86 eV/per defect) and Schottky defects (3.33 eV) are higher than that of the Frenkel oxygen defects (2.81 eV), hence the most likely form of intrinsic disorder is Frenkel-type oxygen defects.[35] This is widely accepted from the experimental studies.[36-38] For instance, Steele and Floyd reported that the predominant defects in ceria and yttria-doped ceria are anion vacancies;[39] Faber *et al.* concluded that the amount of interstitial Ce defects was less than ~ 0.1% of the total defect concentration in $CeO_{1.91}$.[40]

Anion Frenkel-type oxygen defects lead to the formation of pairs of oxygen vacancies and oxygen atoms in interstitial positions. Generally, these defects do not change the stoichiometric composition and usually have a low concentration. However, ceria can form a high concentration of vacancy defects by removing oxygen ions under reducing environment, which induces the stoichiometry change from CeO_2 to CeO_{2-x} ($0 < x < 0.5$). In this case, the created oxygen vacancies need to compensate the negative charges formed during removing oxygen. After removing the oxygen from CeO_2 lattice, the left electrons are associated with the charge change of two cerium atoms from +4 to +3. The process is illustrated in the following equation.

$CeO_2 \rightarrow CeO_{2-x} + x/2\ O_2\ (g)\ (0 < x < 0.5)$

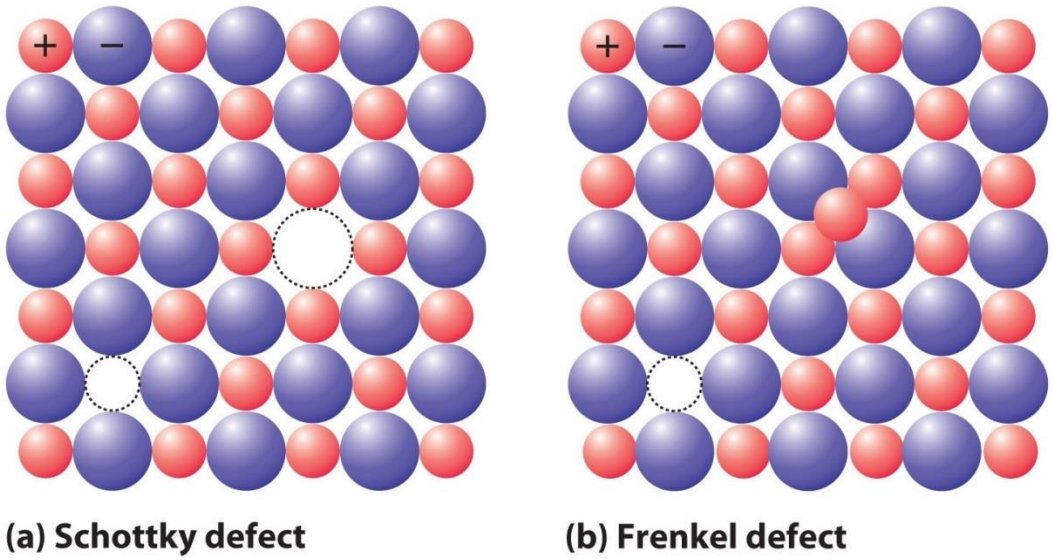

Figure 1.2 Differences between a Schottky defect and a Frenkel defect in a lattice.[34]

This defect forming process can also be written using the expressions below: [2]

$CeO_2 \rightarrow 2x\ Ce'_{Ce} + (1-2x)\ Ce_{Ce} + x\ V_{Ö} + (2-x)\ O_O + 0.5x\ O_2\ (g)$

In this reaction, x moles of atomic oxygen are removed from the CeO_2 lattice, leaving oxygen vacancies and (2-x) O^{2-} anions at their original sites. To maintain electroneutrality, 2x moles of Ce^{3+} (Ce'_{Ce}) will be formed and the remaining1-2x moles of Ce cation are kept being Ce^{4+} (Ce_{Ce}).[5] In undoped ceria, the concentration of oxygen defects [$V_{Ö}$] (only valid for very low concentrations) is proportional to $P(O_2)^{-1/6}$ (P-pressure).[41]

Oxygen vacancy defects (OVDs) of ceria enable ceria act as an oxygen buffer to store oxygen under oxygen-rich environment and release oxygen under oxygen-lean environment. This unique property is due to the interchange of oxidation states Ce^{4+} and Ce^{3+} coupled with OVDs formation. This property is also called oxygen storage capacity, which has been proved to positively correlate to the activities of catalysts/electrolytes in automobile emissions treatment systems and solid oxide fuel cells.[2, 16, 18] Another important role of OVDs in ceria played in catalysis is to promote supported noble metals' activity and dispersion.[16, 18 42] Both phenomena have strong correlation with the type, size and distribution of OVDs.[43]

The size, type and distribution of OVDs on CeO_2 (111) surface have been studied by Esch *et al.* utilizing high-resolution scanning tunneling microscopy (STM) and density functional theory (DFT) calculations.[43] Single and clustered vacancies have been observed both in surface and subsurface. Single vacancies have two types. One is surface oxygen vacancy appearing as depressions surrounded by three oxygen-pair lobes

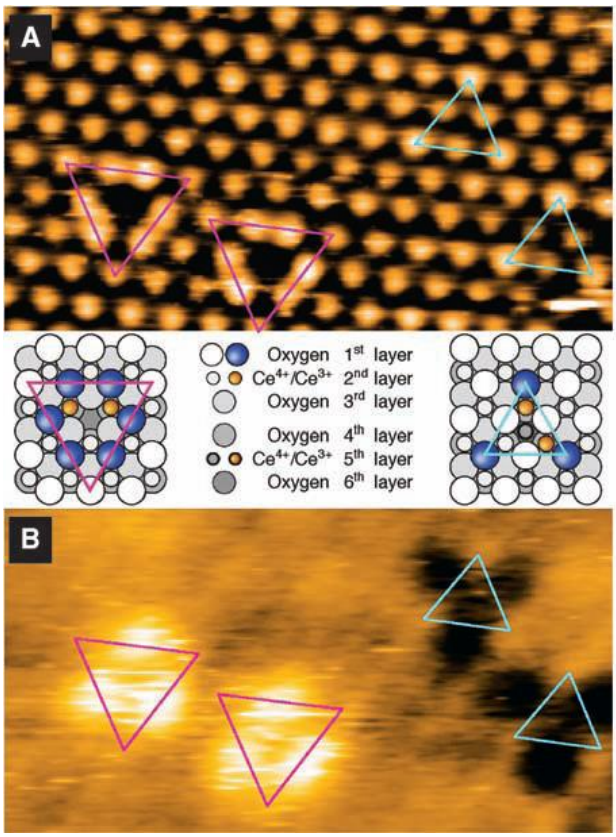

Figure 1.3 (A) Filled-state and (B) empty-state STM images of single vacancies and related structural models (left, surface vacancy; right, subsurface vacancy; characteristic O rim atoms in blue). (From reference [43], reprinted with permission from AAAS)[43]

(magenta triangles). (See Figure 1.3.A) The other type is subsurface oxygen vacancy which appears as triple oxygen-protrusions (cyan triangles) centered around third-layer oxygen sites. (See Figure 1.3.B) The superposition of a surface vacancy and a subsurface vacancy can form a vacancy dimer, which is the only observed vacancy dimer. Single vacancies are dominant at slightly reduced surfaces. Clustered vacancies only occupy 1.5% and 1.3% of the vacancies at surface and subsurface, respectively.[43]

At higher reduced surfaces, clustered vacancies are the dominant ones with a percentage of 68%, and 92% of those are linear surface oxygen vacancies (LSVC).[43] (See Figure 1.4) Each LSVC has two oxygen atoms facing each other, one appearing 0.1 Å below and the other one protruding 0.1 Å above the surface. Both atoms shift towards the inside of the OVD. The double LSVC has a dimer of surface vacancies and one subsurface vacancy, forming a trimer vacancy with Ce^{3+} ions coordinated to the defect. Triangular surface oxygen vacancy trimers are the next most abundant OVDs after LSVC, with exposing Ce^{3+} ions only.[43]

Oxygen vacancy defects also induce the highly mobile lattice oxygen migration involved in the oxidation process, which corresponds to the electrical conductivity of ceria. Actually both electronic and ionic conduction contribute to the total conductivity of ceria and enables ceria as a mixed conductor. However, since the electron mobilities are generally orders of magnitude greater than ionic mobilities, the non-stoichiometry induced by OVDs formation does not lead to mixed conduction.[44] An OVD creates a small polaron where the electrons are trapped at Ce^{3+} lattice sites and can only move to adjacent sites by a hopping process similar to ionic diffusion. This results in dramatically reduced electron conductivities, which has an order of 10^{-4}-10^{-2} cm^2/V Sec.[2, 45]

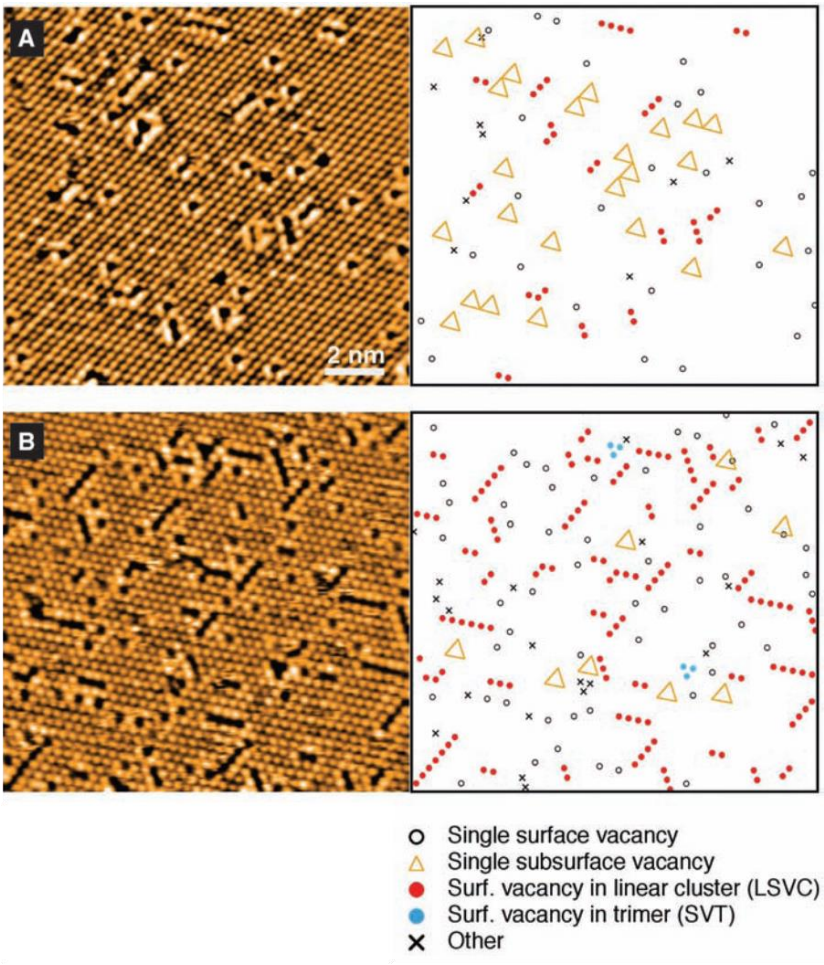

Figure 1.4 (A and B) STM images of the CeO_2(111) surface obtained after 1 min (A) and 5 min (B) of annealing at 900-C, with corresponding representations of the observed defects. (From reference [43], reprinted with permission from AAAS)[43]

1.1.5 Applications

Cerium oxide based materials have been applied in numerous areas, including catalysis, ceramics, fuel cells, glass, and phosphors.[1, 5] All these applications are based on its potential redox chemistry between Ce^{3+} and Ce^{4+}, high oxygen affinity and absorption/ excitation energy bands associated with electronic structure.

The redox property and Lewis acid and base sites on ceria make this oxide suitable as a catalyst or a support for chemical reactions. Ceria is an important ingredient in three-way catalysts for catalytic converters to convert the toxic gases in automobile emissions to less or non-toxic ones. Due to its oxygen storage and release capability, ceria can oxidize the toxic carbon monoxide to less toxic carbon dioxide, oxidize the unburnt hydrocarbons to carbon dioxide and water, and help reduce NO_x to N_2 gas. In catalytic converters, ceria also acts as a stabilizer for high surface area support alumina[1] and a sintering-resistant support for noble metals. It helps noble metal dispersion on its surface and provides oxygen to the supported metal particles for oxidizing the adsorbents.[5] The high density of OVDs in ceria is helpful to increase its catalytic activity towards automobile emission mitigations. Recently, we discovered that OVDs also assisted the self-regeneration ability of supported palladium clusters. The ceria nanorods with higher density of OVDs helped the reoxidation of palladium metallic clusters to palladium oxides, which were proved as the active sites for CO oxidation.[18]

Ceria's weak Lewis acid and stronger Lewis base property allows it to be used in reactions of organic synthesis, for example, dehydrogenation of glycerol, carbonate synthesis, C-C coupling reactions and so on.[5] Recently, Cheung's group discovered the bifunctional catalytic activity of ceria nanorods towards the cyanosilylation of aldehydes using trimethylsilyl cyanide. Ceria nanorods exhibited 99% conversion of aldehydes to

the expected products in 3 h, which was much higher than those of bulk ceria and ceria nanoparticles due to the higher density OVDs possessed in ceria nanorods.[46] Tamura *et al.* reported high selectivity and yield of cyclic carbonate from direct conversion of CO_2 and diols using ceria catalysts. CeO_2-ZrO_2 catalysts demonstrated > 99% selectivity after 2h reaction at 423 K. CeO_2 in the mixed oxides was suggested as the main active species in the reaction due to its positive correlation between the product and the content of Ce in catalyst at reaction temperatures of 673 K and 873 K.[47]

Ceria performs as the best polishing agent for most glass compositions.[48] A significant portion of cerium products are applied in polishing industry annually.[49] Nano ceria with different sizes and size distributions (eg. 30-50 nm,[50] and 10-80 nm[51]) have been synthesized and investigated for shallow trench isolation chemical mechanical polishing. Among those synthesis, Tsai reported a very simple powder synthesis method of cerium oxide with grain size of ~8nm via homogeneous precipitation under normal pressure, which was considered advantageous than previous methods. The best polishing performance of this nano grade ceria was 2258 Å/min for oxide film and 220 Å/min for nitrite.[52]

Ceria is of interest as a material for solid oxide fuel cell (SOFC) due to its decrease of internal electrical resistance in an SOFC. The internal resistance comes from both electrolyte, and the fuel and air electrode. Ceria-containing fuel electrode has lower susceptibility towards coke formation and is less sensitive to the fuel impurities such as sulfur. Oxygen vacancies are essential for ceria possessing these properties. Doped ceria has been reported as a low-temperature electrolyte for about fifty years, such as Ce_{1-}

$_yGd_yO_{2-y/2-x}$, and $Ce_{1-y}Sm_yO_{2-y/2-x}$. Around 500-650 °C in SOFC, ceria doped materials have high oxygen ion conductivity which enables ceria act as a good electrolyte.[5]

1.2 Synthetic Methods for Cerium Oxide Nanostructures

Nanostructured ceria materials exhibit different physicochemical properties compared to their bulk counterpart due to their large surface areas, small sizes, relatively higher densities of OVDs, quantum size effects, etc.[5, 53-55] Synthesis of nanostructured ceria has garnered intensive interest and investment during the past two decades. The synthetic methods are divided into two categories: chemical and physical methods. The chemical methods include hydrothermal, co-precipitation, sol-gel, microwave, combustion methods and so on. Ball milling is the major physical method.[5, 55] The chemical methods, such as hydrothermal, co-precipitation and sol-gel methods, are the most common methods in producing ceria nanoparticles for catalytic applications. In the present chapter, these three methods will be addressed and discussed.

1.2.1 Hydrothermal Synthesis

Hydrothermal method refers to the oxide synthesis and crystal growth in aqueous solutions under high temperature and pressure using a sealed heated vessel which is known as autoclave. It is one of the most important and well-established methods for the laboratory and industrial scale synthesis of nanoceria materials. Two big advantages of this method are that: The reaction temperature is below the melting point of reactants, and the operational parameters such as reaction temperature, duration, autoclave types can be easily tuned to modify the reactivity of synthesize inorganic solids.[5]

In our lab, we have applied hydrothermal method to synthesize different morphologies of ceria nanomaterials. We synthesized ceria nanorods from $Ce_2(SO_4)_3 \bullet xH_2O$ and NaOH reactants utilizing a Parr autoclave with 50 ml Teflon liner at 120 °C for 15 h.[28] $Ce(OH)_3$ nanorods were formed after the hydrothermal treatment. After filtration, drying and calcination processes, $Ce(OH)_3$ turned into fluorite structured CeO_{2-x} nanorods characterized by X-ray diffraction (XRD) and transmission electron spectroscopy (TEM). (See Figure 1.5a) By using the same type of autoclave, ceria nanocubes were successfully prepared from $Ce(NO)_3 \bullet 6H_2O$ and NaOH precursors at 180 C° for 24 h. The hydrothermal step led to the precipitation of ceria in white powder. Further steps of centrifuge, washing with water and ethanol, and drying were performed to finalize the product. Figure 1.5b shows the TEM images of resulting ceria nanocubes. Ceria nano-octahdedra were obtained from $Ce(NO)_3 \bullet 6H_2O$ and trace amount of Na_3PO_4 mixtures heated at 170 °C for 8 h. (See Figure 1.5c) The synthesized ceria octahedral exposed (111) facets on its surface according to TEM studies. [20, 27]

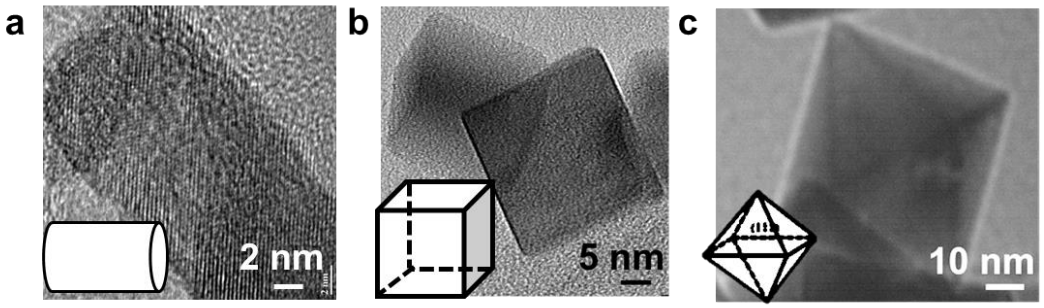

Figure 1.5 TEM images of ceria nanomaterials with different shapes of (a) rod, (b) cube, and (c) octahedron.

The control of shape and particle size together with uniformity is challenging with hydrothermal method. Surfactant is usually introduced to improve the morphological properties. Wang and co-workers developed a facile hydrothermal method to synthesize ceria nanocubes with six {100} facets with oleic acid as the surfactant. The as-prepared ceria were single crystalline, confirmed by uniform crystal lattice fringes. The sizes were well controlled with side lengths from 9 to 17 nm.[21] Vantomme *et al.* applied a cheap and easy-available surfactant cetyltrimethylammonium bromide (CTMABr) in their direct growth and aggregation of crystalline ceria nanorods. The as-synthesized ceria nanorods were single crystalline with uniform diameters of 10- 25 nm and lengths ranging from 150 – 400 nm. The nanorods formation mechanism assisted by CTMABr was also investigated and discussed. The cationic surfactant $CTMA^+$ was proposed to incorporate into the $Ce(H_2O)_x(OH)_y^{4-y}$ complex formed from Ce^{4+} under basic conditions at the beginning, after the pH value reached above the isoelectric point (7-8) of hydrous CeO_2. Colloidal ceria nanoparticles with surfactant capsules were then generated when the solution pH increased to a certain value. Subsequently, a bilayer of ceria/surfactant was formed under autoclaving conditions due to the interchain attraction, flocculation and coalescence of these inorganic/organic composites. The bilayer drove the orientation growth of ceria nanorods. Moreover, CTMA+ capsules also restricted the size regularization of nanorods, which contributed to the uniformity of as-prepared materials.[56]

1.2.2 Co-Precipitation Synthesis

Co-precipitation synthetic method is another extensively used approach for preparing nanomaterial. This method has typical advantages: (i) simple and rapid

preparation process (ii) easily controllable particle size and composition, and (iii) flexible in modifying the particle surface state and overall homogeneity.[15] In general, this method requires two salts precursors dissolved in aqueous solutions, and the desired product precipitates out of the solution after the pH was adjusted to a certain value, which varies depending on the desired materials.[5] The cerium precursors are usually inorganic cerium salt, such as $Ce(NO_3)_3$, $CeCl_3$, $(NH_4)_2Ce(NO_3)_6$, and the precipitating agents are generally NaOH, NH_4OH, hydrazine and oxalic acid.[57-60] The concentration of precursors, reaction temperature, pH and rate of addition of precipitating agent are the main factors influencing the particle size and morphology of ceria nanoparticles.

In the synthesis of mixed oxides, due to the differences in solubility of several precipitating phases, the precipitation of each metal ion component has different precipitation kinetics and brings difficulties in controlling the homogeneity of mixed fine particles. To achieve high homogeneity, the solubility of all the precipitate components should be close. To overcome the difficulty of controlling particle size, template-assisted co-precipitation, redox co-precipitation, carbonate co-precipitation etc. have been introduced in conventional co-precipitation method.[5, 61] For example, Abimanyu and co-workers utilized ionic liquid as a template to prepare magnesium and cerium mixed oxides. It was found that the surface area and particle size were dramatically improved using this template. In addition, ionic liquids also increased the surface basicity of the particles, which was important to affect the catalytic activity towards ethylene carbonate conversion and dimethyl carbonate yield.[61]

1.2.3 Sol-Gel Synthesis

Sol-gel method is widely used in ceramics industry and materials science for producing solid materials such as ceramic fibers and dense films. The method is highly suitable for the fabrication of metal oxides. It is easy to perform and does not need any special conditions.[5] Metal alkoxide and metal chloride are typical precursors. The process involves conversion of metal alkoxide/chloride solution into a colloidal suspension (sol) and gelation of the sol to form discrete particles or network polymers in a continuous liquid phase (gel).[62] The particles in the sol are amorphous or crystalline and particle aggregation is prevented by electrostatic repulsion. The particle size depends on the temperature, pH, and solution composition etc. The morphology, size and chemical property of final product are strongly correlated to the hydrolysis, condensation and drying conditions. The relative rates of hydrolysis and condensation greatly affect the gel quality. For example, relatively slow rates of hydrolysis and condensation result in colloids/ sol. Slow hydrolysis rate and rapid condensation rate cause controlled precipitation. Polymeric gels tend to form in a fast hydrolysis rate and slow condensation rate. Either colloidal gel or gelatinous precipitate is produced if both hydrolysis and condensation rates are fast.[63]

Drying process is another important step that affects the physicochemical properties of as-synthesized materials. Shrinkage and densification usually take place accompanied with drying at low temperature treatments (25-100 °C).[64] This results in the formation of xerogel. Xerogel often has small surface area and low pore volume, which is not suitable for catalytic applications. Another different sol-gel material called aerogel

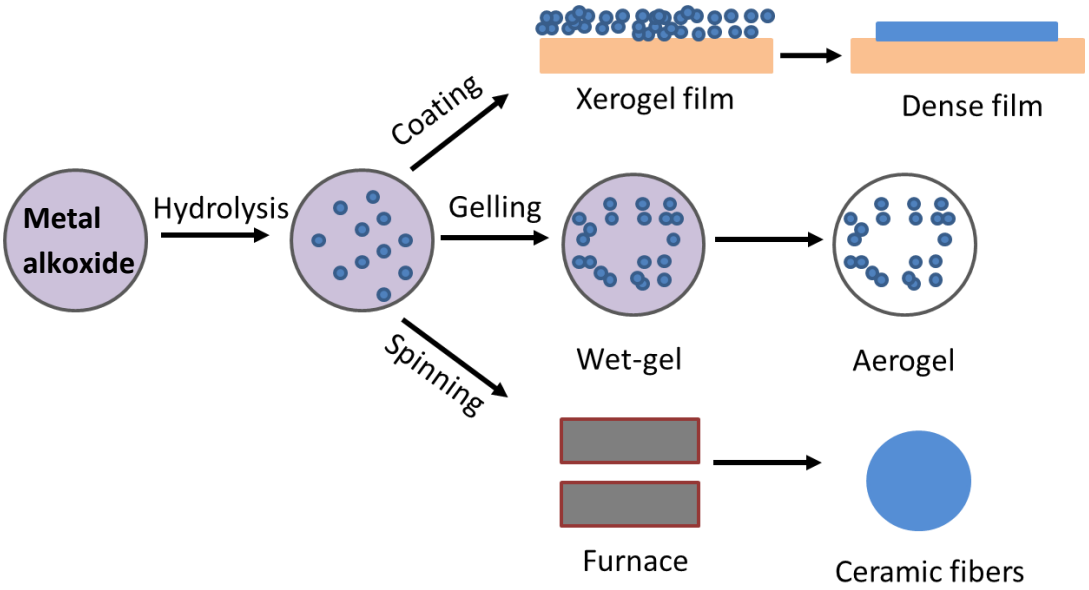

Figure 1.6 Schematic representation of the different stages and routes of the sol-gel technology.[64]

will be obtained if supercritical drying process is employed. There is no liquid/vapor interface and therefore no capillary-force-drive collapse or shrinkages will happen. Various materials can be synthesized from sol-gel method, which is illustrated in Figure 1.6.[5, 64] Darroudi *et al*. reported synthesizing cerium oxide nanoparticles via sol-gel method in gelatin media. The metal precursor is cerium nitrate $Ce(NO_3)_3$. The hydrolysis was performed using ammonia solution. Long-chain gelatin was utilized to terminate the growth of ceria nanoparticles and stabilize them. The as-prepared ceria exhibited a cubic fluoride structure with sizes less than 10 nm.[65]

1.3 Physical Characterization Techniques

Metal oxides have grown rapidly in their applications in various areas, especially in catalysis. This necessitates deep understandings of metal oxide in these applications to further optimize the materials and thus achieve better performances. Recent advances in characterization techniques enable us to improve our understanding of metal oxide structures and the processes occurring on the surface and in the bulk. A number of modern physical techniques are used to characterize metal oxides, ranging from probing the interaction of metal oxides with probe molecules to *in-situ* and *ex-situ* surface characterization and structural elucidation.[66]

1.3.1 Transmission Electron Microscopy

Transmission electron microscopy (TEM) is one of the most active research fields in solid state and materials science. The principle of TEM is that electrons emitted from electron gun are accelerated and focused to form a parallel beam. The electron beam interacts with specimen and created different forms of energy. The most useful energy forms for TEM are transmitted electrons, elastically/inelastically scattered electrons.[67]

High Resolution TEM (HRTEM) uses under-focus conditions which overcome the lens defect effect, and has been essential in study the structures of solid oxides. The resolution of HRTEM can reach to 800,000 × to 1,500,000 × magnification. High energy electron has strong interaction with specimens. Diffraction and phase contrasts are the two formation mechanisms for HRTEM image contrast. Diffraction contrast is widely used to investigate the locations and defects in crystals due to the different Bragg angles in defect area to the perfect crystal bulk. The phase contrast can be enhanced by defocusing.[67] HRTEM surface profile imaging provides surface structural information, such as lattice fringes, facets, defects, etc. We have utilized HRTEM to investigate approximate locations of defects on ceria surface in our lab. Different types of defects, point and linear OVDs, were observed in ceria nanorods.[28] (See Figure 1.7)

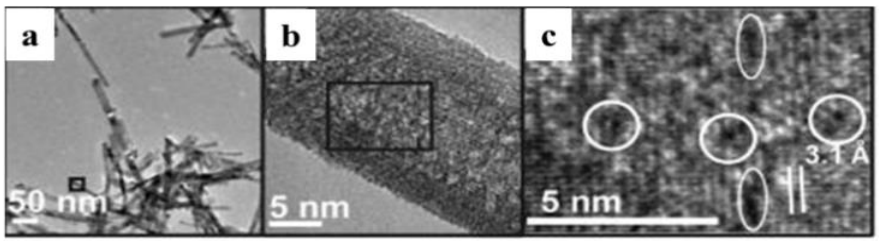

Figure 1.7 (a) Typical TEM image of ceria nanorods. (b) HRTEM images of individual nanorods. Squares in the figure (b) show approximate zoomed-in area of interest for adjacent figure to the right. (c) The approximate locations of some oxygen vacancy defects (OVDs). Point OVDs (circles) and linear OVDs (ovals). (reprinted with permission from American Chemical Society)[28]

1.3.2 X-ray Diffraction

X-ray diffraction (XRD) is a useful tool to identify the atomic and molecular structure of a crystal, where the crystalline atoms cause the incident beam X-rays to diffract and interferences occur. XRD can be used to measure the spacing between layers or rows of atoms, to determine the crystal orientation, strain and grain sizes, and to identify the crystal structures of unknown species.[68]

The basic physical principle of XRD is Bragg's law, which was developed by English physicists W. H. Bragg and his son W. L. Bragg. Incident X-ray interacting with atoms in crystals can be scattered, producing elastic scattering. If the scatterers are arranged symmetrically with a separation *d*, the constructive interference of scattered waves only happen in the directions where their path distance difference $2d \sin\theta$ is *n* (*n*= integer numbers) times of the wavelength λ. Thus, Bragg's law is written as (See Scheme 1.1)

$$2d \sin\theta = n\lambda$$

d - lattice spacing; θ- incident beam angle; λ- X-ray wavelength.[69]

We utilized XRD to determine the structure and lattice parameters of cerium oxide nanorods synthesized in our lab. The nanoceria materials are multicrystalline and consistent with fluorite phase of CeO_2. The broad peaks demonstrate nanocrystalline nature of ceria particles. The grain size of ceria nanorods activated at different temperatures increases as the temperature increases, for example, the grain size of ceria activated at 400 °C is 8.17 nm, while the one activated at 1000 °C is 43.3 nm according to the Scherrer's formula. (See Figure 1.8)

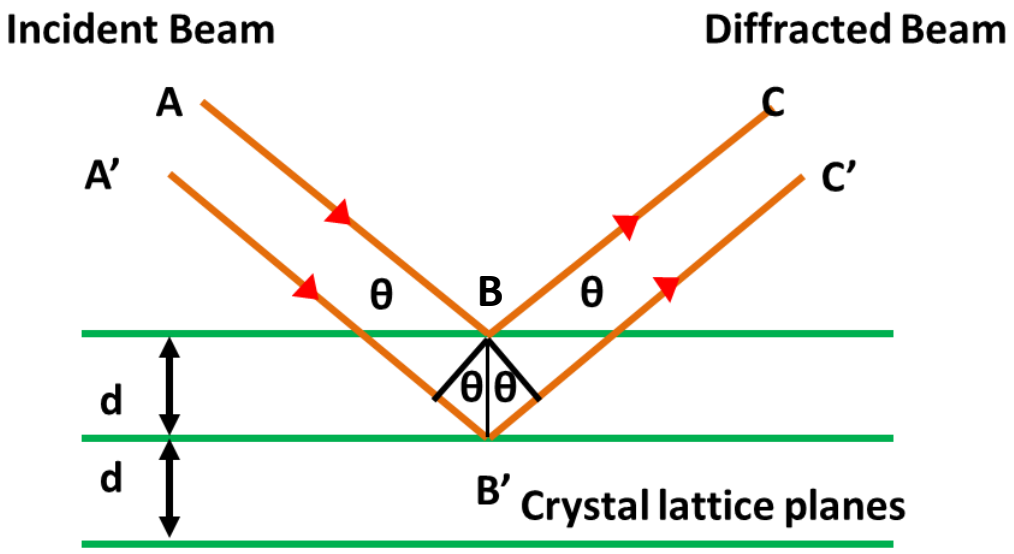

Scheme 1.1 Bragg's Law reflection. The diffracted X-rays exhibit constructive interference when the distance between paths ABC and A'B'C' differs by an integer number of wavelengths (λ).[70]

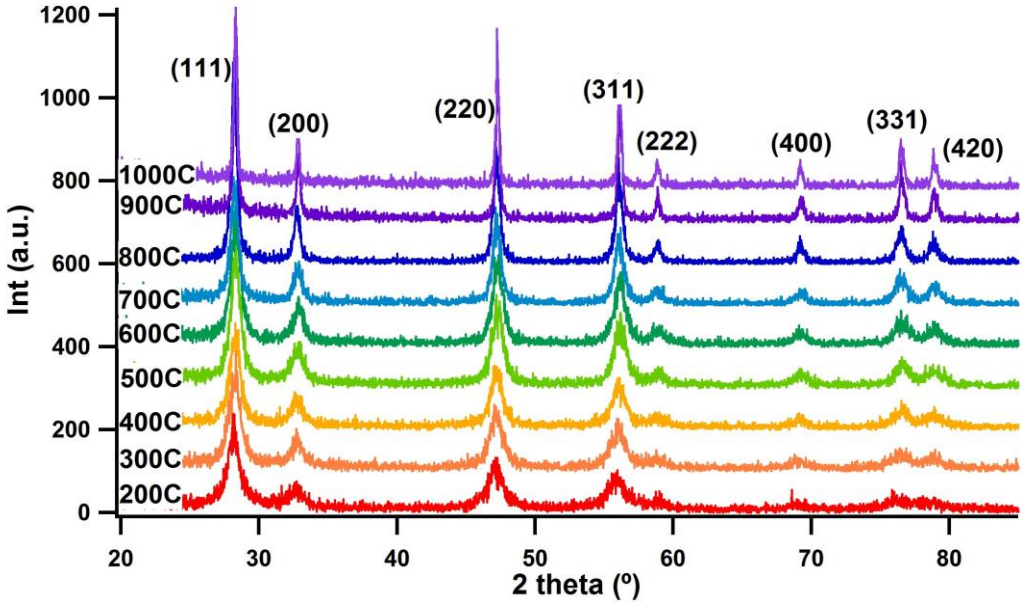

Figure 1.8 XRD patterns of cerium oxide nanorods activated at different temperatures.

1.3.3 X-ray Absorption Fine Structure

X-ray absorption fine structure (XAFS) spectroscopy is a unique tool for studying the local structure of selected elements in a material at atomic and molecular scales.[71] XAFS is going beyond the capabilities of a number of structural techniques, such as XPS, TEM, SEM etc., due to its applications in highly disordered nano/subnano materials and its operation under almost every environmental conditions.[72] With this, XAFS has been applied in numerous areas, including crystals, amorphous systems, glasses, membranes, solutions, liquids, gases, proteins, etc.

X-ray spectroscopy uses the X-ray photoelectric effect and the wave nature of the electron to determine local structures around selected atomic species. When X-ray with sufficient energy interacts with an atom, a deep-core electron in the atom can be ejected and propagate away, creating a hole in core level. A higher lying electron decays into the core-hole and emits a photon. The ejected photoelectron can be scattered by the neighboring atoms, generating interferences between the outgoing and scattered parts of the photoelectron wavefunction. These interferences cause an energy-dependent variation in the X-ray absorption probability, which is proportional to the X-ray absorption coefficient μ (E). The μ (E) parameter is a measurable quantity. Generally, μ (E) is an approximate linear function of $1/E^3$. However, at specific energy levels which are corresponding to the characteristic energies of the core electrons, for example, *s*, *p*, or *d* electrons, there are sudden increases called X-ray absorption edge.[71] (See Figure 1.9)

The X-ray absorption spectrum consists of two different regions, the X-ray Absorption Near Edge Structure (XANES) and the Extended X-ray Absorption Fine

Structure (EXAFS) region.[71] The XANES region includes the region before the absorption edge to the beginning of the EXAFS region (about 50eV above the absorption edge). XANES probes the transition of core electrons into unoccupied states. Multiple scattering patterns are dominant in XANES.

The EXAFS region usually starts from the point where the wavelength of photoelectron equals the distance between the absorbing atom and the closest neighboring atom to the point about 1000 eV past the inflection point of the absorption edge. The photoelectron generated in this region has higher kinetic energy. The outgoing wave can be scattered by the neighboring atoms, causing interference at the origin. This interference can be constructive or destructive, which depends on the interatomic distance and photoelectron wavelength. The constructive interference causes maxima in the spectrum while destructive interference is responsive to the minima in the spectrum.[71, 72]

XAFS has been used extensively to analyze the coordination number, bond length, structural disorder, and thermal motions of neighboring atoms. We have applied XAFS in investigating the structures of as-synthesized ceria and ceria supported noble metal nanomaterials. Ceria nanorods exhibited a Ce-O coordination number of 6.2 compared to 8 in its bulk counterpart, indicating a large deficiency of oxygen atoms around Ce atoms in ceria nanomaterials. Shorter bond length of Ce-O (2.294 Å) from EXAFS data fitting in ceria nanorods implied the quantum confinement effect present in nanoscaled particles.[18]

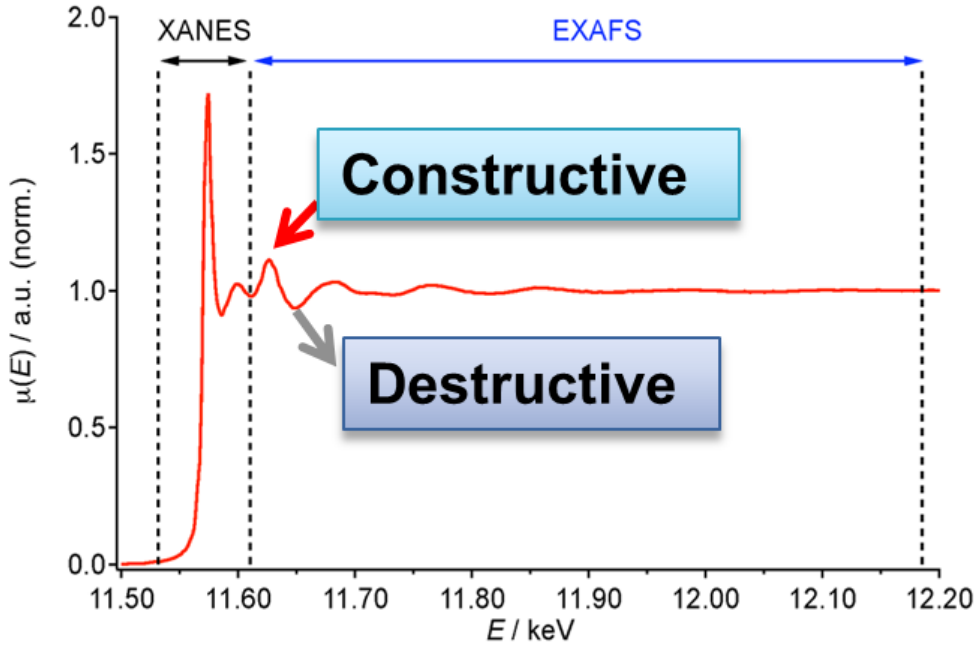

Figure 1.9 A typical X-ray absorption spectrum with XANES and EXAFS ranges.

1.3.4 X-ray Photoemission Spectroscopy

X-ray photoemission spectroscopy (XPS) is a popular surface technique. It plays an important role in understanding the working principles of solid catalysts based on its unique ability of investigating the surface geometric and electronic structure. Due to its short mean free path of photoelectrons in solid, XPS can only detect the top few atomic layers of the solid, which is dependent upon the kinetic energy of the detected electrons. XPS is usually used to analyze the chemical states and valence band electronic structure of materials.[73]

XPS is based on the observation of photoelectric effect. An electron in the atom is excited by impinging photon and promoted to vacuum level. The kinetic energy (E_k) of this emitted electron is measurable. The binding energy (E_B) of this electron can be calculated from the energy of incident beam ($h\nu$), the work function (φ) and kinetic energy.

$$E_B = h\nu - E_k - \varphi$$

The binding energy describes the energy required to remove an electron from a certain orbital, and the work function is the energy needed to take an electron from the inside of slide to the vacuum level. The binding energies of a particular core level in the same atom are different in different chemical environments, which make XPS very useful of characterizing materials. Binding energies are correlated with the partial charge on an atom, because the energy difference occurs due to different screening of the Coulomb interaction between the nucleus and the probed orbital through valence electrons. Therefore, the more the positive charge is, the higher the binding energy will be.[73]

XPS has been used to study the electronic states of Ce $3d_{5/2}$ and Ce $3d_{3/2}$ levels in Ce^{3+} and Ce^{4+} states. The CeO_2 XPS spectrum is composed of two multiplets, u and v. These multiplets correspond to the spin orbit split $3d_{5/2}$ and $3d_{3/2}$ core holes. Each spin-orbit component of the Ce 3*d* XPS spectrum is dominated by five features. Ten peaks corresponding to the pairs of spin-orbit doublets are identified in the Ce 3*d* spectrum (CeO_2). v^0, v', u^0, and u' peaks are attributed to Ce^{3+}; while v, v", v"', u, u", and u"'' are the characteristic peaks of Ce^{4+} ions. (See Figure 1.10) The surface Ce^{3+} concentration can be calculated by the areas of deconvoluted peaks using the following equation.[74] With the surface concentration of Ce^{3+}, one can easily decide the relative density of OVDs in ceria, which is helpful to determine the relationship of OVDs and performances of ceria catalysts. Indeed, this method has been used widely in understanding the roles of surface OVDs in ceria catalysis.[28, 74]

$$[Ce^{3+} = \frac{A_{v0} + A_{v'} + A_{u0} + A_{u'}}{A_{v0} + A_{v'} + A_{u0} + A_{u'} + A_v + A_{v''} + A_{v'''} + A_u + A_{u''} + A_{u'''}}]$$

.

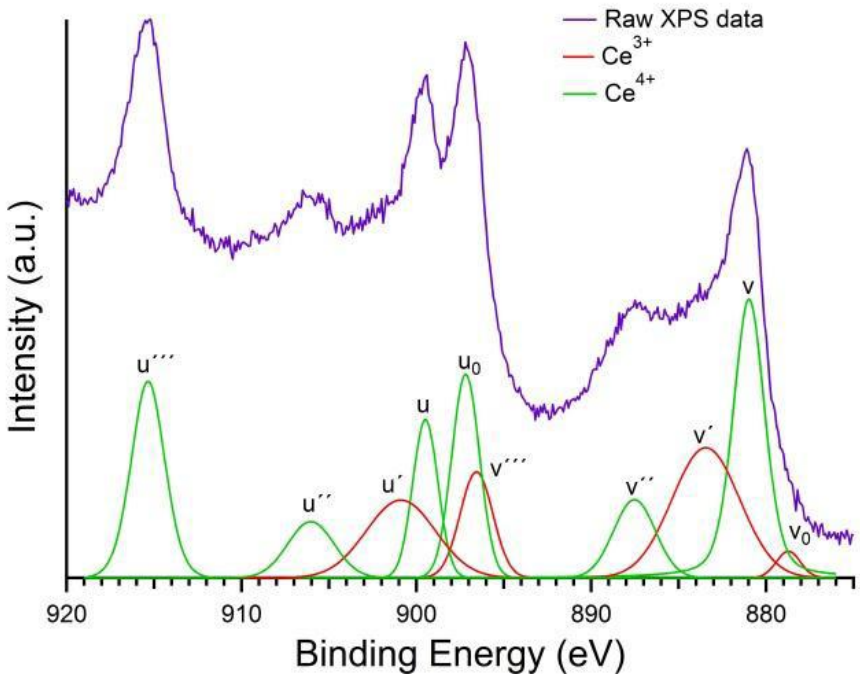

Figure 1.10 XPS peak fitting for low pressure activated ceria nanorods. (reprinted with permission from American Chemical Society) [28]

1.4 References

1 C. K. Gupta and N. Krishnamurthy, in *Extractive Metallurgy of Rare Earths*, CRC Press, Boca Raton, 2004.

2 A. Trovarelli, in *Catalysis by Ceria and Related Materials*, London, 2001, vol. 2, pp. 15-50.

3 J.-L. Sabot and P. Maestro, in *Kirk-Othmer Encyclopedia of Chemical Technology*, John Wiley & Sons, Inc., 2000.

4 J. B. Hedrick, *Min. Eng.*, 2000, **52**, 55-57.

5 A. Trovarelli, *Catalysis by Ceria and Related Materials*, London, 2013, vol. 12, pp.1-888.

6 J. Kaspar, M. Graziani and P. Fornasiero, eds., *Ceria-Containing Three Way Catalyts*, Elsevier, 2000.

7 S. Otsuka-Yao-Matsuo, T. Omata, N. Izu and H. Kishimoto, *J Solid State Chem*, 1998, **138**, 47-54.

8 N. Izu, T. Omata and S. Otsuka-Yao-Matsuo, *J. Alloy Compd.*, 1998, **270**, 107-114.

9 D. J. M. Bevan, *J. Inorg. Nucl. Chem.*, 1955, **1**, 49-59.

10 G. Brauer and K. A. Gingerich, *J. Inorg. Nucl. Chem.*, 1960, **16**, 87-99.

11 S. Vyas, *Simulation of Ceria: Bulk and Surface Defects*, University of London, 2005, pp. 85-143.

12 T. X. T. Sayle, S. C. Parker and C. R. A. Catlow, *Surf. Sci.*, 1994, **316**, 329-336.

13 M. Fronzi, A. Soon, B. Delley, E. Traversa and C. Stampfl, *J. Chem. Phys.*, 2009, **131**.

14 K. Kaneko, K. Inoke, B. Freitag, A. B. Hungria, P. A. Midgley, T. W. Hansen, J. Zhang, S. Ohara and T. Adschiri, *Nano Lett.*, 2007, **7**, 421-425.

15 http://nanospinel.blogspot.in/2007/08/nanopspinel-synthesis-by.html, 2007.

16 Y. Zhou, N. J. Lawrence, L. Wang, L. Kong, T.-S. Wu, J. Liu, Y. Gao, J. R. Brewer, V. K. Lawrence, R. F. Sabirianov, Y.-L. Soo, X. C. Zeng, P. A. Dowben, W. N. Mei and C. L. Cheung, *Angew. Chem. Int. Ed.*, 2013, **52**, 6936-6939.

17 Y. Y. Zhou, C. L. Menendez, M. J. F. Guinel, E. C. Needels, I. Gonzalez-Gonzalez, D. L. Jackson, N. J. Lawrence, C. R. Cabrera and C. L. Cheung, *RSC Adv.*, 2014, **4**, 1270-1275.

18 Y. Y. Zhou, N. J. Lawrence, T. S. Wu, J. Liu, P. Kent, Y. L. Soo and C. L. Cheung, *Chemcatchem*, 2014, **6**, 2937-2946.

19 N. Maksimchuk, *Proc. NAP.*, 2012, 1, 02NNBM281-3.

20 S. P. Wang, L. F. Zhao, W. Wang, Y. J. Zhao, G. L. Zhang, X. B. Ma and J. L. Gong, *Nanoscale*, 2013, **5**, 5582-5588.

21 X. Wang, Z. Y. Jiang, B. J. Zheng, Z. X. Xie and L. S. Zheng, *CrystEngComm*, 2012, **14**, 7579-7582.

22 X. Xie, Y. Li, Z.-Q. Liu, M. Haruta and W. Shen, *Nature*, 2009, **458**, 746-749.

23 H. G. Yang, C. H. Sun, S. Z. Qiao, J. Zou, G. Liu, S. C. Smith, H. M. Cheng and G. Q. Lu, *Nature*, 2008, **453**, 638-641.

24 M. Leng, M. Liu, Y. Zhang, Z. Wang, C. Yu, X. Yang, H. Zhang and C. Wang, *J. Am. Chem. Soc.*, 2010, **132**, 17084-17087.

25 K. B. Zhou, X. Wang, X. M. Sun, Q. Peng and Y. D. Li, *J. Catal.*, 2005, **229**, 206-212.

26 L. J. Liu, Z. J. Yao, Y. Deng, F. Gao, B. Liu and L. Dong, *ChemCatChem*, 2011, **3**, 978-989.

27 Q. Dai, H. Huang, Y. Zhu, W. Deng, S. Bai, X. Wang and G. Lu, *Appl. Catal. B*, 2012, **117–118**, 360-368.

28 N. J. Lawrence, J. R. Brewer, L. Wang, T.-S. Wu, J. Wells-Kingsbury, M. M. Ihrig, G. Wang, Y.-L. Soo, W.-N. Mei and C. L. Cheung, *Nano Lett.*, 2011, **11**, 2666-2671.

29 H.-X. Mai, L.-D. Sun, Y.-W. Zhang, R. Si, W. Feng, H.-P. Zhang, H.-C. Liu and C.-H. Yan, *J .Phys. Chem. B*, 2005, **109**, 24380-24385.

30 Q. G. Dai, S. X. Bai, H. Li, W. Liu, X. Y. Wang and G. Z. Lu, *CrystEngComm*, 2014, **16**, 9817-9827.

31 G. Hua, L. Zhang, G. Fei and M. Fang, *J. Mater. Chem.*, 2012, **22**, 6851-6855.

32 M. Choi, K. Na, J. Kim, Y. Sakamoto, O. Terasaki and R. Ryoo, *Nature*, 2009, **461**, 828-828.

33 C. C. Tang, Y. Bando, B. D. Liu and D. Golberg, *Adv. Mater.*, 2005, **17**, 3005-3009.

34 B. A. Averill, *Principles of General Chemistry*, 2012, pp. 1403-1521.

35 S. Vyas, *Simulation of Ceria: Bulk and Surface Defects*, University of London, 2005, pp.144-156.

36 T. G. Stratton and H. L. Tuller, *J. Chem. Soc., Faraday Trans. 2*, 1987, **83**, 1143-1156.

37 H. L. Tuller and S. R. Bishop, *Chem. Lett.*, 2010, **39**, 1226-1231.

38 M. C. Gobel, G. Gregori and J. Maier, *Solid State Ionics*, 2012, **215**, 45-51.

39 B. C. H. Steel and J. M. Floyd, *Proc. British. Ceram. Trans.*, 1971, **72**, 55-76.

40 J. Faber Jr, M. A. Seitz and M. H. Mueller, *J. Phys. Chem. Solids*, 1976, **37**, 903-907.

41 H. L. Tuller and A. S. Nowick, *J. Electrochem. Soc.*, 1979, **126**, 209-217.

42 S. Bernal, J. J. Calvino, M. A. Cauqui, J. M. Gatica, C. Larese, J. A. P. Omil and J. M. Pintado, *Catal. Today*, 1999, **50**, 175-206.

43 F. Esch, S. Fabris, L. Zhou, T. Montini, C. Africh, P. Fornasiero, G. Comelli and R. Rosei, *Science*, 2005, **309**, 752-755.

44 M. Mogensen, T. Lindegaard, U. R. Hansen and G. Mogensen, *J. Electrochem. Soc.*, 1994, **141**, 2122-2128.

45 M. Mogensen, in *Catalysis by Ceria and Related Materials*, London, 2001, vol. 2, pp. 453-481.

46 G. Wang, L. Wang, X. Fei, Y. Zhou, R. F. Sabirianov, W. N. Mei and C. L. Cheung, *Catal. Sci. Technol.*, 2013, **3**, 2602-2609.

47 M. Tamura, M. Honda, Y. Nakagawa and K. Tomishige, *J. Chem. Technol. Biotechnol.*, 2014, **89**, 19-33.

48 J. Khaladji and M. Peltier, Google Patents, 1990.

49 K. Schermanz, in *Catalysis by Ceria and Related Materials*, London, 2001, vol. 2, pp.1-13.

50 J. F. Wang, Google Patents, 1996.

51 K. Hanawa, N. Mochizuki and N. Ueda, Google Patents, 1999.

52 M.-S. Tsai, *Mater. Sci. Eng., B*, 2004, **110**, 132-134.

53 C. A. Mirkin, *Small*, 2005, **1**, 14-16.

54 J. M. Campelo, D. Luna, R. Luque, J. M. Marinas and A. A. Romero, *ChemSusChem*, 2009, **2**, 18-45.

55 R. J. White, R. Luque, V. L. Budarin, J. H. Clark and D. J. Macquarrie, *Chem. Soc. Rev.*, 2009, **38**, 481-494.

56 A. Vantomme, Z. Y. Yuan, G. H. Du and B. L. Su, *Langmuir*, 2005, **21**, 1132-1135.

57 L. Eyring, in *Synthesis of Lanthanide and Actinide Compounds*, eds. G. Meyer and L. R. Morss, Springer Netherlands, 1991, vol. 2, pp. 187-224.

58 C. deLeitenburg, A. Trovarelli and J. Kaspar, *J. Catal.*, 1997, **166**, 98-107.

59 S. Nakane, T. Tachi, M. Yoshinaka, K. Hirota and O. Yamaguchi, *J. Am. Ceram. Soc.*, 1997, **80**, 3221-3224.

60 N. Audebrand, J. P. Auffredic and D. Louer, *Chem. Mater.*, 2000, **12**, 1791-1799.

61 H. Abimanyu, B. S. Ahn, C. S. Kim and K. S. Yoo, *Ind. Eng. Chem. Res.*, 2007, **46**, 7936-7941.

62 http://www.gitam.edu/eresource/nano/nanotechnology/bottamup%20app.htm.

63 D. A. Ward and E. I. Ho, *Ind. Eng. Chem. Res.*, 1995, **34**, 421-433.

64 http://en.wikipedia.org/wiki/Sol-gel.

65 M. Darroudi, M. Hakimi, M. Sarani, R. Kazemi Oskuee, A. Khorsand Zak and L. Gholami, *Ceram. Int.*, 2013, **39**, 6917-6921.

66 S. D. Jackson and J. S. J. Hargreaves, in *Metal Oxide Catalysis*, Wiley-VCH Verlag GmbH & Co. KGaA, Weinheim, 2009, pp. I-XXVIII.

67 W. Zhou, in *Metal Oxide Catalysis*, Wiley-VCH Verlag GmbH & Co. KGaA, Weinheim, 2009, pp. 443-485.

68 B. D. Cullity and S. R. Stock, *Elements of X-ray Diffraction*, 3rd ed., Prentice Hall, 2001.

69 http://en.wikipedia.org/wiki/X-ray_crystallography.

70 http://serc.carleton.edu/research_education/geochemsheets/BraggsLaw.html.

71 G. Bunker, *Introduction to XAFS: A Practicle Guide to X-ray Absorption Fine Structure Spectroscopy*, Cambridge University Press, New York, 2010.

72 M. Stockenhuber, in *Metal Oxide Catalysis*, Wiley-VCH Verlag GmbH & Co. KGaA, Weinheim, 2009, pp. 299-321.

73 D. Teschner, E. M. Vass and R. Schlögl, in *Metal Oxide Catalysis*, Wiley-VCH Verlag GmbH & Co. KGaA, Weinheim, 2009, pp. 243-298.

74 S. Deshpande, S. Patil, S. V. N. T. Kuchibhatla and S. Seal, *Appl. Phys. Lett.*, 2005, **87**, 133113.

CHAPTER 2

REGENERATIVE ABILITY OF PALLADIUM CATALYSTS ON NANOSTRUCTURED CERIUM OXIDE SUPPORT FOR CARBON MONOXIDE OXIDATION

2.1 Introduction

One of the biggest problems in the chemical industry is that catalysts tend to lose activity after extensive use. The loss in catalytic activity, or catalyst deactivation, can be attributed to various reasons including morphological changes, sintering, or catalyst poisoning either by reactants or products.[1-5] For example, the deactivation of supported palladium (II) oxide (PdO) catalysts was observed at high temperature or after extensive use, being caused by the formation of metallic palladium (Pd) from PdO particles.[6-8] Significant effort has been devoted to improve the stability and the regenerative property of catalysts.[9,10] Much attention has been focused on various systems of supported Pd or platinum (Pt) catalysts such as Pd/SiO_2,[11-13] Pd/CeO_2,[14-18] Pt/TiO_2,[19] Pd/perovskites,[20-22] and Pt/CeO_2[23,24] because of their sintering-resistant and regenerative properties. These supports are often porous or oxygen-deficient. They can serve as physical barriers to prevent sintering of supported metal nanoparticles or oxygen-providers to re-oxidize reduced metal nanoparticles and maintain their stable catalytic activity.

Cerium oxide (ceria, CeO_{2-x}, where $0 \leq x < 0.5$) is a well-recognized catalyst support for the stabilization of noble metal particles against sintering.[25-27] It has attracted great attention in diverse fields such as automobile catalysis,[28,29] organic chemical

synthesis[30-32] and fuel cells.[33,34] It has been reported to demonstrate the regenerative capability when combined with noble metals or transition metal oxides in various reactions, such as carbon monoxide (CO) oxidation, nitrogen oxides (NO_x) reduction and ethanol reforming reactions.[27,35,36] A previous study on a Pd-based ceria catalyst reported that the catalyst exhibited "self-regenerative" property in CO oxidation at 500 °C. The catalyst consistently showed fully restored catalytic activity after thermal treatments in an oxidative environment.[35] The Pd species exhibited reversible processes of moving-in and moving-out-of the ceria support upon successive reduction-oxidation cycles. This phenomenon was proposed to be responsible for the observed regenerative property[35] and was likely due to the surface PdO species or Pd^{2+}-like species incorporated in the ceria lattice. Another regeneration study on a Pt-based ceria catalyst system (Pt/Al_2O_3-CeO_2) illustrated the reversible changes in the Pt oxidation state under oxidative and reductive conditions. A complex oxide formed between Pt and its ceria support was attributed to the regenerated catalytic activity.[25] Many other studies on similar regenerative catalyst systems in the past have been mainly focused on either investigating the regeneration mechanism or enhancing the regenerative abilities of those catalysts at high temperatures.[25, 37] For instance, the oxidation and reduction of Pd species assisted by the support was proposed as the regeneration mechanism,[22,38] and various mixed metal oxide supports and synthesis methods were explored to promote the catalytic activity.[25,35] However, the exact nature of the active species and the role of ceria support are still controversial because of the large variations in the reported catalyst synthetic methods and the complexity of mixed metal oxide supporting materials. Therefore, it is essential to study the effects of atomic structures and oxidation states of both supported metals and

ceria support in ceria-based catalyst systems in order to gain further insights into the understanding of their regenerative activity.

Herein we report the regenerative ability of Pd decorated ceria nanorod (abbreviated as Pd/CeO_{2-x}) catalyst under ambient conditions for the CO oxidation reaction and propose possible explanations for the observed phenomenon by revealing the structure-activity relationships in this catalyst system. Ceria nanorod supports were studied due to their higher catalytic activity towards different reactions when compared with other shapes of nanocrystalline ceria.[39,40] Most previous reports focus on studies of ceria-supported palladium or palladium oxides at high temperatures (for example, 800 °C in oxygen atmosphere).[35] Unlike the cases of high temperature reactions in which ceria nanoparticles tend to agglomerate and thus diminish their active surface areas,[27,37,38] the Pd/CeO_{2-x} nanorod catalyst is expected to remain its shaped structure in room temperature reactions. Thus, our regeneration study of Pd/CeO_{2-x} in mild oxidative environment can be of potential importance. To gain insights into the active species of the regenerative Pd/CeO_{2-x} catalysts, X-ray photoemission spectroscopy (XPS), X-ray absorption near edge spectroscopy (XANES) combined with extended X-ray absorption fine structure (EXAFS) study were utilized to resolve the oxidation states and the local atomic environments of the palladium species and the oxygen vacancy defects (OVDs) in the ceria nanorod support. Results of these studies revealed that the Pd ions of the catalyst interacted with the ceria nanorod support and formed PdO_y (disordered PdO and possibly PdO_2-like clusters), which were observed to be the most active component of this catalyst for the CO oxidation reaction and in the catalyst regeneration process. Furthermore, the extent of regenerative ability of Pd/CeO_{2-x} catalysts was found to be positively correlated

to the density of OVDs on the surface of ceria nanorods supports, suggesting the significance of OVDs of oxide supports for engineering regenerative catalysts.

2.2 Experimental Methods

2.2.1 Synthesis of Cerium Oxide Supported Palladium Catalysts

Cerium (III) sulfate hydrate ($Ce_2(SO_4)_3 \bullet xH_2O$), potassium tetrachloropalladate(II) (K_2PdCl_4), sodium hydroxide (NaOH) were purchased from Sigma-Aldrich (St. Louis, MO). Hydrogen peroxide 30 % (H_2O_2) was purchased from VWR SP (Batavia, IL). All chemicals were used without further purification. All water used in the experiments was ultrapure water purified using a Synergy Millipore system (Synergy, Kankakee, IL) with a resistivity greater than 18 MΩ•cm at 25 °C.

The nanostructured ceria support was synthesized by using a hydrothermal method modified from that reported by Zhou *et al*.[68] A sample of 0.5 g of $Ce_2(SO_4)_3 \bullet xH_2O$ and 40 mL of 10 M NaOH were mixed and added to a 50-mL capacity Teflon-lined stainless steel autoclave. The chemicals in the autoclave were hydrothermally treated for 15 h. at 120 °C in a convection oven to generate cerium (III) hydroxide ($Ce(OH)_3$) nanorods. The product was filtered with a 3.0-μm pore size polycarbonate filter membrane (Millipore, Billerica, MA), rinsed with three aliquots of 50 mL water and placed in the convection oven for an initial oxidation at 50 °C for 2 h. During this oxidation process, most $Ce(OH)_3$ was converted to cerium oxide composed of both Ce_2O_3 and CeO_{2-x}. The oxides were then mixed with 25 ml of water. Subsequently, 55.68 μL of 10 g/L K_2PdCl_4 solution was added into the oxide-water mixture to synthesize 0.1 at.% Pd/CeO_{2-x} sample. Different volumes of K_2PdCl_4 precursor-solution were used

accordingly for the synthesis of other loadings of Pd/CeO_{2-x} catalysts. The mixture was stirred for 20 min. to incorporate Pd into the cerium oxide nanorods. Following the Pd incorporation, 25 mL of 30 % aqueous H_2O_2 was added to the mixture and sonicated for 30 min., followed by stirring for 30 min. to allow the reaction to reach completion. Then, the resulting catalyst was filtered with a 3.0-μm pore size polycarbonate membrane, rinsed with 50 ml of water and dried for 4 h. at 50 °C in a convection oven. Lastly, the synthesized material was activated at 400 °C in simulated air (20 % O_2, 80 % N_2) at 100 SCCM (standard cubic centimeter per minute) for 30 min. in a horizontal quartz-tube annealing furnace with an operating pressure of 2.0 Torr for low-vacuum-activated sample and 0.07 Torr for high- vacuum-activated sample.

2.2.2 Characterization of Catalysts

The elemental composition of the catalysts was analyzed using a Thermo Jarrell Ash IRIS Advantage Inductively Coupled Plasma Optical Emission Spectrometer (ICP-OES). A catalyst sample of 50 mg was dissolved in 10 ml of freshly made aqua regia (70 % concentrated HCl: 30 % concentrated HNO_3) at 110 °C for 1 h. in an acid digestion autoclave. The resulting solution was then diluted with water to a 50 mL total volume solution for the elemental analysis.

The morphology of the catalyst particles was investigated by transmission electron microscopy (TEM). The catalyst powders were dispersed in methanol. 10 μL of the suspension mixture was sonicated for 5 sec. and loaded on holey carbon films supported on copper TEM grids. TEM micrographs were collected using a Hitachi H7500 transmission electron microscope (Hitachi High Technologies America, Inc., Pleasanton CA) operated at 100 kV. High resolution TEM (HRTEM) images were collected using a

Tecnai G^2 F20 S-Twin 200 kV field-emission TEM (FEI Company, Hillsboro, OR). Images were analyzed with the Digital Micrograph™ software. The crystal structures of the samples were investigated with a Rigaku D/Max-B diffractometer (Rigaku America, The Woodlands, TX) equipped with a Cu Kα X-ray source of average wavelength 1.544 Å.

The reducibility of the Pd/CeO_{2-x} catalysts was determined by H_2-temperature programmed reduction (TPR) technique. 20 mg of sample (ceria nanorods and Pd/CeO_{2-x} activated at low or high vacuum) was placed in a quartz reactor which was connected to a homemade TPR apparatus. A 5 % H_2 - 95 % N_2 gas mixture with a flow rate of 20 mL/min. was used as the reducing agent. The reactor ramp rate was 10 °C/min. The H_2 uptake during the reduction was measured by a thermal conductivity detector (TCD), calibrated by CuO powder. The H_2-TPR experiment of reduced Pd/CeO_{2-x} catalyst was performed using a PCA-1200 adsorption apparatus equipped with a TCD detector (Beijing Builder Company, Beijing, China). The experimental condition for this sample was consistent with the other samples, except that the reducing gas mixture is 5 % H_2 - 95 % Ar gas.

An X-ray photoelectron spectroscopy (XPS) study was carried out *ex situ* using a PHI 5000 VersaProbe system (Physical Electronics, Inc., Chanhassen, MN) equipped with a monochromatic Al Kα X-rays at an operating pressure of $5x10^{-7}$ Pa. XPS experiments were performed using a high resolution 180 degree spherical capacitor energy analyzer. A quartz crystal monochromator was used to focus and scan samples. A 200-μm spot size was used for analysis. Sample charging during the measurement was compensated by using the VersaProbe Dual beam charge compensation system. The X-

ray take-off angle was 45° with respect to the sample surface. The pass energy was 23.5 eV for the Pd 3d core level spectra with an energy resolution of 0.2 eV. All spectra were calibrated using the carbon 1s peak at 284.8 eV.

The palladium decorated ceria nanorod samples were also studied using the X-ray absorption near edge structure (XANES) technique. Three samples of 1 at.% Pd on ceria processed at the different stages of catalyst evaluation were studied: (Stage 1) Catalyst after low vacuum annealing activation; (Stage 2) Catalyst after the carbon monoxide oxidation reaction leading to a deactivated catalyst; and (Stage 3) Catalyst after a 24-h. regeneration under ambient conditions. The Pd K-edge XANES and EXAFS measurements were carried out at beamline BL01C of Taiwan Light Source at National Synchrotron Radiation Research Center (NSRRC) in Taiwan. A Si (111) double-crystal monochromator was used to scan the photon energy. The energy resolution ($\Delta E/E$) for the incident x-ray photons is estimated to be 1×10^{-4}. The absolute energy scale was calibrated by assigning established Pd K-edge to the first inflection point 24350 eV of the spectra taken from a Pd foil. The samples were prepared with sealed Kapton® tapes in a nitrogen glove box. Spectra were collected in the fluorescence yield mode using a Lytle fluorescence detector for the three 1 at.% Pd on ceria samples processed at the three different stages (after the catalyst activation, after the CO oxidation evaluation and after the regeneration under ambient conditions for 24 h.). At least two scan sets were collected for each of the samples to demonstrate the reproducibility of the experimental data. The spectra of the Pd K-edge XANES for metallic Pd and PdO were collected as the Pd references according to the standard procedure[69,70] and analysed using the FEFF software.[57-59]

The Ce L_3-edge XANES spectra were collected ex situ at the DCM beamline at the Center for Advanced Microstructures and Devices (CAMD, Louisiana State University, Baton Rouge, LA). Monochromatic light was obtained using a double crystal monochromator of the Lemonnier type equipped with a Ge (220) crystal pair for the cerium analysis.[71] The estimated energy resolution was approximately 2 eV. The absolute energy scale was calibrated by assigning established chromium K-edge to the first inflection point of the spectra taken from a chromium foil. Spectra were collected in the transmission mode for the bulk ceria as standard and three 1 at.% Pd/CeO_{2-x} samples processed at three different stages (after the catalyst activation, after the CO oxidation evaluation and after the regeneration under ambient conditions for 24 h.) under a nitrogen atmosphere of 15 Torr. At least two scans were collected on all samples and demonstrated the reproducibility of the experimental data. The Ce L_3-edge spectra were analysed using FEFF software.[56-59]

2.2.3 Catalytic Oxidation of Carbon Monoxide (CO)

Carbon monoxide (CO) oxidation reactions with the palladium decorated ceria (Pd/CeO_{2-x}) catalysts were carried out in a U-tube fixed bed quartz reactor with a 30 mL/min. flow of a factory-pre-mixed feed gas composed of CO (1.06 %) and O_2 (20.41 %) balanced in helium and controlled by a mass flow controller (MFC, Type 1479A, MKS Instruments, Inc., Andover, MA). 100 mg of Pd/CeO_{2-x} catalyst was used for each of the catalytic activity reactions. Gas chromatography (GC, Agilent 7820A, Agilent Technologies, Santa Clara, CA) with a packed column (Alltech Haysep Q 80,100, Grace, Deerfield, IL) was used to monitor the concentrations of CO_2 in the effluent. Between each consecutive data point collected at different reaction temperatures, a

minimum of 10 min., without reaction gases flowing, were allowed for the system to reach thermal equilibrium before collection. The catalytic activity of the samples was examined at reaction temperatures from 0 °C to 100 °C with 10 °C intervals for 0.1 at. %, 1 at.% and 2 at.% Pd on cerium oxide. The temperature was controlled by a low-temperature-circulator chiller (RC6 CS Lauda). For pure ceria nanorods, the reaction temperatures were chosen from 50 °C to 200 °C with 10 °C intervals. Series of long term catalytic reactions of 1 at.% Pd/CeO_{2-x} were operated at 25 °C for 24 h. The regeneration process was taken under ambient conditions (~20 °C and ~20 % relative humidity).

2.3 Results and Discussion

2.3.1 Structural Characterization of Catalysts

The Pd/CeO_{2-x} nanorod catalysts with 0.1 to 2 at.% Pd content were synthesized by employing a wet impregnation method of Pd on ceria nanorods and a subsequent low vacuum activation at 2.0 Torr and 400 °C.[29] The morphology and lattice structure of the nanorod catalysts were characterized using high resolution transmission electron microscopy (HRTEM) and X-ray diffraction (XRD). Typical bright field TEM images in Figure 2.1 show that the as-synthesized 1 at.% Pd/CeO_{2-x} nanorods were highly crystalline with lengths between 300 nm and 800 nm and diameters ranging from 7 nm to 15 nm. The TEM images nanorods typically displayed the 3.1 Å lattice fringes corresponding to the (111) lattice of cubic fluorite-structured CeO_2. Upon extensive HRTEM imaging, no palladium or palladium oxide particles were observed in any HRTEM images of the Pd/CeO_{2-x} catalysts containing between 0.1 and 2 at.% of Pd vs. Ce. XRD patterns of the as-synthesized catalysts further confirmed that the cerium oxide substrates existed in the cubic fluorite phase of CeO_2. However, no reflections

corresponding to Pd metal, palladium (II) oxide (PdO), or palladium (IV) oxide (PdO_2) in these samples were observed. (Figure 2.2) Nonetheless, the expected concentrations of Pd in the ceria nanorod catalysts were confirmed by inductively coupled plasma optical emission spectroscopy analysis with values reported to be within ±0.1 at.% for the 1 at.% and 2 at.% of Pd and ±0.02 at.% for the 0.1 at.% of Pd in the corresponding Pd/CeO_{2-x} catalysts. Energy-dispersive X-ray (EDX) spectra recorded at different positions along the catalyst rods verified the presence of Pd along the entire length of a Pd/CeO_{2-x} nanorod. (Figure 2.3) Since our exhaustive HRTEM could not detect any Pd or PdO particles, we postulate that the Pd in the catalyst were either in the forms of very small palladium or palladium oxide clusters and/or Pd atoms highly dispersed on ceria nanorods.

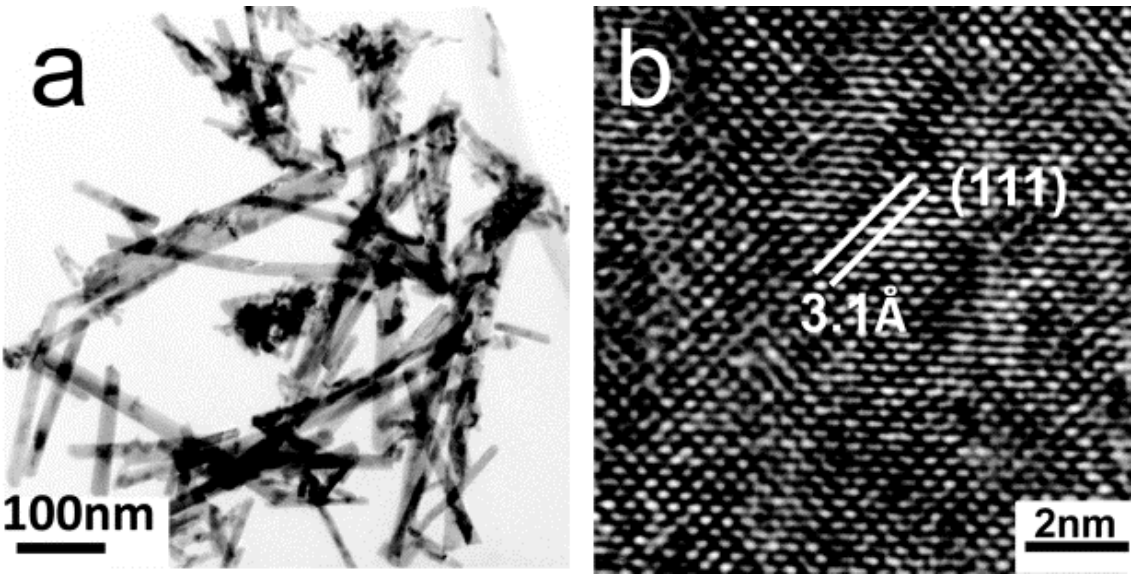

Figure 2.1 Typical TEM and HRTEM images of 1 at.% Pd on ceria after activation. (a) Typical TEM image of Pd/CeO_{2-x} nanorods. (b) HRTEM image of a Pd/CeO_{2-x} nanorod showing lattice fringe spacing of 3.1 Å corresponding to the (111) planes of fluorite-structured ceria.

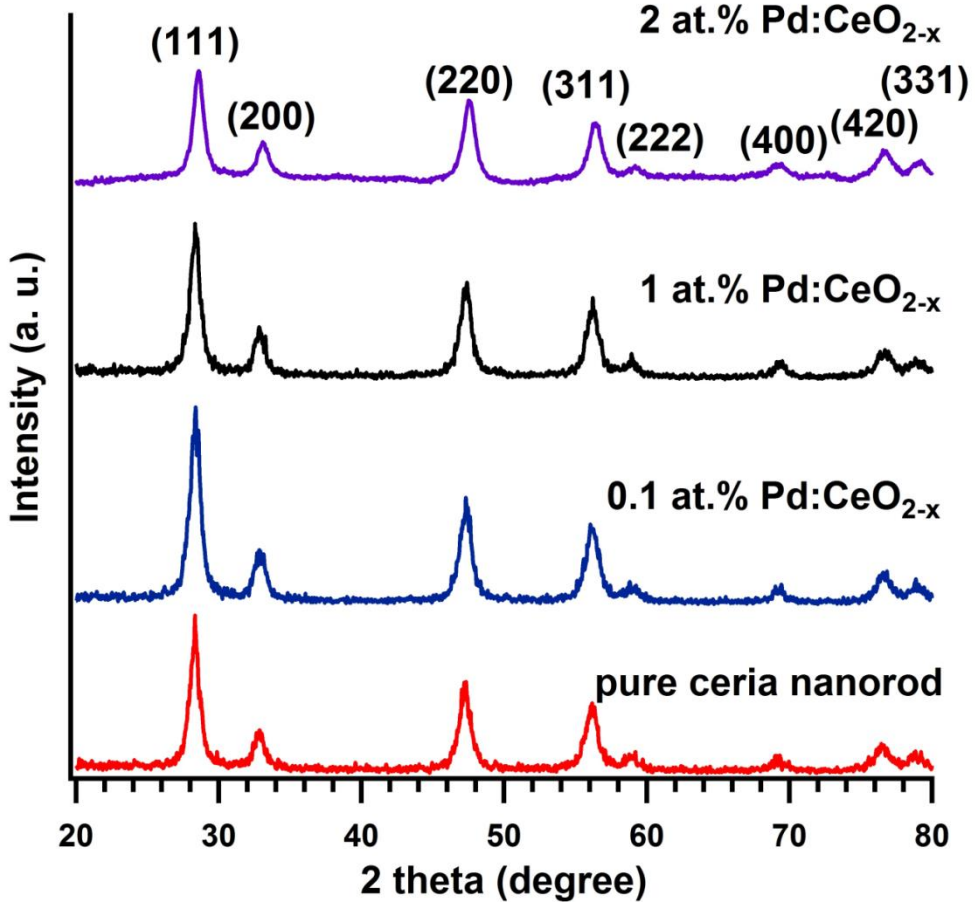

Figure 2.2 XRD patterns of 0.1 at.%, 1 at.% and 2 at.% Pd/CeO_{2-x} nanorods and CeO_{2-x} (ceria) nanorods after low vacuum (2.0 Torr) activation. All peaks are indexed with respect to the cubic $Fm\bar{3}m$ structure of CeO_2. No peaks corresponding to Pd or PdO or PdO_2 are present in the XRD patterns. ICDD card 04-013-4361 was used for the peak assignments for the CeO_2 content in the patterns.

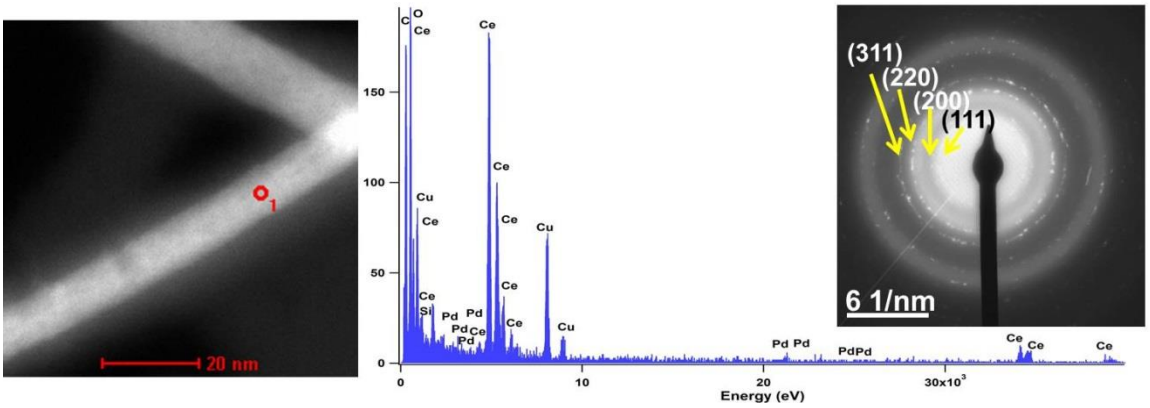

Figure 2.3 (Left) Scanning transmission electron microscopy (STEM) image of 1 at.% Pd/CeO_{2-x} nanorods (low vacuum activated under 2.0 Torr). (Middle) Energy-dispersive X-ray (EDX) spectrum of a 1 at.% Pd/CeO_{2-x} nanorod obtained at the red circle location on the left STEM image. The presence of Pd in the Pd/CeO_{2-x} nanorod was clearly revealed in the EDX data. (Right) Selected area electron diffraction (SAED) pattern of the 1 at.% Pd/CeO_{2-x} nanorods. Rings of SAED patterns indicate the polycrystallinity of ceria samples. The rings are indexed against the fluorite structured ceria.

2.3.2 Catalytic Activity and Regenerative Property Towards CO Oxidation

The Pd/CeO_{2-x} nanorods demonstrated more enhanced catalytic activity than pure CeO_{2-x} nanorods towards CO oxidation. The catalytic activity of the Pd/CeO_{2-x} nanorods was evaluated as a function of reaction temperature and Pd content in the catalysts. Figure 2.4a shows that catalysts with greater atomic percentages of Pd content are more active and have lower light-off temperatures (T_{50}) for the CO oxidation reaction. The 2 at.% Pd/CeO_{2-x} catalyst achieves 50 % CO conversion at 18 °C, whereas 50 % CO conversions are not achieved until 32 °C, 65 °C, and 150 °C for the 1 at.% Pd/CeO_{2-x}, 0.1 at.% Pd/CeO_{2-x} and pure CeO_{2-x} nanorods, respectively. At 50 °C, pure ceria nanorods exhibit almost non-detectable CO oxidation activity, while the 1 at.% and 2 at.% Pd/CeO_{2-x} catalysts demonstrate nearly complete CO conversion. However, the catalytic activity of Pd/CeO_{2-x} catalyst was found to drop in prolonged CO oxidation reactions. For example, Figure 2.4b illustrates that the % of CO conversion by the 1 at.% Pd/CeO_{2-x} catalyst decreased from 30 % to 15 % after 2 h. of reaction at room temperature (20 °C) during the initial reaction run. The product (CO_2) yield continued to drop in the next 15 h. until it reaches 8 % conversion and remained at that level for at least the next 7 h. (The complete product yield curve for this 24 h. run is not shown.) We attribute the decrease in catalytic activity of Pd/CeO_{2-x} to the chemical transformation of Pd species in the catalyst during CO oxidation reaction. This is supported by the observed significant color change of the 1 at.% Pd/CeO_{2-x} catalyst from yellow to dark olive drab, indicating a significant chemical change in the catalyst after CO-reduction at room temperature.

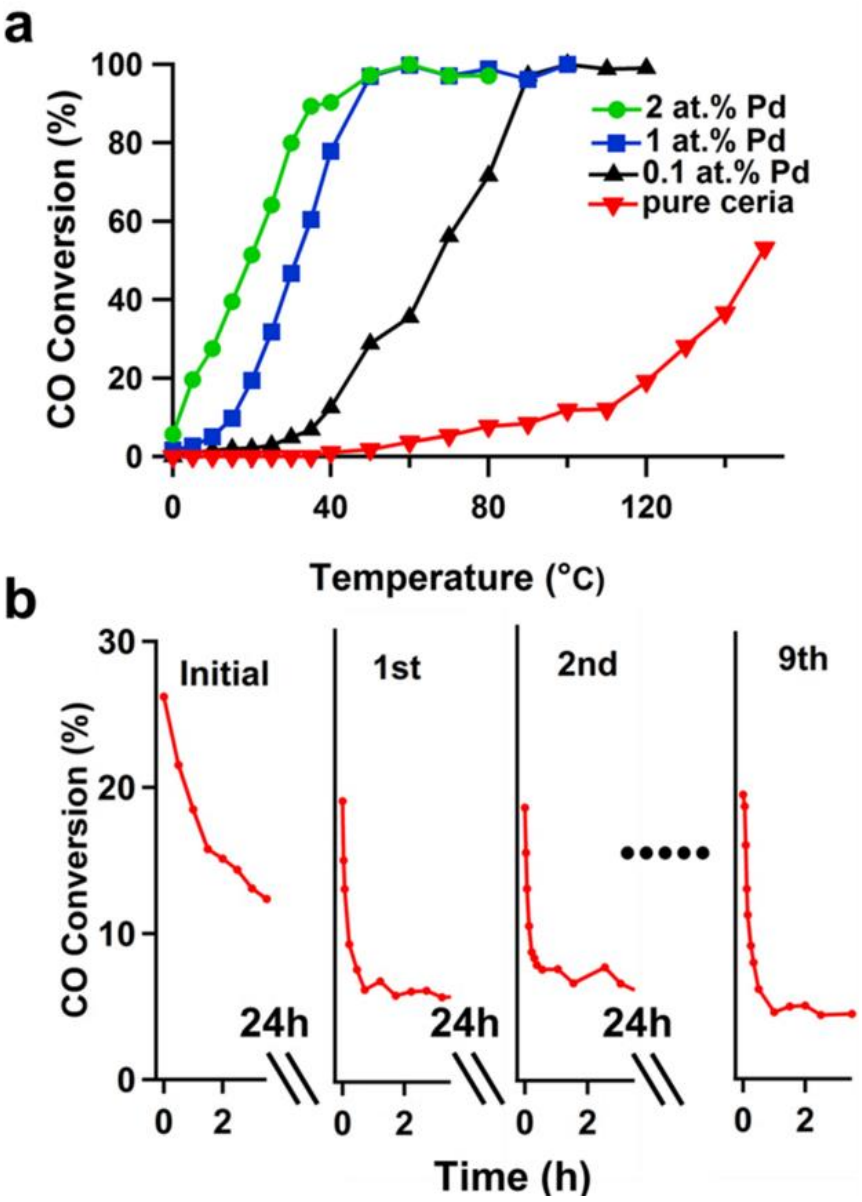

Figure 2.4 (a) Temperature dependent carbon monoxide conversion over (●) 2 at.% Pd, (■) 1 at.% Pd, (▲) 0.1 at.% Pd and (▼) 0 at.% Pd on cerium oxide nanorods (Pd/CeO_{2-x}). A factory pre-mixed gas stream composing of 1.06 % CO and 20.41 % O_2 balanced in He was fed to the reactor in a flow rate of 30 mL/min. (b) Series of CO catalytic reactions of 1 at.% Pd/CeO_{2-x} at 20 °C for 24 h. and regenerative treatment under ambient conditions 24 h. between each reaction run.

In order to gauge the regenerative property of the catalyst, we subjected the 1 at.% Pd/CeO_{2-x} to the CO oxidation evaluation for 24 h. at room temperature (20 °C), followed by exposing the reacted (or reduced) catalyst to air under ambient conditions (~20 °C and ~20 % relative humidity) for 24 h. for regeneration. Afterwards, the regenerated catalysts were found to exhibit 73 ± 6 % of its original catalytic activity (Figure 2.4b 1^{st} run). After a series of CO oxidation reaction and regeneration cycles, the catalyst maintained similar efficiencies (60 – 80 % of the original activity) and effective life spans. Several batches of the catalysts were continuously reduced and regenerated for more than nine redox cycles and similar behaviors were observed. To ascertain the cause of catalyst regenerative ability not resulting from the build-up and elimination of carbonate species on the catalyst surface, we analyzed the XPS O 1s spectra of the as-synthesized, reduced, and regenerated samples. (See Figure 2.5) Since the carbonate peaks were present in the XPS spectra of all three samples with almost identical intensity, the regenerated catalytic activity likely had insignificant contributions from the elimination of carbonate species during the regeneration process. Additionally, the carbonate species were unlikely to be removed without heating at high temperature, subjecting the sample to vacuum, or inert gas exchange. Thus, our regeneration method by exposing the used catalyst to ambient conditions was unlikely to remove a detectable amount of carbonate species from the surface. According to the color change of the catalysts in CO oxidation reaction, some of the decorated Pd was possibly reduced by CO to form small Pd metal particles. These small Pd particles, which are typically grey or black, likely agglomerated on the yellow ceria support surface and contributed to the dark olive drab color of the reacted catalyst.

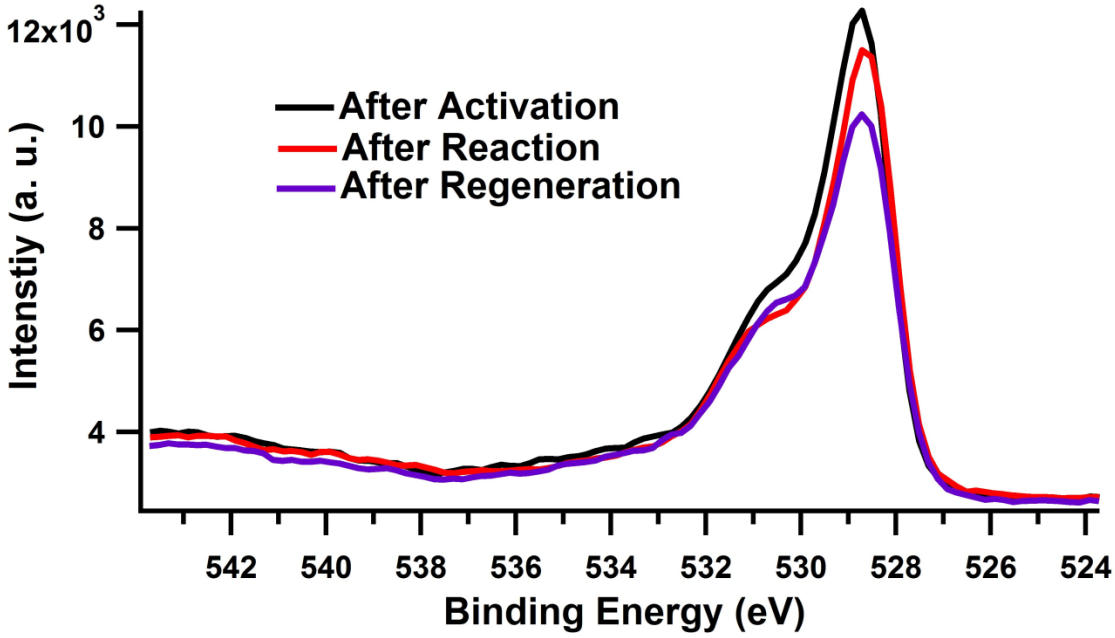

Figure 2.5 The O 1s XPS spectra of 1 at.% Pd/CeO_{2-x} catalysts after activation (activated under 2.0 Torr), after reaction with CO for 24 h. and after regenerated under ambient conditions for 24 h. The shoulder peak at 531.5 eV is ascribed to the carbonate species existing in the catalysts.[1]

The growth of Pd metal particles might cause the depression of catalytic activity of the Pd/CeO_{2-x} catalyst during long CO oxidation reactions.[11, 13, 22] After the regenerative treatment, some of the Pd^0 in small metal particles were oxidized back to Pd^{n+}, the initial chemical state in the fresh catalyst, by oxygen in air and therefore regained part of the catalytic activity of the fresh catalyst over CO oxidation. Thus, we attribute the restored catalytic activity of Pd/CeO_{2-x} catalyst largely to chemical transformation of Pd species in the catalyst.

2.3.3 Catalysts Active Species Towards CO Oxidation

The regeneration ability and enhanced catalytic activity of Pd/CeO_{2-x} is hypothesized to be due to the formation of Pd oxides, similar to the cases of previously reported Pd-based metal oxide catalysts.[41] To validate this hypothesis, hydrogen-temperature programmed reduction (H_2-TPR) studies were performed to evaluate the reduction capability of different oxides on the activated Pd/CeO_{2-x} catalyst and pure ceria nanorods support. From the H_2-TPR profiles shown in Figure 2.6, the profile of pure ceria nanorods exhibits a weak and broad reduction peak at about 400 °C, which can be attributed to easily reducible surface Ce^{4+} species.[26] In contrast, the major H_2 reduction peak of activated Pd/CeO_{2-x} appears at ~100 °C - 170 °C. Numerous studies have demonstrated that the reduction temperature of metal oxides by H_2 can be lowered by the addition of transitions metals due to the H_2 spillover when coupled with an increase in OVDs of the support.[42] Pt and Pd have been reported as the most efficient transition metals in lowering the reduction temperatures in H_2-TPR profiles.[42] Thus, the observed reduction in this range of temperature can be assigned to the reduction from PdO_y-CeO_{2-x} on the surface accompanied with the surface Ce^{4+} reduction.[43, 44] The maximum H_2

consumption peak at ~150 °C was due to the reduction of PdO and also Ce^{4+} in close vicinity to PdO clusters.[44, 45] This indicates the Pd on the activated Pd/CeO_{2-x} catalyst was likely dispersed finely on the support and exhibited strong interaction with ceria support.[44, 45] A small peak at ~100 °C in the H_2-TPR profile is assigned to the reduction of traces of isolated PdO phase present on the surface of ceria.[43] All these PdO_y species formed on the ceria surface are postulated to contribute to enhance the catalytic activity. Another small peak observed at ~480 °C is assigned to the reduction of the surface and subsurface of ceria.[35] In contrast, the H_2-TPR profile of the Pd/CeO_{2-x} catalyst after a 24 h. CO oxidation reaction indicates that most of its PdO_y species were reduced to metallic Pd. (Pd/CeO_{2-x} reduced in Figure 2.6) The profile exhibits a negative H_2 consumption peak in the range of 50 °C - 120 °C, suggesting the presence and decomposition of β-PdH.[43, 46] This indirectly implies the existence of metallic Pd in the reacted Pd/CeO_{2-x} catalyst. The metallic Pd species were likely formed from the reduction of PdO_y species on the activated catalyst by CO during the 24 h. reaction. The broad peak at 420 ºC is due to the H_2 reaction with the ceria support. Summing up the implications from the H_2-TPR profiles, the presence of PdO_y species on the surface is largely accountable for the higher catalytic activity of Pd/CeO_{2-x} nanorods during the CO oxidation reaction when compared with pure ceria nanorods.

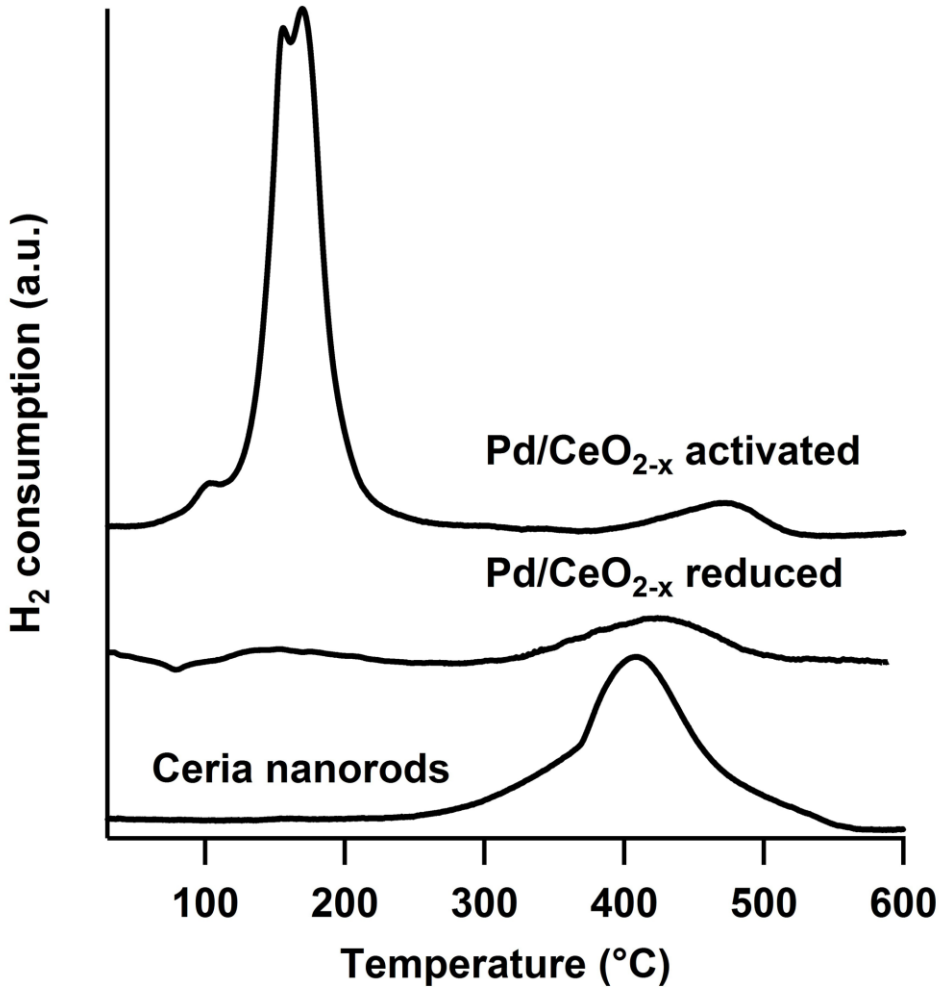

Figure 2.6 H_2-TPR profiles of activated 1 at.% Pd/CeO_{2-x}, reduced 1 at.% Pd/CeO_{2-x} after a 24 h. CO oxidation reaction, and pure ceria nanorods.

2.3.4 Oxidation States of Palladium in the Catalyst

The chemical states of the palladium in the 1 at.% Pd: CeO_{2-x} catalyst samples after activation, reduction by CO for 24 h., and regeneration for 24 h. under ambient conditions were investigated by analyzing the Pd 3*d* region in the XPS spectral data. (Figure 2.7) Pd^{2+} was found to be the predominant component of Pd species in these catalysts. A small portion of Pd^{4+} species, indicating the possible presence of PdO_2,[47,48] was also observed in the activated and regenerated catalysts, but not in the reduced sample. The binding energies of Pd $3d_{5/2}$ at around 337.3 eV and Pd $3d_{3/2}$ at around 342.2 eV represent the electronic transitions related to Pd^{2+}.[47, 49, 50] This suggests that the predominant Pd species in Pd/CeO_{2-x} catalyst is PdO. The shift of binding energy to a slightly higher value is likely due to the decrease of core-hole screening in small particles of the PdO. The strong interactions between Pd and cerium oxide support induced charge transfer from Pd to Ce-O may also cause the peak position shift.[47, 49, 50] In the XPS spectrum of the activated sample, the Pd $3d_{5/2}$ peak has a prominent shoulder at 338.4 eV, suggesting the presence of Pd in the +4 state.[47, 51] Similar shoulder of the Pd $3d_{3/2}$ peak also indicates the presence of Pd^{4+} species. After the catalyst was treated by a mixture of CO and oxygen for 24 h., the XPS spectrum of the CO reduced catalyst displays a small peak at 335.0 eV, which corresponds to Pd^0. The Pd^0 peak in the XPS spectrum of the regenerated catalyst is also found at the binding energy of 334.7eV. The corresponding Pd^0 signatures for the Pd $3d_{3/2}$ show much weaker intensities at the binding energy of around 340.8 eV. This is expected because of the larger degeneracy and higher intensity of the $3d_{5/2}$ peaks than those of the $3d_{3/2}$ peaks.[52] A Pd^{4+} peak shoulder reappears in the

XPS spectrum of the regenerated sample with a ~0.6 eV shift when compared with that of the activated catalyst.

The variations of Pd with different oxidation states in these three activated, reduced and regenerated catalysts provide clues about the underlying nature of the CO reaction and regeneration process. The Pd^0 species observed in the reduced sample implies that some PdO_y clusters with local structures similar to PdO and/or PdO_2 in the activated catalyst are reduced to Pd metal particles during the CO oxidation reaction. Pd^{4+} species are undetectable in the reduced sample, suggesting that the Pd^{4+} present in the activated catalyst was consumed by CO in the reduction reaction. Therefore, Pd^{4+} species are likely only formed on the very top surface of Pd/CeO_{2-x} catalyst, similar to the case of $LaFe_xPd_{1-x}O_3$ catalyst observed by Hamada and co-workers.[48] Interestingly, the main component of Pd species in the reduced catalyst is still Pd^{2+} and only a small peak of Pd^0 in the XPS data could be detected by the XPS. Oxygen present in the reaction gas flow or from the ceria support likely oxidized some Pd^0 to PdO at low temperatures when the Pd particles were in small sizes. The growth of these Pd metal particles into bigger ones was possibly suppressed by the sintering-resistant ceria support.[53, 54] The Pd^0 in the catalysts was found converted back to PdO_y after regeneration as indicated by the decrease in the intensity of Pd^0 peak. A Pd^{4+} shoulder peak is again present in the XPS spectrum of the regenerated catalysts, indicating the re-oxidation of the Pd species on the ceria support surface.

Considering the chemical state analysis of Pd in the Pd/CeO_{2-x} nanorod catalysts, we conclude that the regenerated sample is similar to the activated sample, which explains why the regenerated sample achieved as high as 80 % of its initial catalytic

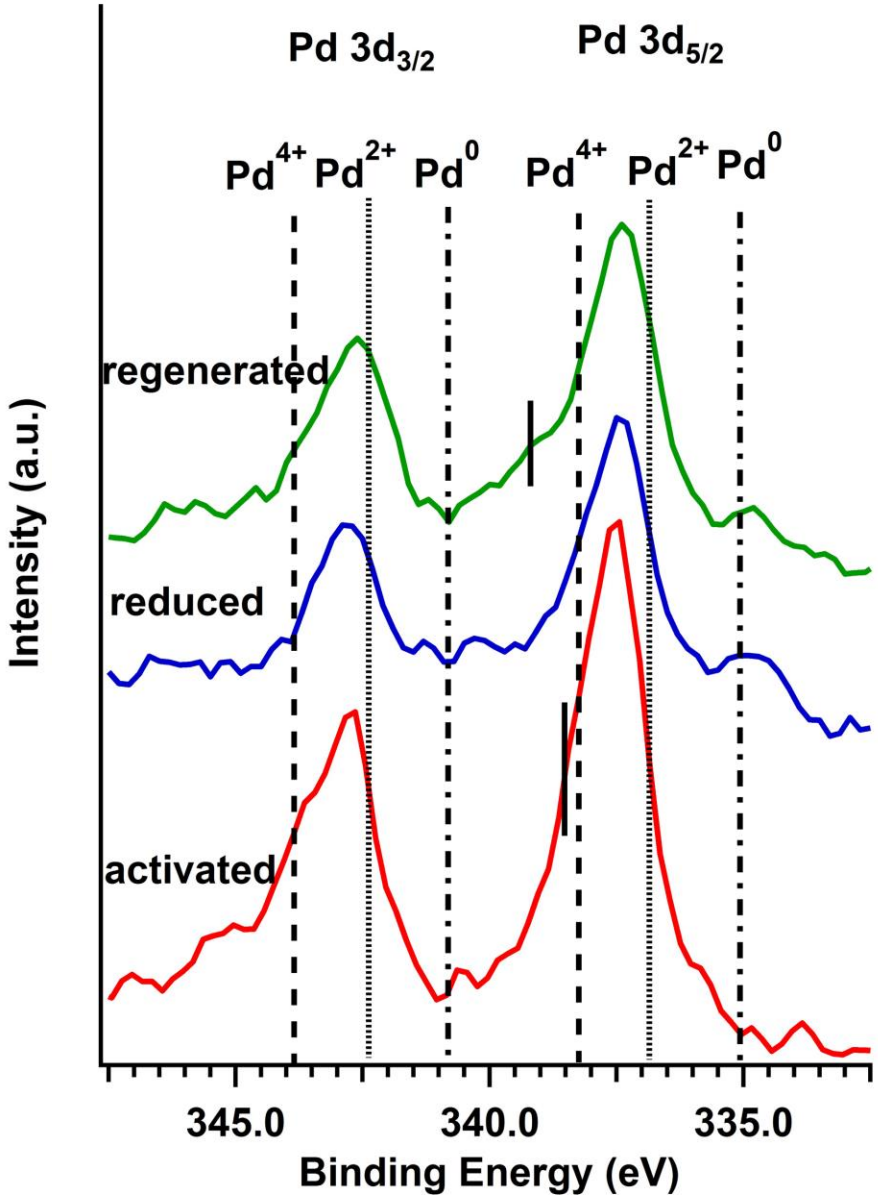

Figure 2.7 Pd 3*d* XPS spectra for the 1 at.% Pd/CeO_{2-x} nanorods. (activated)-catalyst after activated at 400 °C in simulated air (20 % O_2 and 80 % N_2), (reduced)-catalyst after being reduced by the CO oxidation reaction for 24 h. and (regenerated)-reduced catalyst after exposure in air under ambient conditions for 24 h. The fitting peaks are shown as dotted curves for each sample.

activity in Figure 2a. However, a binding energy shift of ~ 0.6 eV was observed for the Pd^{4+} peak in the XPS spectrum of the regenerated sample compared with that of the activated sample. A likely explanation is due to the change in the structure or cluster size of the Pd^{4+} species after the reaction regeneration cycle. Since the PdO_y was continually being reduced by CO to PdO and Pd during the 24 h. CO reaction run, the reduced Pd particles might migrate and spread out on the ceria surface and then segregated as small PdO_y particles after the regeneration.

2.3.5 Catalysts Atomic Structure and Chemical Environment

Changes in the physicochemical environment and valence states of the Pd in the Pd/CeO_{2-x} catalysts were studied by XANES. The valence states of Pd in the activated, reduced and regenerated of 1 at.% Pd/CeO_{2-x} catalysts together with reference materials Pd metal foil and palladium (II) oxide (PdO) were determined using Pd K-edge XANES spectra. (Figure 2.8) The Pd K-edge XANES probes the electronic transition from the 1*s* to 5*p* orbitals and is sensitive to the chemical state of the Pd atoms. The white line (a sharp feature at the top of the sharply rising part of the spectrum) at ~24.36 keV corresponds to the excitation of the Pd 1*s* electrons to the vacant 5*p*-states.[55] The XANES spectra of the three differently processed 1 at.% Pd/CeO_{2-x} samples show that Pd^{2+} is the dominant Pd species and Pd atoms in the catalysts have similar local environment as that of Pd in PdO based on the similarities in absorption edges and oscillation characters. We also notice that the energies of the resonance peaks of Pd/CeO_{2-x} catalyst samples are all slightly shifted to higher level (3 eV) than that of the PdO reference. This can be attributed to the shorter Pd-O bond length due to the quantum confinement effect.[56] Among the three XANES spectra of Pd/CeO_{2-x} samples, no apparent differences

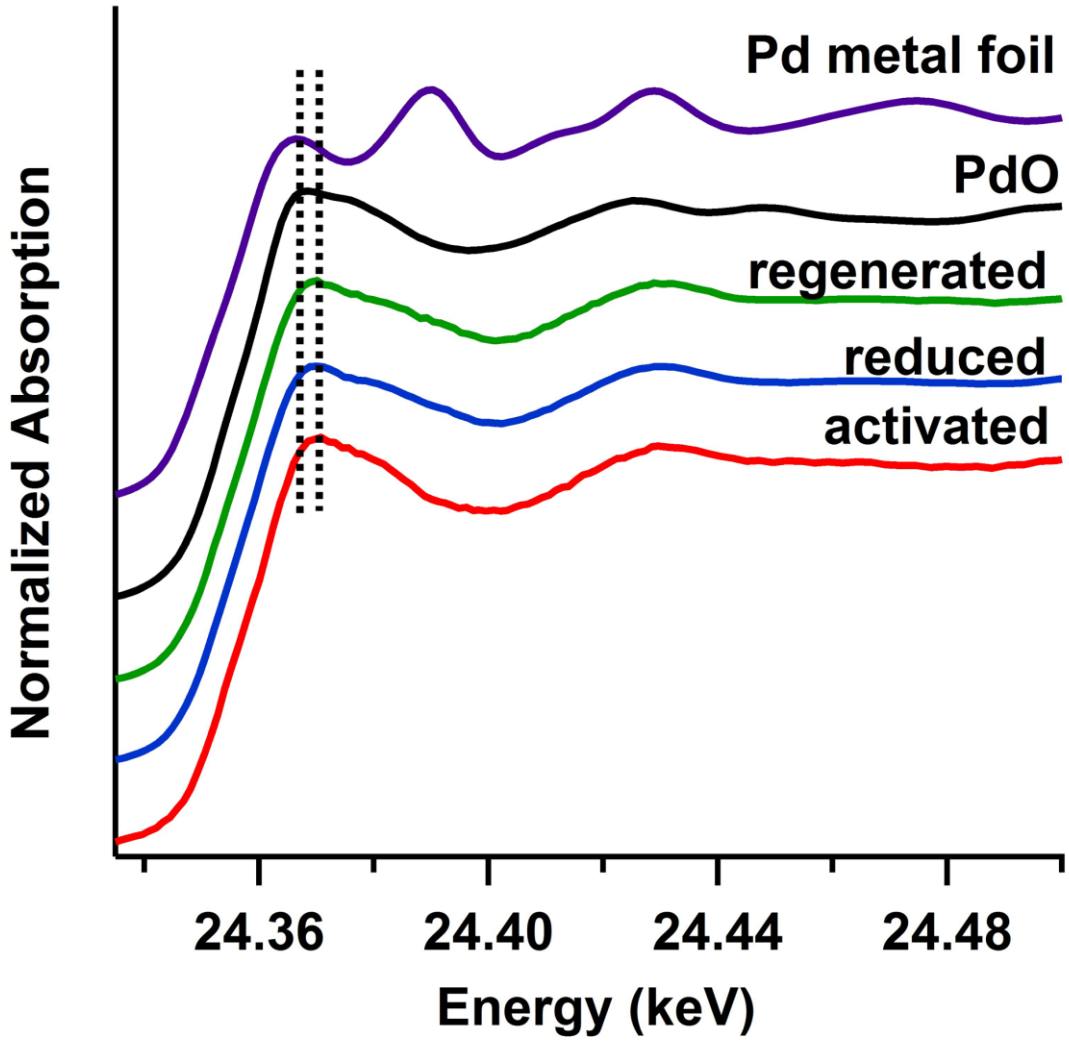

Figure 2.8 Normalized Pd K-edge XANES spectra of 1 at.% Pd/CeO_{2-x} nanorods and the reference sample PdO and Pd metal. The vertical dotted lines indicate the strong resonance contributed by the excitation of Pd 1*s* electrons to vacant 5*p* states. The shift of the white line to higher energies indicates that the Pd atoms in the samples are more oxidized than that in the PdO reference.

are detected due to the limitation of energy resolution as well as sample similarities.

The local structure and chemical environments of Pd in these three 1 at.% Pd/CeO_{2-x} nanorods catalysts were investigated by EXAFS. An established data reduction method was used to extract the χ-functions from the raw experimental data. The χ-functions of the Pd K-edge EXAFS were then Fourier-transformed into real space (R-space) data. Local structural parameters were quantitatively extracted from the EXAFS functions using an improved curve-fitting procedure with back scattering amplitude and phase shifts functions obtained from the *FEFF* software.[57-59] The Fourier transforms of Pd K-edge k^3-weighted $\chi(k)$ for the EXAFS spectra depict the differences in the local structures of Pd atoms between the 1 at.% Pd/CeO_{2-x} samples, the PdO bulk and Pd metal. (Figure 2.9 and Table 2.1) The R-space magnitude data of the catalyst samples shows several main peaks in the R range from 0 to 5 Å. The first peak around 1.5 Å corresponds to the Pd-O single scattering from the first shell of PdO. The second peak around R = 3.0 Å represents a Pd-Pd scattering in the second shell of PdO. However, the relative magnitudes of the second peaks in the catalysts' R-space data are much smaller than those from the PdO reference and their peak positions are slightly different. This suggests that the local environments of Pd from the PdO_y clusters in the 1 at.% Pd/CeO_{2-x} catalysts are different from that of PdO bulk. These differences can be explained by the presence of a highly disordered PdO-like structure due to the influence of surrounded Ce atoms in the catalyst which are possibly associated with the strong interaction between Pd atoms and the ceria support. The data of activated Pd/CeO_{2-x} sample was fitted using only the PdO model ($P4_2/mmc$) while the data of the other two samples were applied both PdO

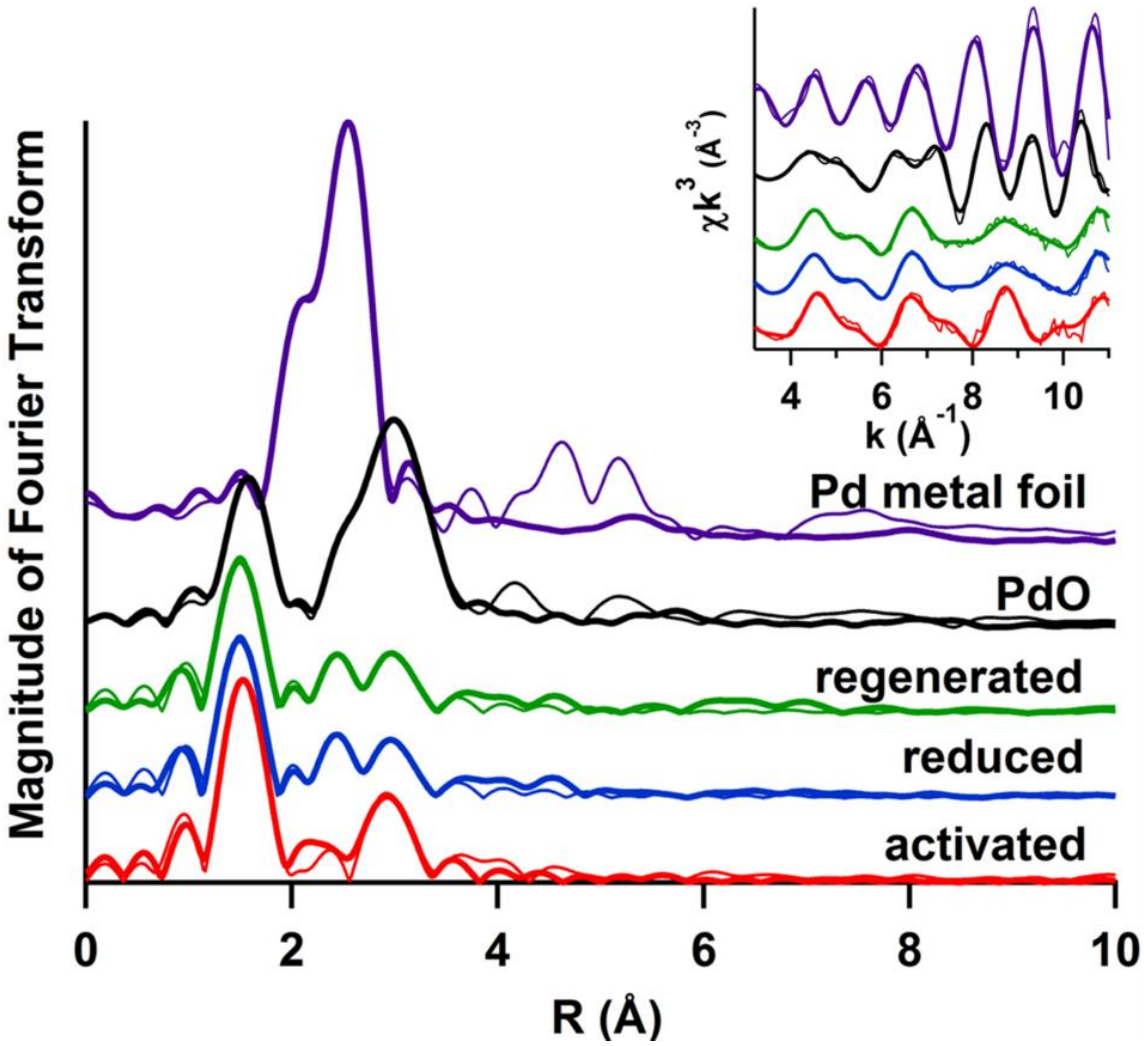

Figure 2.9 Fourier transformed Pd K-edge EXAFS data of activated Pd/CeO_{2-x}, reduced Pd/CeO_{2-x}, regenerated Pd/CeO_{2-x}, and PdO and Pd metal standard samples (from the bottom to the top). The inset image is showing the EXAFS data of the three samples in k space. (Thick lines: data; thin lines: fittings)

Table 2.1 Structural parameters of Pd/CeO_{2-x} catalysts, PdO and Pd metal foil standard samples obtained from EXAFS analysis. [a] ICDD 04-007-6608 is used to obtain coordination of Pd atoms in PdO crystal. The underline marks indicate parameters fixed when processing the fitting analysis.

1% Pd/CeO_{2-x} samples	Bond	Coordination number (N)	Radial distance (R) (Å)	Debye-Waller factor (σ^2) (10^{-3} Å^2)
Activated	Pd-O	4.3 ± 0.3	1.99 ± 0.01	0.9 ± 0.5
	Pd-Pd	6.9 ± 1.3	2.98 ± 0.01	9.6 ± 0.7
Reduced	Pd-O	3.0 ± 0.2	1.99 ±0.01	4.4 ± 0.2
	Pd-Pd	3.4 ± 0.4	2.68 ± 0.01	9.4 ± 0.4
	Pd-Pd	5.5 ± 0.8	<u>2.98</u>	11.7 ± 0.5
Regenerated	Pd-O	3.2 ±0.2	1.99 ± 0.01	1.2 ± 0.5
	Pd-Pd	2.9 ± 0.4	2.68 ± 0.03	8.6 ± 0.6
	Pd-Pd	6.3 ± 0.9	<u>2.98</u>	12.4 ± 0.5
Theoretical	Pd-O	4	2.02 ± 0.01	1.6 ± 0.5
PdO[a]	Pd-Pd	4	<u>3.03</u>	4.8 ± 0.3
	Pd-Pd	8	<u>3.42</u>	3.0± 0.4
	Pd-O	8	<u>3.64</u>	15.8 ± 5.3
Pd metal foil	Pd-Pd	11.0 ± 1.0	2.73 ± 0.01	4.6 ± 0.5

and Pd metal ($Fm\bar{3}m$) models in the fitting. It is because the Pd metal model better captured the two smaller peaks in the range of R = 2 - 3 Å and XPS indicated the presence of Pd^0 in these samples. The second peaks in the R-space data of reduced and regenerated samples are well fitted by taking the first shell of Pd-Pd correlation belonging to the Pd-metal-like phase and the second shell of Pd-Pd from reference PdO. This model leads to the detection of Pd metal with Pd-Pd bond of length ~2.68 Å which is close to that found in Pd metal foil (~2.73 Å). Note that the Pd-O- Ce bond wasn't applied in our data fitting analysis because the spectra of all three Pd/CeO_{2-x} catalysts exhibit a strong peak at 2.98 Å which is close to the 3.03 Å Pd-Pd bond in PdO and unlike the 3.18 Å of Pd-O-Ce bond reported by Machida group.[60] Also, the PdO_2 ($P4_2/mnm$) model was not applied either so as to avoid over-interpreting the data because it does mismatch any peak-positions in the experimental spectra in a meaningful manner.

The intensity of Pd-O bond peak in the activated sample is stronger than those of the other two, implying that larger amount of PdO_y species are present in the activated catalyst. The variations of Pd-O and Pd-Pd bond features in the regenerated and the activated samples indicate that the regenerated sample is not identical to the activated one. The differences are likely caused by the changes in the structure or the cluster size of PdO_y after the activation and the regeneration treatment. However, the "changed" PdO_y still contributes to the restored CO oxidation catalytic activity as shown in Figure 2.4b.

The local structural parameters of the first and second nearest neighboring atoms around Pd atoms in the Pd/CeO_{2-x} catalysts under different treatments at room temperature are shown in Table 1. The average lengths of Pd-O bonds are determined in these three catalysts to be slightly shorter than that of PdO standard. This indirectly

implies the presence of smaller particles of PdO in those catalysts. The obtained Debye-Waller factors and energy shifts (See Table 2.2) from the samples are larger than those of the PdO reference, implying that higher disordered PdO_y species are formed on the ceria support in the catalysts samples. Since the activated sample has more oxygen coordinated to the Pd atoms, more oxidized Pd species are expected to exist in this sample than the other two. The regenerated sample exhibits slightly higher first shell Pd-O coordination number than that of reduced one, which indicates that the regenerated sample is more oxidized by the air under the ambient condition and thus demonstrates the oxidative ability of the regenerated sample towards CO oxidation.

The fitted EXAFS models imply that both the reduced and regenerated samples clearly exhibit one extra Pd-Pd coordination shell with an average radial distance of ~2.68 Å than the freshly activated sample. This indicates that more reduced species exist, likely as Pd nanoparticles, in these two samples because of their CO reduction treatment. Though the reduced sample is expected to have more or larger Pd metal particles because of the larger Pd-Pd coordination number fitted by the first shell of Pd metal model, the obtained atomic structural parameters for the reduced and regenerated samples are similar. This similarity can be explained by the mild oxidation that occurred on the very top surface of the regenerated catalyst after the 24 h. regeneration process under the ambient condition.

Table 2.2 Structural parameters of Pd/CeO_{2-x} catalysts, PdO and Pd metal foil standard samples obtained from Pd K edge EXAFS analysis. The underline marks indicate parameters fixed when processing the fitting analysis.[a] The larger energy shift fitting number is due to the high disorder and small particle size of PdO in the Pd/CeO_{2-x} catalysts.

1 at.% Pd/CeO_{2-x} samples	Bond	Coordination number (N)	Radial distance (R) (Å)	Debye-Waller factor (10^{-3} Å^2)	Energy shift (ΔE) (eV)	S_0^2 (Ampli-tude)
PdO	Pd-O	4	2.02 ± 0.01	1.6 ± 0.5	5.9 ± 1.1	0.85
	Pd-Pd	4	3.03	4.8 ± 0.3	1.3 ± 0.7	
	Pd-Pd	8	3.42	3.0 ± 0.4	-0.2 ± 0.5	
	Pd-O	8	3.64	15.8 ± 5.3	-3.8± 2.5	
Pd foil	Pd-Pd	11.0 ± 1.0	2.73 ± 0.01	4.6 ± 0.5	-0.2 ± 0.5	0.85
Activated	Pd-O	4.3 ± 0.3	1.99 ± 0.01	0.9± 0.5	5.8 ± 1.1	0.85
	Pd-Pd	6.9 ± 1.3	2.98 ± 0.01	9.6 ± 0.7	5.5 ± 1.4[a]	
Reduced	Pd-O	3.0 ± 0.2	1.99 ± 0.01	4.4 ± 0.2	3.8 ± 1.1	0.85
	Pd-Pd	3.4 ± 0.4	2.68 ± 0.01	9.4 ± 0.4	-9.3 ± 5.0	
	Pd-Pd	5.5 ± 0.8	2.98	11.7 ± 0.5	15.5 ±0.6[a]	
Regener-ated	Pd-O	3.2 ± 0.2	1.99 ± 0.01	1.2 ± 0.5	4.1 ±1.1	0.85
	Pd-Pd	2.9 ± 0.4	2.68 ± 0.01	8.6 ± 0.6	-9.4 ± 5.0	
	Pd-Pd	6.3 ± 0.9	2.98	12.4 ± 0.5	15.4 ± 0.6[a]	

2.3.6 Relationship between Regenerative Ability and Density of Oxygen Vacancy Defect of Catalysts

According to our XPS and XAFS data analysis, PdO_y species are responsible for the regenerative catalytic activity of the Pd/CeO_{2-x} catalyst. The formation of PdO_y in the regeneration process was found to be also strongly dependent on the ceria support because not all of the metal oxide based Pd catalysts, such as Pd/Al_2O_3,[20] exhibited the regenerative ability towards CO oxidation. Previous studies of ceria-based catalysts focused on the reversible changes of oxidation state and re-dispersion of supported metal which were attributed to the strong interaction between metal and support.[25, 35] However, current literature provides little information about the correlation between the intrinsic property of ceria support and the associated oxidative change and re-dispersion of supported metals. In addition, the published studies usually employed different supports, such as Al_2O_3,[20, 27] to compare with ceria in order to deduce the functions of ceria support in the regeneration process. These comparisons introduced more unknown factors in identifying the effect of ceria support on the supported metals and metal oxides.

Oxygen vacancy defects (OVDs) in oxide-based catalyst systems have been proposed to play different roles in forming catalytically active sites and facilitating the diffusion of active species during catalyzed reactions. For example, a density functional theory study for the regenerative catalyst $LaFe_{1-x}Pd_xO_{3-y}$ by Hamada *et al* showed that OVDs in the perovskite $LaFeO_{3-y}$ can assist and stabilize surface segregation of Pd atoms which in turn promote the formation of $LaPdO_{3-y}$ in the vicinity of the $LaFe_{1-x}Pd_xO_{3-y}$ surface.[48] Motivated by previous studies on the significance of OVDs in the regenerative catalysts, we sought to confirm the existence of a similar positive correlation between the

density of OVDs in the Pd/CeO_{2-x} nanorod catalyst and its regenerative ability. Previously, we demonstrated that low-pressure heat treatment could be applied to increase the OVD density in ceria nanorods.[61] In the present study, we prepared two batches of Pd/CeO_{2-x} nanorod catalysts with different levels of OVD density in the ceria support by activating these catalysts using vacuum-annealing treatment at two different pressures, 2.0 Torr (low vacuum) and 0.07 Torr (high vacuum). (See Experimental Section) Fitted EXAFS data in Table 2.3 shows that the coordination numbers of first shell Ce-O in the low- and high-vacuum activated catalysts (6.2 and 6.3) are both much smaller than that of the theoretical bulk ceria (8), indicating a large deficiency of oxygen atoms around the cerium atoms in both samples. XPS was utilized to further differentiate the relative OVD densities on the surfaces of these two catalyst supports because this surface sensitive technique can be applied to analyze the % of Ce^{3+} on material's surface which has been positively correlated to the amount of OVDs on the surface of ceria.[62] Significantly, the ceria surface of high-vacuum activated Pd/CeO_{2-x} sample was found to have 40 % Ce^{3+}, which almost doubles the surface concentration of Ce^{3+} in the low-vacuum activated sample (21 %). (Table 2.4 and Figure 2.10) This data thus confirms that the ceria support of Pd/CeO_{2-x} activated under a higher-vacuum condition has higher density of OVDs than the one activated at lower vacuum.

Table 2.3 Parameters of the local structure around Ce atoms of high- and low-vacuum activated ceria nanorods, and bulk samples obtained from curve fitting of the Ce L_3-edge EXAFS. [b] ICDD card 04-013-4361 is used to obtain the Ce atoms coordination in CeO2 crystal.

1 at.% Pd/CeO_{2-x} samples	Bond	Coordination number (N)	Radial distance (R) (Å)	Debye-Waller factor (σ^2) (10^{-3} Å^2)
Low-vacuum activated at 2.0 Torr	Ce-O	6.2 ± 0.1	2.300 ± 0.002	10.3 ± 1.1
	Ce-Ce	6.5 ± 0.7	3.783 ± 0.002	17.4 ± 0.5
High-vacuum activated at 0.07 Torr	Ce-O	6.3 ± 0.1	2.294 ± 0.005	2.4 ± 0.2
	Ce-Ce	7.4 ± 0.4	3.815 ± 0.005	1.3 ± 0.2
Theoretical CeO_2 [b]	Ce-O	8	2.34	-
	Ce-Ce	12	3.83	-

Table 2.4 Comparison of the surface area and Ce^{3+} concentration on the surface of high- and low- vacuum activated 1% Pd: CeO_{2-x} samples and their respective regenerative ability.

1% Pd: CeO_{2-x} samples	Surface area (m^2/g)	% of Ce^{3+} on the ceria surface	Regenerated level of catalytic activity at RT
Low-vacuum-activated at 2.0 Torr	102	21 %	60~80 %
High-vacuum-activated at 0.07 Torr	113	40 %	100 %

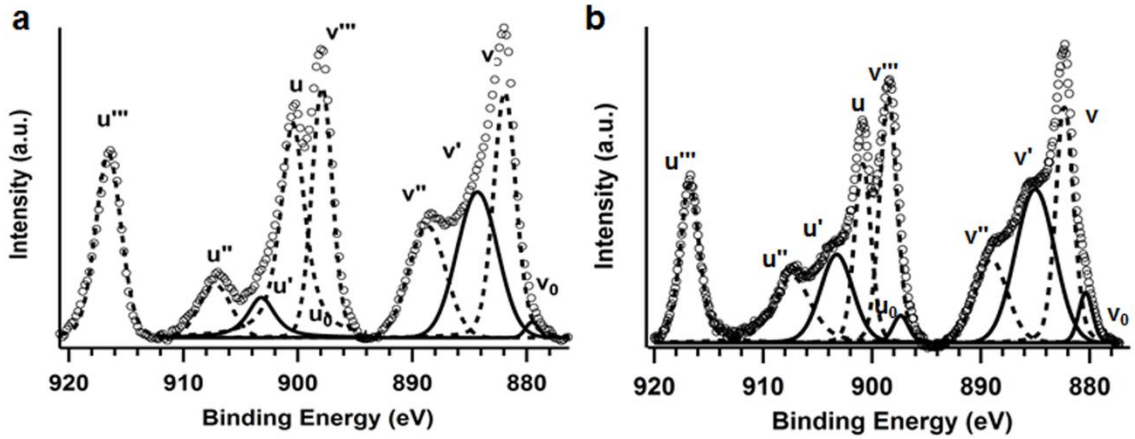

Figure 2.10 Fitted Ce 3*d* core level XPS spectra of 1 at.% Pd/CeO_{2-x} catalyst activated at (a) low-vacuum pressure (2.0 Torr) and (b) high-vacuum (0.07 Torr). The XPS spectra were calibrated against both carbon 1s peak at 284.8 eV and Ce u''' peak at 916.7 eV due to concerns of the over-compensation effect. Insignificant difference was observed. By quantifying the relative areas of the Ce^{3+} peaks to the total area of Ce^{3+} and Ce^{4+} peaks, we can estimate the fraction of Ce^{3+} on the surface of the catalyst and approximate the changes in the valence of cerium in the oxide samples. The binding energy of Ce ($3d_{5/2}$, $3d_{3/2}$) levels for Ce^{4+} are marked by v, v'', v''' and u, u'', u''' (represented by dotted line). Peaks v_0, v' and u_0, u' (represented by solid line) refer to Ce $3d_{5/2}$ and $3d_{3/2}$, respectively, and are characteristics for Ce^{3+}.

The H_2-TPR profiles of Pd/CeO_{2-x} catalysts activated at high and low-vacuum conditions reveal that the high-vacuum-activated catalyst contains surface species more active for CO oxidation, though both of them are expected to have very similar overall atomic composition. Figure 2.11 shows that the H_2-TPR profile of high-vacuum activated sample has a much broader H_2-consumption peak than that of the low-vacuum activated sample in the range of 70 °C to 200 °C. Broader H_2-consumption peaks for supported Pd catalysts typically have been reported to indicate the presence of several different Pd species including isolated PdO phase and PdO_y species with various strength of interaction with the ceria support or different particle size are involved in the H_2 reduction.[35] Thus, the high-vacuum activated sample likely possesses a larger variety of Pd species formed on the ceria surface than the one activated at low vacuum. Interestingly, the H_2 consumption of high and low-vacuum activated catalysts were found to have a ratio of *ca.* 1:1, suggesting these two catalysts has similar amount of palladium species active for oxidizing H_2.

Our experimental data confirms that Pd/CeO_{2-x} nanorod catalysts with ceria support containing higher surface density of OVDs exhibit larger degree of regenerative ability towards the room temperature CO oxidation reaction. The high-vacuum activated catalyst was shown to recover 100 % of the initial CO oxidation activity after exposure to ambient conditions for 24 h., while the low-vacuum activated Pd/CeO_{2-x} could only attain 60 – 80 % of regenerative ability after similar treatments. (See Figure 2.12) Note that since both evaluated catalysts have similar surface area (102 m^2/g for the low-vacuum activated catalyst vs. 113 m^2/g for the high-vacuum activated catalyst), we reason that

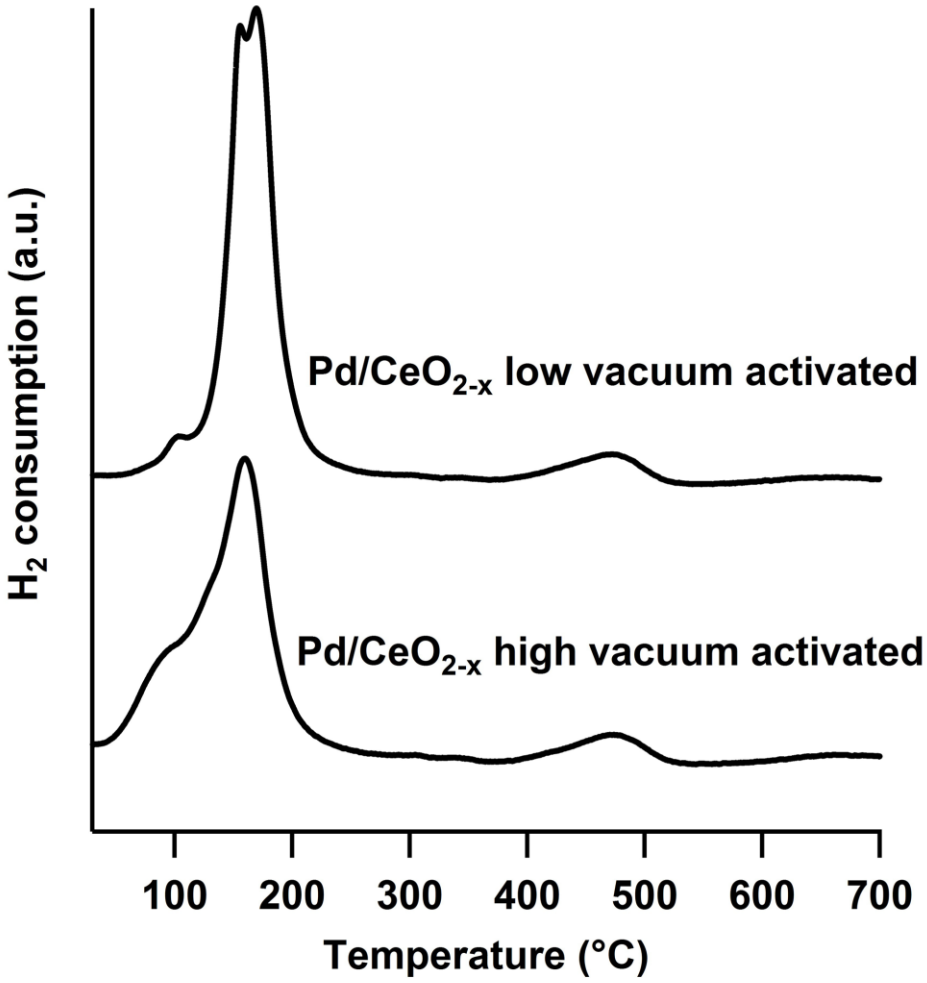

Figure 2.11 H_2-TPR profiles of Pd/CeO_{2-x} catalysts activated at high vacuum (0.07 Torr) and low vacuum (2.0 Torr), respectively.

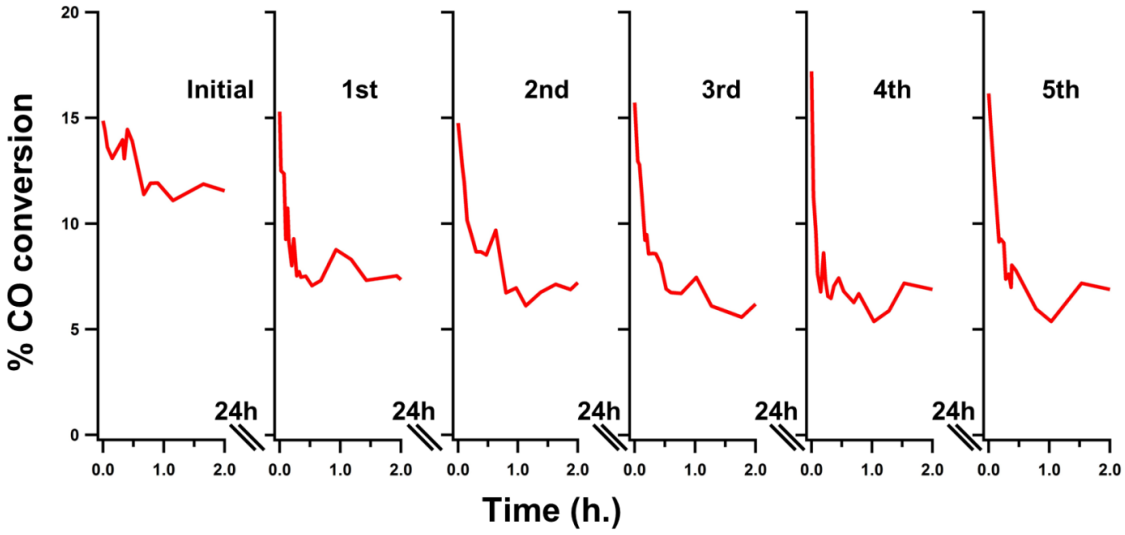

Figure 2.12 Series of CO catalytic reactions over 1 at.% Pd/CeO_{2-x} nanorod catalyst prepared by the method described in the text. The catalyst was activated under high-vacuum pressure (0.07 Torr). The CO oxidation reaction was performed at 20 °C for 24 h. In between successive reaction runs, the catalyst was subjected to regenerative treatment by exposure to air under ambient conditions for 24 h.

this difference in surface areas of these two catalysts is too small and not significant enough to yield the much larger difference in the observed regeneration performance. As indicated in our XPS and XAFS data, the disordered PdO_y formed on the surface is deduced to be responsible for the regeneration of catalysts. Since the formation of PdO_y species is strongly dependent on the OVDs of ceria according to our H_2-TPR data, therefore, we postulate that the regenerative ability of the Pd/CeO_{2-x} catalyst is strongly correlated with the OVDs in the ceria support.

From the above discussions, we postulate that OVDs of the Pd/CeO_{2-x} catalysts likely function to assist the formation of PdO_y species under oxidative environments on the catalysts' surface to maintain their high catalytic activity. During the CO oxidation reaction, the Pd^{2+} species were reduced to Pd^0 species which then aggregated as Pd metallic particles on the ceria surface. However, when exposed to air, the oxygen vacancy sites promoted these small Pd metallic particles to coordinate with the neighboring oxygen atoms in the ceria to form PdO_y species,[48] which are the key catalytic components in recovering the high activity over CO oxidation at room temperature. An increase in the OVD density could further enhance the formation of PdO_y species under an oxidative environment[48,63] and facilitate the catalyst regeneration process. Hence, the synergy between the Pd species and the OVDs in the ceria support possibly plays a significant role in the self-regeneration process of the Pd/CeO_{2-x} catalysts towards CO oxidation under ambient conditions.

2.4 Conclusion

The regenerative property of the Pd/CeO_{2-x} nanorod catalyst for the CO oxidation reaction at room temperature was demonstrated to be highly reproducible and tunable by controlling the oxygen vacancy defect (OVD) density of the ceria nanorod support. Our XPS and XANES spectroscopic studies on the chemical states of the elements and atomic structure of this catalyst lead to new insights into the catalytically active Pd species on the catalysts and the synergistic interactions between these Pd species and the ceria nanorods for the observed regeneration phenomena. Disordered palladium oxides (PdO_y) were determined to be the major catalytically active Pd species on the ceria support at room temperature. The formation of Pd species with high oxidation states (Pd^{2+} and Pd^{4+}) and highly disordered PdO_y in the Pd/CeO_{2-x} catalyst were found responsible for enabling this catalyst to promote the catalytic CO oxidation reaction at room temperature. The regeneration of the Pd/CeO_{2-x} catalysts after usage was illustrated to be achieved by exposing the catalyst to ambient conditions for 24 h. This treatment consequently oxidized the Pd^0 species formed during the CO reaction back to the active PdO_y species on the catalyst surface. Significantly, higher degree of regenerative ability was found in Pd/CeO_{2-x} catalysts with ceria support containing higher density of OVDs.

Based on the atomic structures and oxidation state data of the Pd/CeO_{2-x} catalysts after different stages of catalyst activation, reaction and regeneration, we hypothesize that the OVDs in ceria nanorods facilitate the formation of PdO_y on the ceria surface. Upon exposure of the used catalysts to ambient conditions, the highly defective ceria with significant oxidizing power possibly re-oxidizes the reduced metal particles into disordered PdO_y. Our atomic structure findings may help understanding the Pd-

containing ceria for other chemical reactions, such as nitrogen oxide reduction in automobile exhaust[64, 65] and C-C bond formation reactions in organic chemistry.[31, 66, 67] Hence, we expect that our demonstrated evidence of using ceria support with high density of OVDs for enhancing the regenerative ability of metal and metal oxide catalysts may inspire new designs of regenerative catalysts. Such a catalyst design strategy is expected to be applicable to altering the catalytic property and regenerative ability of other ceria supported catalysts.

2.5 References

1 P. E. Garrou, *Chem. Rev.*, 1985, **85**, 171-185.

2 P. Forzatti and L. Lietti, *Catal. Today*, 1999, **52**, 165-181.

3 C. H. Bartholomew, *Appl. Catal., A*, 2001, **212**, 17-60.

4 Q. Xu, K. C. Kharas, B. J. Croley and A. K. Datye, *ChemCatChem*, 2011, **3**, 1004-1014.

5 K. Heidkamp, M. Aytemir, K. D. Vorlop and U. Prusse, *Catal. Sci. Technol.*, 2013, **3**, 2984-2992.

6 D. Ciuparu, M. R. Lyubovsky, E. Altman, L. D. Pfefferle and A. Datye, *Catal. Rev.*, 2002, **44**, 593-649.

7 C. H. Bartholomew, *Appl Catal a-Gen*, 2001, **212**, 17-60.

8 P. Albers, J. Pietsch and S. F. Parker, *J. Mol. Catal. A: Chem.*, 2001, **173**, 275-286.

9 G. A. Somorjai, A. M. Contreras, M. Montano and R. M. Rioux, *Proc. Natl. Acad. Sci. U.S.A.*, 2006, **103**, 10577-10583.

10 A. T. Bell, *Science*, 2003, **299**, 1688-1691.

11 A. J. Forman, J.-N. Park, W. Tang, Y.-S. Hu, G. D. Stucky and E. W. McFarland, *ChemCatChem*, 2010, **2**, 1318-1324.

12 J.-N. Park, A. J. Forman, W. Tang, J. Cheng, Y.-S. Hu, H. Lin and E. W. McFarland, *Small*, 2008, **4**, 1694-1697.

13 B. Li, W.-Z. Weng, Q. Zhang, Z.-W. Wang and H.-L. Wan, *ChemCatChem*, 2011, **3**, 1277-1280.

14 M. Cargnello, T. Montini, S. Polizzi, N. L. Wieder, R. J. Gorte, M. Graziani and P. Fornasiero, *Dalton Trans.*, 2010, **39**, 2122-2127.

15 W. J. Shen and Y. Matsumura, *Phys. Chem. Chem. Phys.*, 2000, **2**, 1519-1522.

16 Y. Luo, Y. Xiao, G. Cai, Y. Zheng and K. Wei, *Catal. Sci. Technol.*, 2011, **1**, 1362-1366.

17 T. Bunluesin, R. J. Gorte and G. W. Graham, *Appl. Catal., B*, 1998, **15**, 107-114.

18 O. Pozdnyakova, D. Teschner, A. Wootsch, J. Krohnert, B. Steinhauer, H. Sauer, L. Toth, F. C. Jentoft, A. Knop-Gericke, Z. Paal and R. Schlogl, *J. Catal.*, 2006, **237**, 17-28.

19 Y. Dai, B. Lim, Y. Yang, C. M. Cobley, W. Li, E. C. Cho, B. Grayson, P. T. Fanson, C. T. Campbell, Y. Sun and Y. Xia, *Angew. Chem. Int. Ed.*, 2010, **49**, 8165-8168.

20 Y. Nishihata, J. I. Mizuki, T. Akao, H. Tanaka, M. Uenishi, M. Kimura, T. Okamoto and N. Hamada, *Nature*, 2002, **418**, 164-167.

21 M. Uenishi, M. Taniguchi, H. Tanaka, M. Kimura, Y. Nishihata, J. Mizuki and T. Kobayashi, *Appl. Catal., B*, 2005, **57**, 267-273.

22 H. Tanaka, M. Uenishi, M. Taniguchi, I. Tan, K. Narita, M. Kimura, K. Kaneko, Y. Nishihata and J. I. Mizuki, *Catal. Today*, 2006, **117**, 321-328.

23 H.-P. Zhou, H.-S. Wu, J. Shen, A.-X. Yin, L.-D. Sun and C.-H. Yan, *J. Am. Chem. Soc.*, 2010, **132**, 4998-4999.

24 K. Yoon, Y. Yang, P. Lu, D. Wan, H.-C. Peng, K. Stamm Masias, P. T. Fanson, C. T. Campbell and Y. Xia, *Angew. Chem. Int. Ed.*, 2012, **51**, 9543-9546.

25 M. Hatanaka, N. Takahashi, N. Takahashi, T. Tanabe, Y. Nagai, A. Suda and H. Shinjoh, *J. Catal.*, 2009, **266**, 182-190.

26 H. C. Yao and Y. F. Y. Yao, *J. Catal.*, 1984, **86**, 254-265.

27 Y. Nagai, T. Hirabayashi, K. Dohmae, N. Takagi, T. Minami, H. Shinjoh and S. Matsumoto, *J. Catal.*, 2006, **242**, 103-109.

28 A. Trovarelli, *Catal. Rev.*, 1996, **38**, 439-520.

29 Y. Y. Zhou, N. J. Lawrence, L. Wang, L. M. Kong, T. S. Wu, J. Liu, Y. Gao, J. R. Brewer, V. K. Lawrence, R. F. Sabirianov, Y. L. Soo, X. C. Zeng, P. A. Dowben, W. N. Mei and C. L. Cheung, *Angew. Chem. Int. Ed.*, 2013, **52**, 6936-6939.

30 G. Wang, L. Wang, X. Fei, Y. Zhou, R. F. Sabirianov, W. N. Mei and C. L. Cheung, *Catal. Sci. Technol.*, 2013, **3**, 2602-2609.

31 L. Vivier and D. Duprez, *ChemSusChem*, 2010, **3**, 654-678.

32 S. Sato, F. Sato, H. Gotoh and Y. Yamada, *ACS Catal.*, 2013, **3**, 721-734.

33 H. Yahiro, Y. Baba, K. Eguchi and H. Arai, *J. Electrochem. Soc.*, 1988, **135**, 2077-2080.

34 Y. Zhou, C. L. Menendez, M. J. F. Guinel, E. C. Needels, I. Gonzalez-Gonzalez, D. L. Jackson, N. J. Lawrence, C. R. Cabrera and C. L. Cheung, *RSC Advances*, 2014, **4**, 1270-1275.

35 M. Kurnatowska, L. Kepinski and W. Mista, *Appl. Catal., B*, 2012, **117**, 135-147.

36 H. S. Roh, A. Platon, Y. Wang and D. L. King, *Catal. Lett.*, 2006, **110**, 1-6.

37 Y. Nagai, K. Dohmae, Y. Ikeda, N. Takagi, N. Hara, T. Tanabe, G. Guilera, S. Pascarelli, M. A. Newton, N. Takahashi, H. Shinjoh and S. i. Matsumoto, *Catal. Today*, 2011, **175**, 133-140.

38 H. Tanaka, *Catal. Surv. Asia*, 2005, **9**, 63-74.

39 J. Xu, J. Harmer, G. Li, T. Chapman, P. Collier, S. Longworth and S. C. Tsang, *Chem. Commun.*, 2010, **46**, 1887-1889.

40 H.-X. Mai, L.-D. Sun, Y.-W. Zhang, R. Si, W. Feng, H.-P. Zhang, H.-C. Liu and C.-H. Yan, *J. Phys. Chem. B*, 2005, **109**, 24380-24385.

41 A. Trovarelli, ed., *Catalysis by Ceria and Related Materials*, Imperial College Press, London, 2002.

42 W. C. Conner and J. L. Falconer, *Chem. Rev.*, 1995, **95**, 759-788.

43 X. Xiao, J. Lu, X. Su, M. Guo and M. Luo, *Acta Phys. Chim. Sin.*, 2009, **25**, 561-566.

44 H. Q. Zhu, Z. F. Qin, W. J. Shan, W. J. Shen and J. G. Wang, *J. Catal.*, 2004, **225**, 267-277.

45 M. Luo, Z. Hou, X. Yuan and X. Zheng, *Catal. Lett.*, 1998, **50**, 205-209.

46 N. S. Babu, N. Lingaiah, N. Pasha, J. V. Kumar and P. S. S. Prasad, *Catal. Today*, 2009, **141**, 120-124.

47 S.-H. Oh and G. B. Hoflund, *J. Phys. Chem. A*, 2006, **110**, 7609-7613.

48 I. Hamada, A. Uozumi, Y. Morikawa, A. Yanase and H. Katayama-Yoshida, *J. Am. Chem. Soc.*, 2011, **133**, 18506-18509.

49 K. R. Priolkar, P. Bera, P. R. Sarode, M. S. Hegde, S. Emura, R. Kumashiro and N. P. Lalla, *Chem. Mater.*, 2002, **14**, 2120-2128.

50 A. Gupta, A. Kumar, U. V. Waghmare and M. S. Hegde, *Chem. Mater.*, 2009, **21**, 4880-4891.

51 L. Meng, A. Jia, J. Lu, L. Luo, W. Huang and M. Luo, *J. Phys. Chem. C*, 2011, **115**, 19789-19796.

52 S. Hofmann, in *Auger- and X-Ray Photoelectron Spectroscopy in Materials Science*, Springer Berlin Heidelberg, Berlin, 2013, vol. 49.

53 N. R. Shiju, *ChemCatChem*, 2011, **3**, 112-114.

54 J. A. Farmer and C. T. Campbell, *Science*, 2010, **329**, 933.

55 K. Paredis, L. K. Ono, F. Behafarid, Z. F. Zhang, J. C. Yang, A. I. Frenkel and B. R. Cuenya, *J. Am. Chem. Soc.*, 2011, **133**, 13455-13464.

56 S. I. Zabinsky, J. J. Rehr, A. Ankudinov, R. C. Albers and M. J. Eller, *Phys. Rev. B*, 1995, **52**, 2995-3009.

57 J. J. Rehr, *Jpn. J. Appl. Phys.*, 1993, **32**, 8-12.

58 J. J. Rehr, R. C. Albers and S. I. Zabinsky, *Phys. Rev. Lett.*, 1992, **69**, 3397-3400.

59 J. J. Rehr, J. Mustre de Leon, S. I. Zabinsky and R. C. Albers, *J. Am. Chem. Soc.*, 1991, **113**, 5135-5140.

60 S. Hinokuma, H. Fujii, M. Okamoto, K. Ikeue and M. Machida, *Chem. Mater.*, 2010, **22**, 6183-6190.

61 N. J. Lawrence, J. R. Brewer, L. Wang, T.-S. Wu, J. Wells-Kingsbury, M. M. Ihrig, G. Wang, Y.-L. Soo, W.-N. Mei and C. L. Cheung, *Nano Lett.*, 2011, **11**, 2666-2671.

62 S. Deshpande, S. Patil, S. V. Kuchibhatla and S. Seal, *Appl. Phys. Lett.*, 2005, **87**, 133113.

63 Q. Fu, H. Saltsburg and M. Flytzani-Stephanopoulos, *Science*, 2003, **301**, 935-938.

64 M. Haneda, T. Mizushima and N. Kakuta, *J. Phys. Chem. B*, 1998, **102**, 6579-6587.

65 G. W. Graham, A. E. O'Neill and A. E. Chen, *Appl. Catal., A*, 2003, **252**, 437-445.

66 G. Centi, *J. Mol. Catal. A: Chem.*, 2001, **173**, 287-312.

67 R. Narayanan and M. A. El-Sayed, *J. Am. Chem. Soc.*, 2003, **125**, 8340-8347.

68 K. Zhou, Z. Yang and S. Yang, *Chem. Mater.*, 2007, **19**, 1215-1217.

69 M. Pirocchi, R. Barchewitz, S. Bodeur, J.-M. Esteva, Y. Lepetre, R. Rivoira, R. Philip and G. Rasigni, *Appl. Opt.*, 1986, **25**, 3640-3644.

70 T. M. Hayes and J. B. Boyce, in *Solid State Physics*, eds. F. S. Henry Ehrenreich and T. David, Academic Press, 1983, vol. 37, pp. 173-351.

71 M. Lemonnier, O. Collet, C. Depautex, J.-M. Esteva and D. Raoux, *Nucl. Instrum. Methods*, 1978, **152**, 109-111.

CHAPTER 3

s-d HYBRIDIZATION IN GOLD CLUSTERS SUPPORTED ON CERIA NANORODS

3.1 Introduction

Gold catalysts have attracted immense interest because of their catalytic activities towards chemical reactions of both industrial and environmental importance.[1-5] The most investigated chemical reactions on gold clusters are those involving molecular oxygen (O_2). Haruta *et al.* first demonstrated the remarkable catalytic activity of supported gold clusters towards carbon monoxide (CO) oxidation at low temperatures.[6] Activation (adsorption and dissociation) of the O_2 molecules on the gold surface was found as the key limiting factor in the catalytic processes because the formation of the chemisorbed O_2^- intermediate is thermodynamically unfavourable on flat gold surfaces.[7] Theoretical investigations predict the potential reactivity of gold clusters with O_2 with very small chemisorption energy of O_2 on various sizes of gold clusters.[8, 9] However, theoretical models indicate that gold clusters supported on reducible metal oxide exhibit strong adsorption of O_2 at the gold-metal-oxide interface through enhanced electron transfer from the supported gold to the π^* anti-bonding states of O_2.[10, 11] In addition, Chen and Goodman probed experimentally the influence of the oxide support material on the intrinsic properties at the metal surface and showed that the support acted as the dispersant and promoter of the Au overlayers to enhance the binding to CO and O_2.[12] Much research effort has been focused on studying the effects of quantum confinement,[13, 14] cluster geometry[8, 9, 15-17] and charge transfer[10, 18] to illustrate their enhanced catalytic

activity of metal oxide supported gold systems over CO oxidation, both theoretically and experimentally. Yet the origins of the enhanced catalytic activity of metal oxide supported gold clusters, resulting from the changes in the gold electronic structure, are not fully understood.

Elucidating the electronic structure of supported gold clusters can provide critical clues to the mechanisms for their catalytic activity. In most cases, descriptions of the valence band structures suffice to explain the electronic effect in these catalysed chemical reactions.[19] For the well-known catalytically active noble transition metals, such as platinum and palladium, hybridization of *d* orbitals in these supported metal clusters was theoretically shown to be associated with the catalyst interaction of the lowest unoccupied molecular orbitals (LUMO) of the reactants and with the trends in their increased reactivity.[20] Gold atoms possess an electronic configuration of [Xe] $4f^{14}5d^{10}6s^{1}$ with a filled 5*d* subshell and a half-filled 6*s* subshell. The relativistic effects in gold stabilize its 6*s* orbital and destabilize its 5*d* orbitals.[21-23] Thus, for gold clusters, these effects, together with upward shift of the 5*d* orbitals to the Fermi level due to gold's 4*f* filled subshell, lead to a reduction of the *s*-*d* energy gap and hence render the theoretically expected hybridization of the 5*d* and 6*s* orbitals.[21, 24, 25] When the centre of *d* band spectral weight of the gold clusters is close enough to the Fermi level, these *s*-*d* hybridized orbitals (or bands) essentially increase the number of free *d* states (number of *d* holes) available for bonding with incoming reactant molecules and lowering the transition state energy to promote the reactions.[18] For example, computation modelling predicts that strong adsorption of acetone on gold clusters is based on the overlap of the *s*-*d* hybridized orbitals among the highest occupied molecular orbital (HOMO) with those

at the LUMOs of acetone to form chemical bonds and promote the chemisorption of acetone.[26] Though the importance of the valence-band hybridization in gold-cluster-based catalysts has been long postulated, such a proposed electronic structure feature *has yet to be observed* in active, supported gold cluster catalyst systems.

Our resonance photoemission spectroscopy (RPES) studies, *vide infra*, exhibit resonant enhancements due to 5*p*-to-5*d* and 4*f*-to-5*d* electronic transitions for the gold clusters supported on ceria nanorods (0.01 at.% Au:CeO_{2-x}) and hence the existence of *s*-*d* hybridization in these gold clusters. For this low gold-concentration catalyst system, since the superficial oxygen atoms from the ceria support have strong interactions with the supported gold clusters,[15, 27] the valence states of these oxygen atoms and gold clusters are expected to be slightly mixed. This allows us to study the 5*p*-*to*-*5d* and 4*f*-to-5*d* transitions of the gold clusters indirectly by examining the photoemission of the O 2*p* derived states of metal oxide support as a function of photon energy. In addition, density functional theory (DFT) calculations were performed on two ceria slab-supported gold cluster models to elucidate their detailed 5*d* and 6*s* band structures and provide theoretical evidence to validate the existence of hybridization between these bands in low gold concentration Au:CeO_{2-x} catalysts.

3.2 Experimental Methods

3.2.1 Synthesis of Gold Clusters on Ceria Nanorods

A mixture of 0.5 g of cerium(III) sulfate ($Ce_2(SO_4)_3 \bullet xH_2O$) and 40 mL of 10 M sodium hydroxide (NaOH) was added to a 50-mL capacity Teflon-lined stainless steel autoclave. The mixture was hydrothermally treated at 120 °C for 15 h. in a convection

oven to produce cerium (III) hydroxide ($Ce(OH)_3$) nanorods. The product was filtered with a 3.0-μm pore size polycarbonate filter membrane (Millipore, Billerica, MA) and rinsed with three aliquots of 50 mL of water. The filtered nanorods were then heated in a convection oven for another 2 h. at 50 °C for further oxidation. Subsequently, 25 mL of water, and 17.1 μL of 0.01 M tetrachloroauric acid ($HAuCl_4$) solution were mixed with this mostly oxidized cerium oxide powder. The mixture was stirred for 20 min. to deposit Au ions onto the cerium oxide nanorods. Afterwards, 25 mL of 30 % aqueous H_2O_2 was added to the mixture and sonicated for 30 min., followed by mechanical stirring for an additional 30 min. to attain complete reactions. The resulting products were filtered with a 3.0-μm pore size polycarbonate membrane, rinsed with three aliquots of 50 mL of water and dried for 4 h. at 50 °C in a convection oven. Before evaluations, the synthesized materials were activated at 400 °C in a flow of 100 SCCM (standard cubic centimeter per minute) of simulated air (20 % O_2/ 80 % N_2) for 30 min. in a horizontal 1”-diameter quartz tube annealing furnace with an operating pressure of 0.1 Torr.

3.2.2 Density Functional Theory Modelling of Gold on Cerium Oxide

A DFT calculation was performed to model the Au:CeO_{2-x} system by using VASP code with the projector augmented-wave (PAW) method, plane-wave basis set with cutoff energy of 400 eV, and generalized gradient approximation (GGA) within the parameterization of Perdew-Burke-Ernzerhof (PBE), and the DFT+*U* method. A 9-atomic-layered CeO_2 slab model with eight percent oxygen atoms removed from the surface and subsurface layers was constructed to simulate a defective CeO_2(111) surface containing both surface and subsurface oxygen vacancy defects. Then, a tetrahedral gold cluster (t-Au_{19}) or a planar gold cluster (p-Au_{19}) was placed on the top of the ceria slab

surface. A 19-atom-layered Au (111) slab model was also constructed to compute the bulk gold electronic structure. For all these calculations, structure optimizations were performed until the maximum force was smaller than 0.02 eV/Å.

3.2.3 Composition and Structural Characterization of Catalysts

The elemental composition of the catalysts was analyzed using a Thermo Jarrell Ash IRIS Advantage inductively coupled plasma-optical emission spectrometer (ICP-OES). A catalyst sample of 50 mg was dissolved in 10 mL of freshly made aqua regia (70 % concentrated HCl: 30 % concentrated HNO_3) at 110 °C for 1 h. in an acid digestion autoclave. The resulting solution was then diluted with de-ionized water to a 50 mL total volume solution for the elemental analysis.

The morphology of the catalyst particles was investigated by transmission electron microscopy (TEM). The catalyst powders were dispersed in methanol. 10 μL of the suspension mixture was sonicated for 5 s. and loaded on holey carbon films supported on copper TEM grids. TEM micrographs were collected using a Hitachi H7500 transmission electron microscope (Hitachi High Technologies America, Inc., Pleasanton, CA) operated at 100 kV. High resolution TEM (HRTEM) images of the samples were obtained using a FEI Tecnai G^2 F20 S-Twin TEM and a FEI Tecnai Osiris TEM (FEI Company, Hillsboro, OR). Both TEMs were operated at 200 kV and equipped with high brightness Schottky field emission electron guns. Collected images and selected area electron diffraction patterns were analyzed with the Digital Micrograph^{TM} software and Image J software for evaluating the crystallinity of the catalyst samples. The crystal structures of the samples were also investigated with a Rigaku D/Max-B diffractometer

(Rigaku America, The Woodlands, TX) equipped with a Cu Kα X-ray source of average wavelength 1.544 Å.

The X-ray absorption measurements were performed in the conventional fluorescence mode using a Lytle detector at the beam line BL07A of the Taiwan Light Source at the National Synchrotron Radiation Research Center in Hsinchu, Taiwan. The photon energy dependent, resonance photoemission spectra were obtained using plane-polarized synchrotron light dispersed by a 3-m toroidal grating monochromator at the Center for Advanced Microstructures and Devices of Louisiana State University. These measurements were made at room temperature in an UHV chamber employing a hemispherical electron analyzer with an angular acceptance of ±1°. The combined resolution of the electron energy analyzer and monochromator was 120–150 meV. The photoemission experiments were undertaken as a function of photon energy in the range of 50–120 eV, with a light incidence angle of 45° with respect to the surface normal and with the photoelectrons collected along the surface normal to preserve the highest point group symmetry and eliminate any wave vector component parallel with the surface. All binding energies are referenced to the Fermi level, as determined from clean bulk gold.

3.2.4 Catalytic Activity Characterization

Carbon monoxide (CO) oxidation reactions with the gold decorated ceria (0.01 at.% Au:CeO_{2-x}) catalysts were carried out in a U-tube fixed-bed quartz reactor with a 30 mL/min. flow of feed gas mixture of CO (1.06 %) and O_2 (20.41 %) balanced in helium and controlled by a mass flow controller (MFC, Type 1479A, MKS Instruments, Inc., Orland Park, IL). 100 mg of 0.01 at.% Au:CeO_{2-x} catalyst was used for each of the

catalytic activity reactions. Gas chromatography (GC, Agilent 7820A, Agilent Technologies, Santa Clara, CA) with a packed column (Alltech HayeSep Q 80/100, Grace, Deerfield, IL) was used to monitor the concentrations of carbon dioxide (CO_2) in the effluent. Between each consecutive data point collected at different reaction temperatures, a minimum of 10 min., without reaction gases flowing, were allowed for the system to reach thermal equilibrium before data collection. The catalytic activity of the samples were examined at reaction temperatures from 0 °C to 150 °C with *ca.* 10 °C intervals for 0.01 at.% Au:CeO_{2-x}. For pure ceria nanorods, the reaction temperatures were chosen from 25 °C to 325 °C with *ca.* 25 °C intervals.

3.3 Results

3.3.1 Physical and Chemical Properties of Supported Gold Catalysts

The catalytically active 0.01 at.% Au:CeO_{2-x} nanorods catalysts in this study were prepared by a wet impregnation of gold salt to deposit gold clusters onto ceria nanorods synthesized by a modified hydrothermal method[28]. A subsequent vacuum annealing at a modest 0.1 Torr was applied to achieve more active Au:CeO_{2-x} catalysts caused by the high density of oxygen vacancy defects created in the activation process on the ceria. This was found to be favorable for the binding of the active species on gold clusters.[29, 30] (see Experiment Methods for details) The mean sizes of the olive drab Au:CeO_{2-x} nanorods were 7-12 nm in diameter and 200-500 nm in length. (See Figure 3.1) The 0.01 at.% gold loading in this catalyst was confirmed by inductively couple plasma optical emission spectroscopy analysis with triplicate samples. From X-ray diffraction

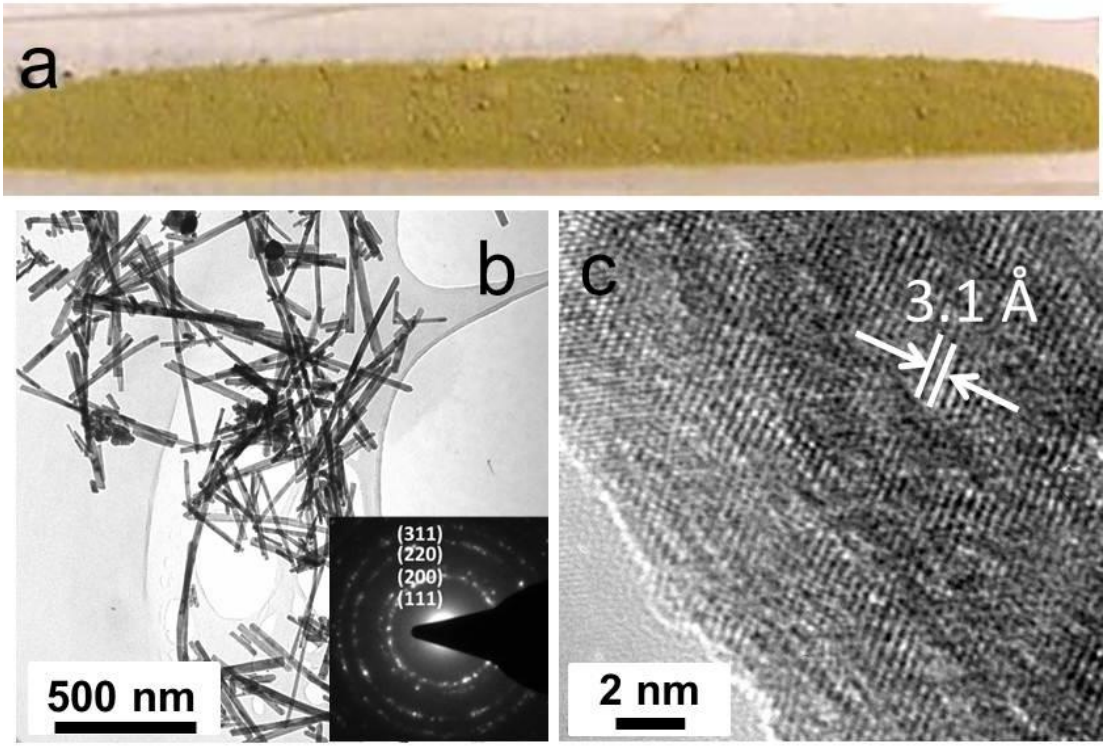

Figure 3.1 a) Photo and b) TEM image of 0.01 at.% Au:CeO_{2-x} nanorods. (Inset) selected area electron diffraction pattern of the nanorods in (b) reflecting the fluorite structure of cerium(IV) oxide. c) HRTEM image of a single nanorod showing lattice fringes with spacing of 3.1 Å corresponding to the (111) plane of cerium(IV) oxide.

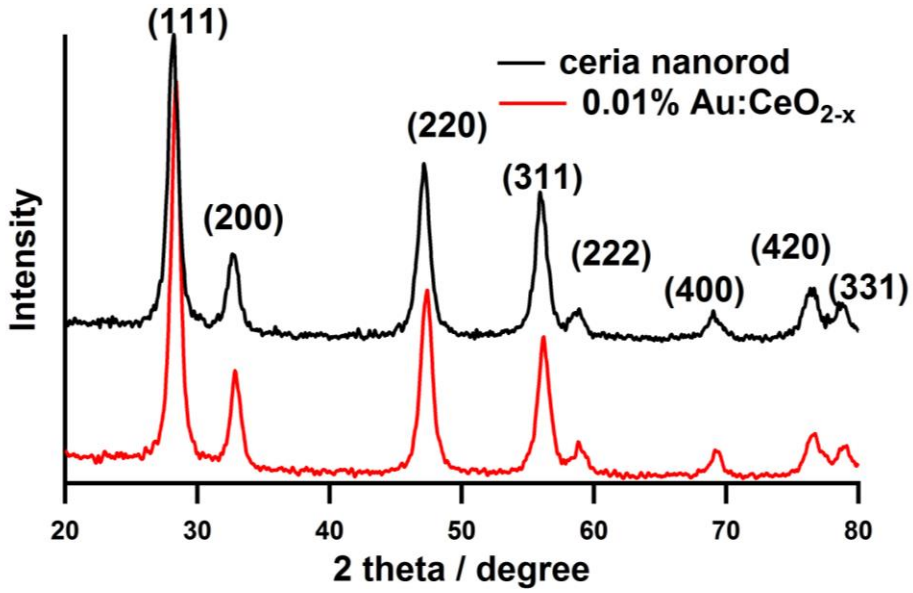

Figure 3.2 X-ray powder diffraction (XRD) patterns of CeO_{2-x} (ceria) nanorods and 0.01 at.% Au:CeO_{2-x} nanorods after low pressure activation at 400 °C in a flow of 100 SCCM of simulated air (20 % O_2/ 80 % N_2) for 30 min. at 0.1 Torr. All peaks are indexed with respect to the cubic $Fm\bar{3}m$ structure of cerium (IV) oxide (CeO_2). ICDD card 04-013-4361 was used for the peak assignments for the CeO_2 content in the patterns. No peaks corresponding to Au, AuO_x, nor $Au(OH)_x$ were observed in the XRD patterns.

(Figure 3.2) and transmission electron microscopy (TEM) images of the catalyst, the CeO_2 ceria nanorods are found to be in the typical fluorite structure. Probably due to the low gold concentration and the low z-contrast between gold and cerium, neither diffraction peaks from the deposited gold nor TEM images of gold clusters were observed in our characterization experiments. Extended X-ray absorption fine structure (EXAFS) analysis of the Ce-L_3 edge absorption spectrum of the sample indicates the presence of high density of oxygen vacancy sites in the ceria nanorods as suggested by the low coordination number (CN = 6.6) of oxygen around the cerium atom when compared to that of the perfect CeO_2 structure (CN = 8). (Table 3.1) It is noteworthy that our low gold concentration Au:CeO_{2-x} sample examined in this study has high catalytic activity towards the oxidation of CO at low temperatures. This Au:CeO_{2-x} catalyst achieved 50 % conversion of CO to CO_2 (light-off temperature, T_{50}) at *ca*. 100 °C. In contrast, the ceria nanorods (CeO_{2-x}) synthesized using a similar procedure exhibited a T_{50} at *ca*. 200 °C. (Figure 3.3)

3.3.2 *d*-Hole Population in Electronic Structures of Supported Gold Clusters

The local structure of gold clusters in the 0.01 at.% Au:CeO_{2-x} nanorods was also studied by X-ray absorption near edge structure (XANES). Figure 3.4 shows the normalized Au L_3-edge XANES data of 0.01 at.% Au:CeO_{2-x} catalyst and Au metal foil (bulk). In general, the absorption spectrum from the gold clusters in the catalyst exhibits similar features as that of the gold metal foil, except that the spectrum for the catalyst has a more intense white line (a feature at the top of the sharply rising part of spectrum at *ca.* 11.92 keV). Since the intensity of the resonance at the threshold (white line) is associated

Table 3.1 EXAFS results charactering the cerium oxide structure in 0.01 at.% Au:CeO_{2-x} catalyst and bulk cerium oxide standard by using Ce L_3-edge data.

Sample	Bond	N	R (Å)	σ (10^{-3} Å^2)	ΔE (eV)
0.01 at.% Au:CeO_{2-x}	Ce-O	6.6 ± 0.1	2.287 ± 0.005	4.4 ± 0.3	2.3 ± 0.3
	Ce-Ce	6.8 ± 0.1	3.803 ± 0.005	0.1 ± 0.3	0.9 ± 0.5
	Ce-O	15.6 ± 1.6	4.482 ± 0.005	4.9 ± 0.4	1.0 ± 0.6
Bulk ceria	Ce-O	8 ± 0.1	2.32 ± 0.005	0.1 ± 0.2	5.8 ± 0.2
	Ce-Ce	12 ± 0.3	3.82 ± 0.005	0.1 ± 0.5	-0.8 ± 0.4
	Ce-O	24 ± 1.2	4.48 ± 0.005	1.5 ± 0.5	1.6 ± 0.4

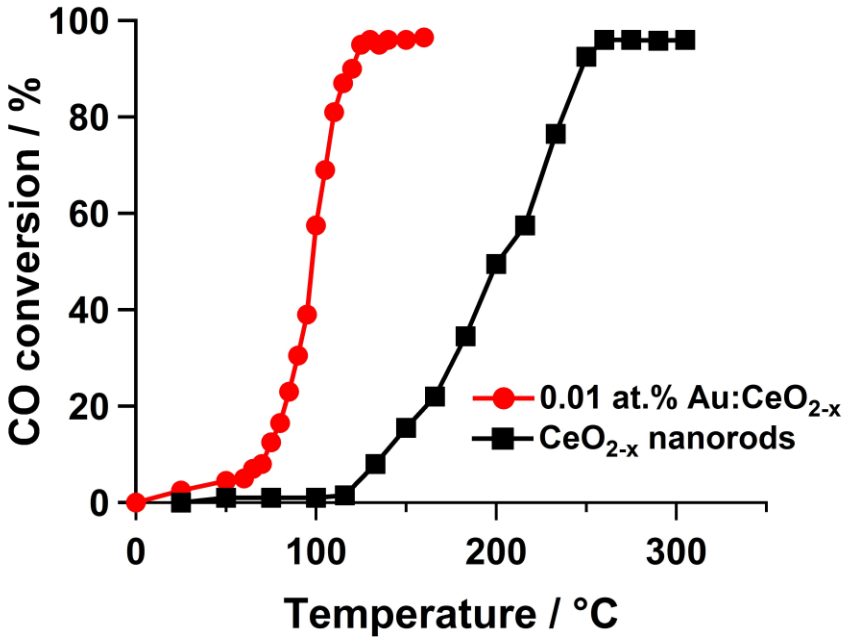

Figure 3.3 Temperature dependent CO catalytic oxidation reaction with (red dot) 0.01 at.% Au:CeO_{2-x} and (black square) pure ceria (CeO_{2-x}) nanorods.

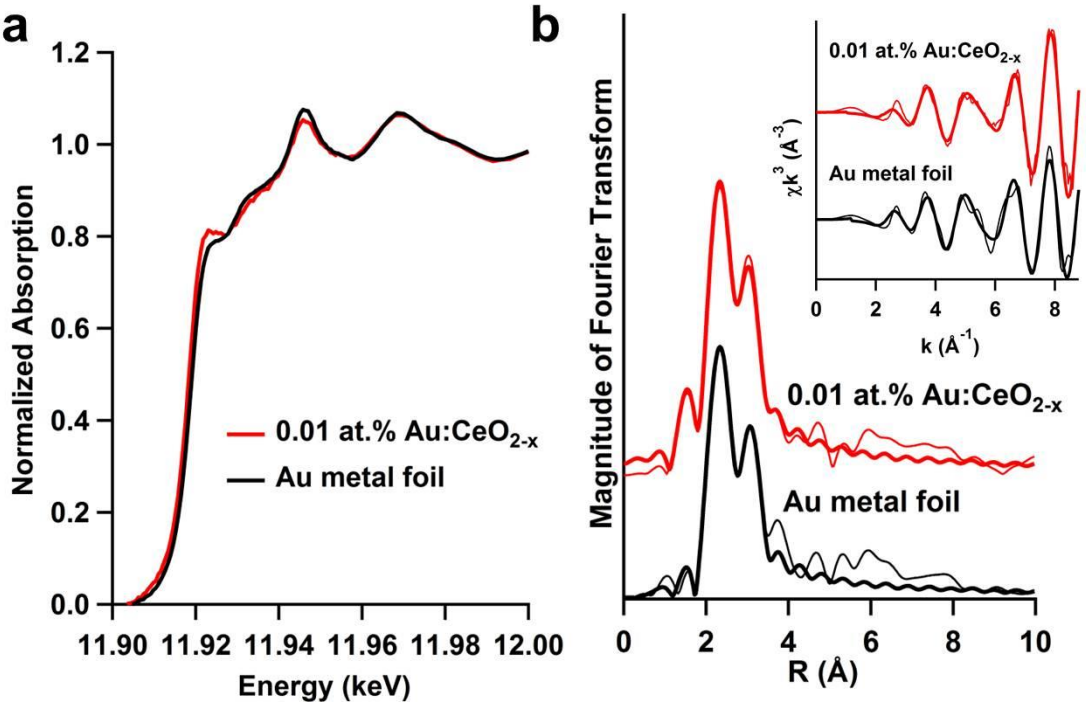

Figure 3.4 (a) Normalized Au L_3-edge XANES spectra of 0.01 at.% Au:CeO_{2-x} nanorods and the reference gold metal foil. (b) Fourier transformed Au L_3-edge EXAFS data in (a). The inset data are the corresponding EXAFS functions in *k* space. (Thick lines: data; thin lines: fittings)

with a $2p_{3/2}$-to-$5d_{5/2,3/2}$ dipole transition that probes the unoccupied densities of *d* states at the Fermi level of gold[31], the more intense white line indicates an increase in the *d*-hole population in the gold clusters on the Au:CeO_{2-x} catalyst.

EXAFS data in Figure 3.4 demonstrates the presence of metal-substrate bonds in the Fourier transformed spectrum for the 0.01 at.% Au:CeO_{2-x}. From the fitted model data, this metal-substrate bond can be attributed to an Au-O bond with an average distance of 2.02 Å. (see Table 3.2), indicating a strong interaction between the supported gold clusters and their ceria supports.[27] A slightly shorter Au-Au atomic distance (2.83 Å) and lower coordination number (8.9) were observed in the 0.01 at.% Au:CeO_{2-x} catalyst than those of bulk gold. (Table 3.2) The shorter Au-Au bond length indicates the small gold cluster size distribution in the catalyst. This small size effect has been proposed to increase the *d* hole population in gold clusters[31]. This prediction is further supported by the more intense white line observed for the catalyst in the Au XANES data. (Figure 3.4 a)

3.3.3 *s*-*d* Hybridization in Gold Clusters on Ceria Nanorods

The electronic structure and valence band spectra (VBS) of the 0.01 at.% Au:CeO_{2-x} were investigated using resonant photoemission spectroscopy (RPES) to determine if resonant enhancement of the valence band occurs for the gold clusters at photon energies corresponding to the gold 5*p* and 4*f* threshold, an indication of both 5*p*-to-5*d* and 4*f*-to-5*d* transitions and thus the existence of 6*s*-5*d* hybridization. The photoelectron spectra were acquired at different photon energies from 65 to 105 eV for the RPES of the O 2*p* states from the ceria support. Owing to the strong interactions

Table 3.2 EXAFS results charactering the gold local structure from 0.01 at.% Au:CeO_{2-x} catalyst and gold metal foil with Au L_3-edge data.

Sample	Bond	N	R (Å)	σ (10^{-3} Å^2)	ΔE (eV)
0.01 at.% Au:CeO_{2-x}	Au-O	0.6 ± 0.3	2.02	4.1 ± 9.9*	-15 ± 5
	Au-Au	8.9 ± 1.3	2.83 ± 0.01	3.8 ± 1.3	4.0 ± 0.8
Au metal foil	Au-Au	12	2.86 ± 0.01	8.1 ± 1.1	5.2 ± 0.6

*Note: The uncertainty is large due to the small Au-O peak when compared to the Au-Au peaks.

theoretically predicted between gold clusters and ceria supports,[15, 29] we focused on investigating the O 2*p* derived states to elucidate the gold resonance in the Au:CeO_{2-x} sample and to overcome the weak signal from the low concentration gold in the catalyst. Figure 3.5 shows the normalized intensity of the VBS recorded at different incident photon energies. Since the binding energies are denoted in terms of $E - E_F$, the binding energies of occupied states are negative. Figure 3.5a is also re-plotted and interpolated using a false color scale in a 2-dimensional manner to demonstrate the intensity change of photoemission corresponding to the photon energy variation in Fig. 3.5b. To evaluate the electronic properties and contributions of different bonding and non-bonding orbitals to the VBS, three Gaussian-shaped peaks were fitted to model the RPES spectra in Fig. 3.5a. Each of these spectra in general consists of a peak appearing at a binding energy of ~ -2 eV (labeled as Peak A) and a broad band stretching from -10 eV to -4 eV (labeled as Peaks B and C), which correspond to the primarily O 2*p* derived states of the ceria support.[32] Peak A is attributed to the emission of electrons from localized Au 5*d* state, whose weak intensity is due to the low loading of gold (0.01 at. %) on the catalyst surface. The enhancement of the valence band states for bulk gold usually affects the states from -6 eV to -3 eV binding energy in resonance photoemission experiments.[33] In our data, this range is observed to be broadened and starts from -8 eV to -2 eV binding energy and accounts for most of the valence band and is a typical feature for gold clusters of small sizes. This broadening of the valence band features, without the addition of specific spectra feature is the result of the increased inhomogeneity of the gold atoms in the clusters and the presence of more localized unoccupied *d* states at the Fermi level.[31, 34] All of these changes in the valence spectral density is consistent with the Au L_3-edge

XANES data that indicates an increase in the *d* hole population in the gold clusters of Au:CeO_{2-x}. In the photoemission spectra (Figure 3.5a), Peaks B and C in the broad band (-10 eV to -4 eV binding energy) arise from the photoemission from the O $2p_x$, O $2p_y$ orbitals (-5.7 eV binding energy) and O $2p_z$ orbital (-7.7 eV binding energy), respectively.[35] The photoemission originating from gold 5*d* band is expected to yield an emission at around the same binding energy region of this broad peak. Although it is difficult to identify photoemission originating from gold 5*d* band, due to the trace amount of gold in our catalyst, the resonant enhancement of the valence band in the photoemission from gold clusters can be clearly observed in the plot of the intensities of Peak B as a function of photon energy at the Au 5*p* and 4*f* thresholds. The maximum intensities in the photoemission spectra occur at roughly Au $5p_{1/2}$ (74.2 eV) and $4f_{5/2}$ (87.6 eV) core threshold binding energies, and are indicative of the $5p_{1/2}$-to-$5d_{3/2}$ and $4f_{5/2}$-to-$5d_{3/2}$ transitions of bulk gold, respectively.[36, 37] Since the electronic configuration of a gold atom ([Xe] $4f^{14}5d^{10}6s^1$) indicates a full 5*d* subshell, these transitions can only occur if there is in fact hybridization of the Au 5*d* and 6*s* in the gold clusters of the catalyst, leading to partial, not complete, occupancy of the valence Au 5*d* bands. Our findings are also consistent with the other reported experimental and computational work that noble metal clusters of small sizes exhibit *s*-*d* hybridization.[26, 38, 39] Additionally, the observed non-zero absorption regions just below the Fermi level in the photoemission spectra support that the gold clusters on the ceria nanorods are mainly of Au^0 state. All these observations indicate that the significant *d*-hole population revealed in the XANES data is likely ascribed to the hybridization of 5*d* states with 6*s* states in the gold clusters.

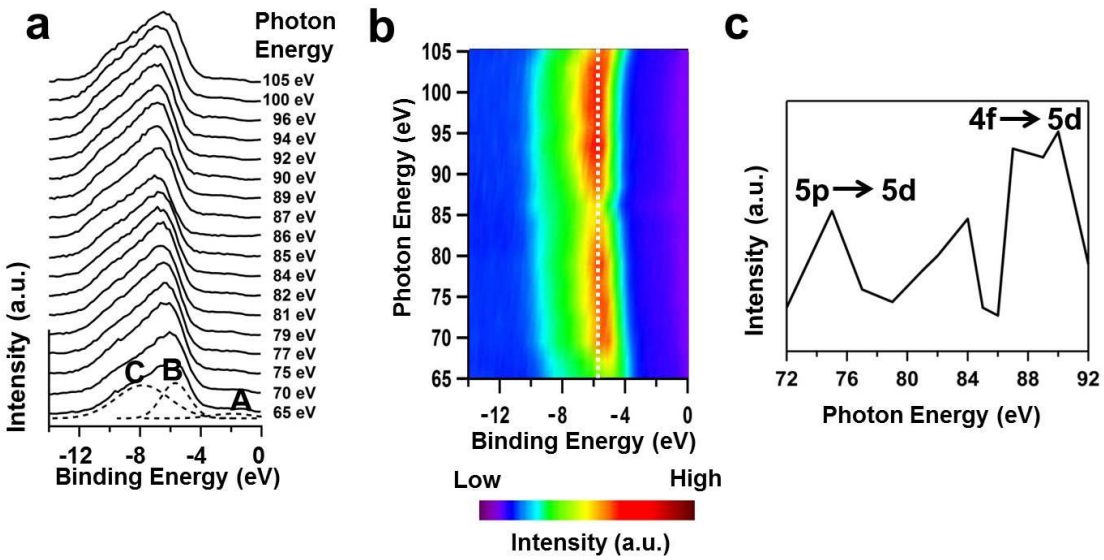

Figure 3.5 a) Fitted valence band resonant photoemission spectra for the 0.01 at.% Au:CeO_{2-x} nanorods taken at photon energies in the range of 65 – 105 eV. Peak A: Au 5*d* band. Peak B: O $2p_x$ and O $2p_y$ derived states and Au 5*d* band envelope. Peak C: O $2p_z$ derived states. b) Interpolated 2-D false color plot using data in (a). White dash line: Binding energy at -5.7 eV. c) Plot of the photoemission intensities at -5.7 eV binding energy as a function of photon energy for the Au in Au:CeO_{2-x} nanorods using the fitting data for Peak B. Binding energies are denoted in terms of E - E_F.

3.3.4 Density Functional Theory Modelling

The existence of *s-d* hybridization in the ceria supported gold clusters is also predicted in our computation studies on models composed of gold clusters on cerium oxide slabs to simulate the Au:CeO_{2-x} catalyst. Density functional theory (DFT) calculation were performed to obtain an optimized slab of C-type $CeO_{1.5}$ bulk with (111) surface using the VASP code.[40] A 9-atom-layered CeO_2 slab model (CeO_{2-x}) with 8% oxygen atoms removed from the surface and subsurface layers was constructed to simulate a defective CeO_2 (111) surface containing both surface and subsurface oxygen vacancy defects. A 19-atom-layered Au (111) slab model with the thickness of about 42 Å was used to simulate the electronic structure of bulk gold. The Au_{19} clusters were used to simulate gold structures on the ceria support based on the cluster size evaluation from the EXAFS data. Two different structures of gold clusters composed of 19 gold atoms, tetrahedral Au_{19} (t-Au_{19})[41] and planar Au_{19} (p-Au_{19}), were considered to represent two extreme cases in the construction of models of a gold cluster on the ceria slab (Au_{19}:CeO_{2-x}). The tetrahedral shaped gold cluster was considered because a similar isolated Au_{19} cluster structure was predicted as the most stable Au_{19} cluster structure in previous computational studies.[41-43] The planar gold cluster structure was used because a tendency to planarity of gold clusters is strongly favored by the relativistic effect, which may decrease the *s-d* promotion energy and lead to the hybridization of the half-filled 6*s* orbital with the fully occupied $5d_{z^2}$ orbital.[14, 43] The optimized structure of the t-Au_{19}:CeO_{2-x} model is shown in Figure 3.6a. The t-Au_{19} cluster was found to be slightly negatively charged (0.17 electron charge per gold atom) as shown in the charge density calculation in Figure 3.6b. The excess charge in the t-Au_{19} cluster likely transferred from

the electron density of the oxygen vacancies in the defective ceria slab support.[15] Comparisons between the total density of states (TDOS) of the t-Au_{19}, CeO_{2-x} slab and t-Au_{19}:CeO_{2-x} in Figure 3.6c suggest that the interaction of t-Au_{19} with the ceria support possibly introduces the pin-in gap state feature (or metal-induced gap states (MIGS)) present below the empty Ce 4*f* states and the Fermi level. By analysing the partial density of states (PDOS) of t-Au_{19}:CeO_{2-x} (Figure 3.6d), we find that these MIGS are mainly composed of Au 5*d* and 6*s* states, consistent with the photoemission findings discussed in the previous section. Non-zero but small contributions from the Au 6*p* states are also noticed in these MIGS. The similarities among the shapes of these 5*d* and 6*s* band structures in the MIGS region further confirm the presence of a strong *s*-*d* hybridization in this supported t-Au_{19} cluster system. The overlap and similarity around the Fermi level of O 2*p* band with Au 6*s* and 5*d* bands displays the significant interaction between the gold clusters and ceria support. Interestingly, in comparison to the band structure of the Au (111) slab, a larger magnitude of spectral weight for the *d* band occurs at the Fermi level for the Au_{19} cluster, revealing more localized HOMO states near the Fermi level of the supported cluster. (Figure 3.6c) A larger *d*-hole population is also evident in the PDOS of t-Au_{19}:CeO_{2-x} when compared with the one for the Au (111) slab model in Figure 3.6d. This again is consistent with our XANES data. Similar *s*-*d* hybridization and *d*-hole population features were also observed in the band structure of the p-Au_{19}:CeO_{2-x} model. (See Figure 3.7)

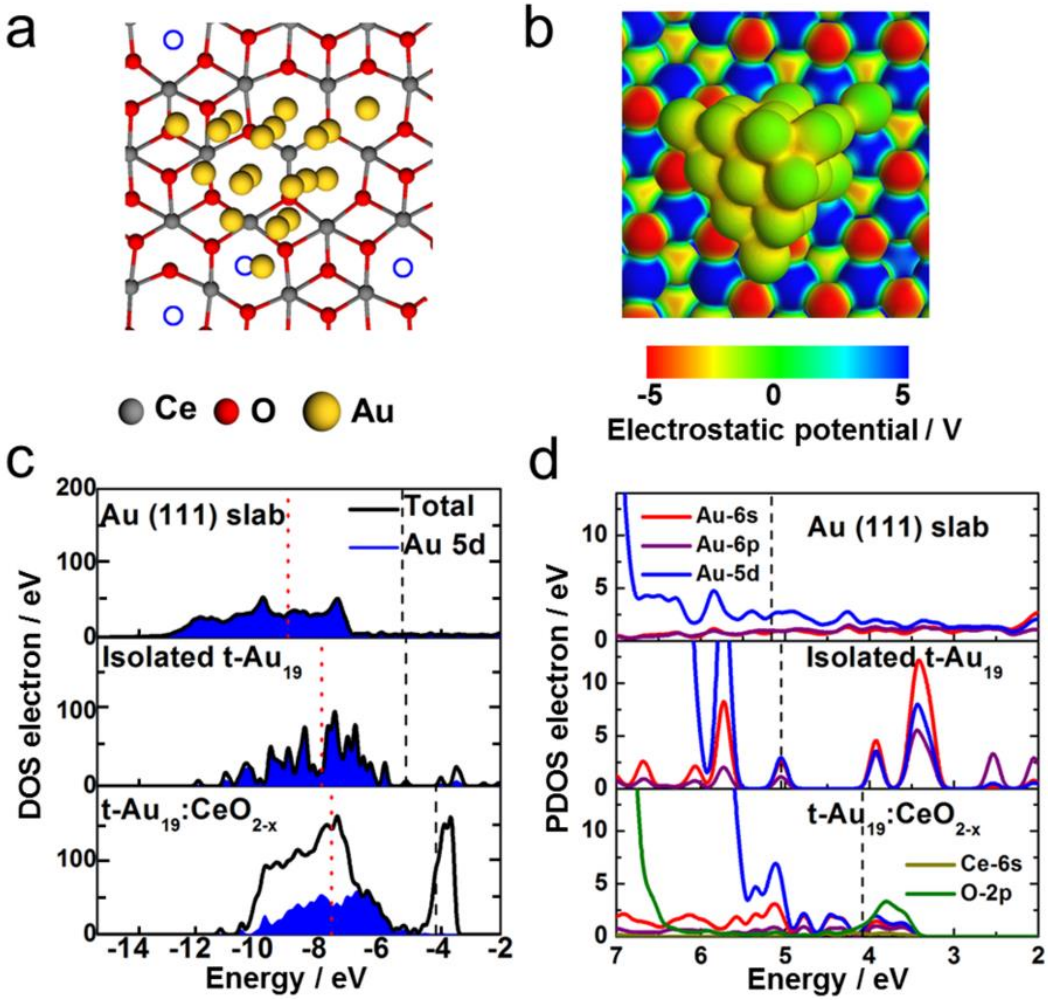

Figure 3.6 a) Top view of a DFT-optimized structures of a t-Au_{19} cluster adsorbed on a defective 9-atom-thick CeO_2 (111) surface slab (CeO_{2-x}). (blue circles) oxygen vacancy sites. b) Calculated charge distribution of the t-Au_{19}:CeO_{2-x} model in (a). c) (Black) Total surface density of states (TDOS) and (blue) density of states of Au 5*d* band for (top) Au (111) slab, (middle) isolated t-Au_{19} and (bottom) t-Au_{19}:CeO_{2-x}. d) Partial density of states (PDOS) for the 6*s*, 6*p* and 5*d* orbitals of Au in (top) a 19-atom-thick Au (111) slab, (middle) isolated t-Au_{19} and (bottom) t-Au_{19}:CeO_{2-x}. The 6*s* orbital of Ce and 2*p* orbital of O in t-Au_{19}:CeO_{2-x} are also illustrated in the bottom figure. Red dash lines: Au 5*d* band centres. Black dash lines: Fermi levels with respect to vacuum at E = 0 eV.

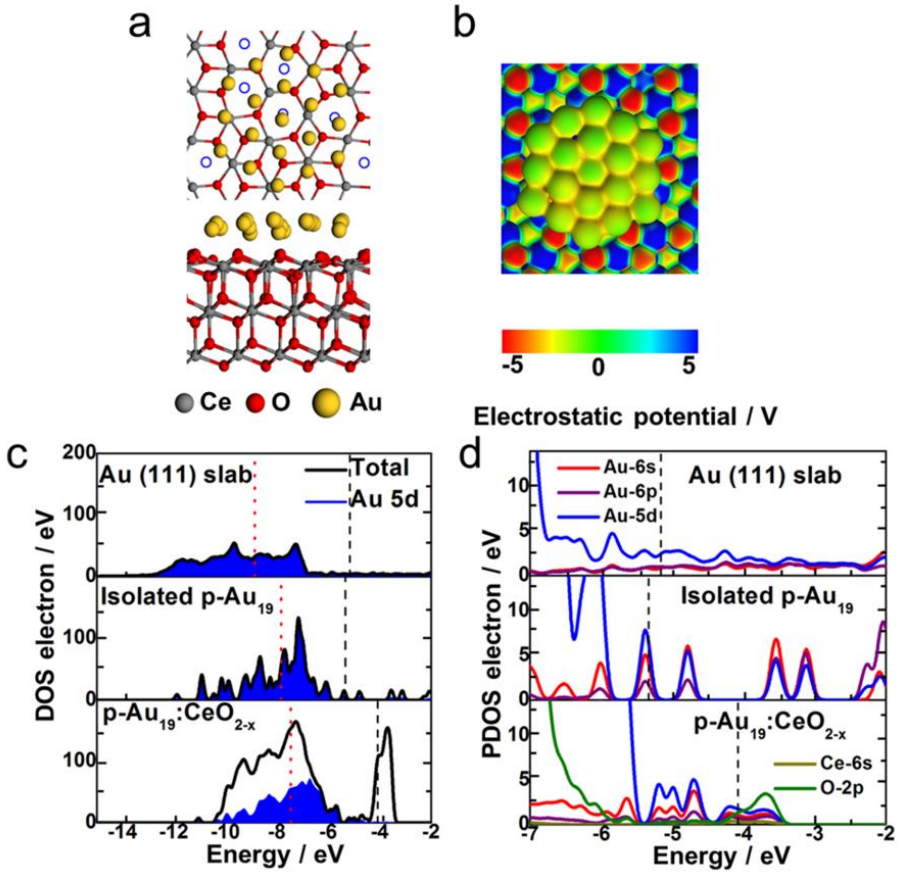

Figure 3.7 a) Top and side view of an optimized structure of a p-Au_{19} cluster adsorbed on the CeO_2(111) surface of a defective 9-atom thick ceria slab (CeO_{2-x}). (blue circles) oxygen vacancy sites. b) Calculated charge distribution of the p-Au_{19}:CeO_{2-x} model in (a). c) (Black) Total surface density of states (TDOS) and (blue) density of states of Au 5*d* band for (top) a 19-atom-thick Au (111) slab, (middle) isolated p-Au_{19} and (bottom) p-Au_{19}:CeO_{2-x}. d) Surface partial density of states (PDOS) for the 6*s*, 6*p* and 5*d* orbitals of Au in (top) 19-atom-thick Au (111) slab, (middle) isolated p-Au_{19} and (bottom) p-Au_{19}:CeO_{2-x}. The 6*s* orbital of Ce and 2*p* orbital of O in p-Au_{19}:CeO_{2-x} are also demonstrated in the bottom figure. Red dash lines: Au 5*d* band centers. Black dash lines: Fermi levels with respect to vacuum at E = 0 eV.

3.4 Discussion

The location of the *d*-band centre with respect to the Fermi level of a transition metal-based catalyst has been proposed to strongly influence catalytic activity. According to the Hammer-Norskov model, molecular adsorption energy on the surface of a transition metal was found as a strong function of the *d*-band centre location.[19] As the *d* band centre up-shifts towards the Fermi level, based on the frontier orbital theory, formation of chemical bonds between the transition metal-based catalyst and reactants are predicted because of the increase in the availability of symmetry-allowed and energetically favoured electronic states from the *d* band. For example, for reactions involving O_2 molecules, if the energy of the symmetry-allowed HOMO of a gold cluster is much closer to that of π^* orbitals of O_2 molecules, it will increase the probability of electron transfer from the *d* band of gold to the O_2 molecules to form chemical bonds and therefore assist the catalytic reactivity of the cluster.[19] Similar *d*-band up-shifts are observed in the electronic structure of our Au_{19}:CeO_{2-x} models, as seen in Figure 3.6c. This offers possible hypotheses to explain the observed high catalytic behaviour of our Au:CeO_{2-x} catalyst over CO oxidation at low temperatures. The placement of the Fermi level energy of our model systems have large differences with deviations up to about 1.4 eV because of the strong interaction involving charge transfer between the ceria support and supported gold clusters. We find that the corresponding Au 5*d* band centre locations with respect to vacuum level for the isolated t-Au_{19} and t-Au_{19}:CeO_{2-x} are at energies of -7.76 and -7.45 eV, respectively. These up-shifted values are in contrast to the energy of -8.85 eV for the Au 5*d* band centre location for the Au (111) slab. Similar up-shift of the *d*-band centre locations are observed for isolated p-Au_{19} (-7.83 eV) and p-Au_{19}:CeO_{2-x} (-

7.46 eV). (See Table 3.3) The t-Au_{19} clusters exhibit stronger *s*- *d* hybridization and upshift of *d* band centre than Au (111) slab. (Figure 3.6c and 3.6d)

The total energy calculation of the optimized models suggests that Au_{19} clusters tend to form a flat layer structure on the surface of a CeO_{2-x} slab model. For isolated clusters, our calculation confirms that a Au_{19} cluster tends to adopt a tetrahedral shape in contrast to the planar structure because the calculated total energy of t-Au_{19} is 0.89 eV smaller than that of p-Au_{19}. However, for ceria supported Au clusters, the total energy of t-Au_{19}:CeO_{2-x} is 0.74 eV larger than that of p-Au_{19}:CeO_{2-x}. From these data, the binding energy of p-Au_{19} onto the CeO_{2-x} slab is -8.84 eV, which is 1.72 eV less than that of t-Au_{19} binding to CeO_{2-x} surface (-7.12 eV). The more stable planar Au_{19} structure on the CeO_{2-x} support indicates higher dispersion or "wetting" of gold on ceria which might be ascribed to the strong interaction between gold atoms and the CeO_{2-x} support.

Our computation results for the Au_{19}:CeO_{2-x} model suggest a non-zero transfer of electrons from the defective ceria to the Au_{19}. Such a negative charge transfer has been predicted to increase the availability of valence electron density of gold for bonding to chemisorbed molecules and affect the strength of highly directional *s*- *d* hybridized orbitals.[15, 18] In the case of oxygen, negatively charged gold clusters can provide more electrons to transfer to π^* orbitals of O_2 molecules, which again affects the adsorption energy of O_2 that is highly sensitive to the electronic state of adsorption site, therefore leading to higher catalytic activity over CO oxidation. Since our computation data suggests the *d* band centre up-shift in small gold clusters when compared with bulk, the larger *d*-hole population in Au 5*d* band of our catalyst and the resulting hybridized *s*-*d* orbitals likely promotes the electron transfer to form bonding and back-bonding between

Table 3.3 Au 5*d* band center locations of bulk gold, isolated t-Au_{19}, t-Au_{19}:CeO_{2-x}, isolated p-Au_{19} and p-Au_{19}:CeO_{2-x} in reference to the vacuum level ($\boldsymbol{E_{vac}}$) and Fermi level ($\boldsymbol{E_F}$), respectively. [a] The Au 5*d* band spectral weight centers were determined by calculating the average energy ($\int \rho E dE \Big/ \int \rho dE$) of the Au 5*d* band for each model. ρ is the Au 5*d* PDOS. A 19-atom-layered Au (111) slab was used as a model to calculate the electronic structure to represent that of bulk gold.

Sample	Au 5*d* band center location (eV)[a]		Fermi level reference to vacuum level (eV)
	Reference to vacuum level, E_{vac}	Reference to Fermi level, E_F	
Au (111) slab	-8.85	-3.69	-5.16
CeO_{2-x}	-	-	-3.94
isolated t-Au_{19}	-7.76	-2.71	-5.05
t-Au_{19}:CeO_{2-x}	-7.45	-3.36	-4.09
isolated p-Au_{19}	-7.83	-2.50	-5.33
p-Au_{19}:CeO_{2-x}	-7.46	-3.38	-4.08

the supported Au clusters and O_2 molecules. Such modifications of the metal surface *d* orbitals due to the valence band hybridization can alter the interactions of the molecules' HOMO and LUMO orbitals with modified metal states and hence lead to considerable consequences for molecular adsorption on catalyst surfaces. Nevertheless, other factors such as the metal-oxide interfacial charge transfer to the supported metal should also be considered because they may also result in shifts of the total *d*-band centre which are not directly related to the binding of the molecule to the metal surface.

3.5 Conclusion

In summary, the existence of *s-d* hybridization in gold of a catalytically active 0.01 at.% Au:CeO_{2-x} catalyst was demonstrated using resonance photoemission spectroscopy and computation modeling. Significant $5p_{1/2}$-to-$5d_{3/2}$ and $4f_{5/2}$-to-$5d_{3/2}$ resonant electronic transitions observed in our Au:CeO_{2-x} catalysts indicate the presence of an unfilled 5*d* subshell (or 5*d* holes) in our gold catalysts and thus provide the evidence for the *s-d* hybridization. The similarities in the shapes and intensity of the 5*d* and 6*s* band in our computed Au_{19}:CeO_{2-x} models verify the presence of strong hybridization of the Au 5*d* and 6*s* states in the supported gold clusters. Small contributions from Au 6*p* band in the MIGS are also observed in our modeling results. Though there is no experimental proof from our data of Au *s-p-d* hybridization, the possibility is not excluded either. Furthermore, the *d*-band center up-shifts determined in the computed PDOS data in these models possibly facilitate the chemisorption of oxygen on low gold concentration Au:CeO_{2-x} catalysts. Our approach to investigate the electronic structures of supported gold catalysts of low gold concentration illustrates an alternate pathway to investigate other metal oxides supported metal systems and to disclose the

electronic structures of the metal clusters for further insights into their structure-reactivity relationship and developing new strategies in catalyst design.

3.6 References

1 S. Carrettin, P. Concepción, A. Corma, J. M. López Nieto and V. F. Puntes, *Angew. Chem. Int. Ed*, 2004, **43**, 2538-2540.

2 M. Chen and D. W. Goodman, *Acc. Chem. Res.*, 2006, **39**, 739-746.

3 W. Deng and M. Flytzani-Stephanopoulos, *Angew. Chem. Int. Ed*, 2006, **45**, 2285-2289.

4 H. Daly, A. Goguet, C. Hardacre, F. C. Meunier, R. Pilasombat and D. Thompsett, *J. Catal.*, 2010, **273**, 257-265.

5 T. Hayashi, K. Tanaka and M. Haruta, *J. Catal.*, 1998, **178**, 566-575.

6 M. Haruta, N. Yamada, T. Kobayashi and S. Iijima, *J. Catal.*, 1989, **115**, 301-309.

7 J. T. Miller, A. J. Kropf, Y. Zha, J. R. Regalbuto, L. Delannoy, C. Louis, E. Bus and J. A. van Bokhoven, *J. Catal.*, 2006, **240**, 222-234.

8 G. Mills, M. S. Gordon and H. Metiu, *J. Chem. Phys.*, 2003, **118**, 4198-4205.

9 Y. Gao, N. Shao, Y. Pei, Z. Chen and X. C. Zeng, *ACS Nano*, 2011, **5**, 7818-7829.

10 Z.-P. Liu, X.-Q. Gong, J. Kohanoff, C. Sanchez and P. Hu, *Phys. Rev. Lett.*, 2003, **91**, 266102.

11 L. M. Molina and B. Hammer, *Appl. Catal., A*, 2005, **291**, 21-31.

12 M. S. Chen and D. W. Goodman, *Science*, 2004, **306**, 252-255.

13 C. Lemire, R. Meyer, S. Shaikhutdinov and H.-J. Freund, *Angew. Chem. Int. Ed*, 2004, **43**, 118-121.

14 M. Valden, X. Lai and D. W. Goodman, *Science*, 1998, **281**, 1647-1650.

15 H. Y. Kim, H. M. Lee and G. Henkelman, *J. Am. Chem. Soc.*, 2011, **134**, 1560-1570.

16 G. Shafai, S. Hong, M. Bertino and T. S. Rahman, *J. Phys. Chem. C*, 2009, **113**, 12072-12078.

17 H. Häkkinen and U. Landman, *Phys. Rev. B: Condens. Matter*, 2000, **62**, R2287-R2290.

18 V. Cooper, A. Kolpak, Y. Yourdshahyan and A. Rappe, in *Nanotechnology in Catalysis*, eds. B. Zhou, S. Han, R. Raja and G. Somorjai, Springer New York, 2007, pp. 13-21.

19 B. Hammer and J. K. Nørskov, in *Advances in Catalysis*, ed. H. K. Bruce C. Gates, Academic Press, 2000, vol. 45, pp. 71-129.

20 B. Hammer and J. K. Nørskov, *Surf. Sci.*, 1995, **343**, 211-220.

21 L.-S. Wang, *Phys. Chem. Chem. Phys.*, 2010, **12**, 8694-8705.

22 P. Pyykko, *Chem. Rev.*, 1988, **88**, 563-594.

23 P. Pyykkö, *Angew. Chem. Int. Ed*, 2004, **43**, 4412-4456.

24 W. Liu, Y. F. Zhu and Q. Jiang, *J. Phys. Chem. C*, 2010, **114**, 21094-21099.

25 L. F. Mattheiss and R. E. Dietz, *Phys. Rev. B: Condens. Matter*, 1980, **22**, 1663-1676.

26 G. S. Shafai, S. Shetty, S. Krishnamurty, V. Shah and D. G. Kanhere, *J. Chem. Phys.*, 2007, **126**, 014704.

27 M. Cargnello, C. Gentilini, T. Montini, E. Fonda, S. Mehraeen, M. Chi, M. Herrera-Collado, N. D. Browning, S. Polizzi, L. Pasquato and P. Fornasiero, *Chem. Mater.*, 2010, **22**, 4335-4345.

28 N. J. Lawrence, J. R. Brewer, L. Wang, T.-S. Wu, J. Wells-Kingsbury, M. M. Ihrig, G. Wang, Y.-L. Soo, W.-N. Mei and C. L. Cheung, *Nano Lett.*, 2011, **11**, 2666-2671.

29 Q. Fu, H. Saltsburg and M. Flytzani-Stephanopoulos, *Science*, 2003, **301**, 935-938.

30 A. Trovarelli, ed., *Catalysis by ceria and related materials*, Imperial college press, 2002.

31 P. Zhang and T. K. Sham, *Phys. Rev. Lett.*, 2003, **90**, 245502.

32 M. Skoda, M. Cabala, I. Matolinova, K. C. Prince, T. Skala, F. Sutara, K. Veltruska and V. Matolin, *J. Chem. Phys.*, 2009, **130**, 034703.

33 R. Courths, H. G. Zimmer, A. Goldmann and H. Saalfeld, *Phys. Rev. B: Condens. Matter*, 1986, **34**, 3577-3585.

34 S. Doniach and M. Sunjic, *J. Phys. C: Solid State Phys.*, 1970, **3**, 285.

35 Q.-H. Wu, A. Thissen, W. Jaegermann, M. Schüz and P. C. Schmidt, *Chem. Phys. Lett.*, 2006, **430**, 309-313.

36 J. A. Bearden and A. F. Burr, *Rev. Mod. Phys.*, 1967, **39**, 125-142.

37 J. C. Fuggle and N. Mårtensson, *Core Level Binding Energies in Metals*, Inst. of Physics, Univ., 1980.

38 Y. B. Losovyj, S.-C. Li, N. Lozova, K. Katsiev, D. Stellwagen, U. Diebold, L. Kong and C. S. S. R. Kumar, *J. Phys. Chem. C*, 2012, **116**, 5857-5861.

39 D. Marchenko, A. Varykhalov, M. R. Scholz, G. Bihlmayer, E. I. Rashba, A. Rybkin, A. M. Shikin and O. Rader, *Nat. Commun.*, 2012, **3**, 1232.

40 G. Kresse and J. Hafner, *Phys. Rev. B: Condens. Matter*, 1994, **49**, 14251-14269.

41 S. Bulusu, X. Li, L.-S. Wang and X. C. Zeng, *Proc. Natl. Acad. Sci. U.S.A.*, 2006, **103**, 8326-8330.

42 S. Bulusu and X. C. Zeng, *J. Chem. Phys.*, 2006, **125**, 154303.

43 E. M. Fernández, J. M. Soler, I. L. Garzón and L. C. Balbás, *Phys. Rev. B: Condens. Matter*, 2004, **70**, 165403.

CHAPTER 4

INFLUENCE OF SUPPORT MORPHOLOGY ON PLATINUM NANOPARTICLES FOR METHANOL ELECTROOXIDATION

4.1 Introduction

Development of an economically viable catalyst is essential to chemical-conversion-based energy production using portable fuel cells for large-scale applications such as aeronautical and space explorations.[1] A cost-effective fuel source reduces the dependence on conventional fuels required for the perpetuation of air or space transportation.[2, 3] Methanol is considered as an excellent energy source for fuel cells because of its relatively high energy density (6.09 $kWh \cdot kg^{-1}$), ease of storage and delivery as well as its low cost synthesis from abundant natural gas resources.[4, 5] Previous studies of methanol oxidation have been performed using anode catalysts such as carbon-supported platinum (Pt) modified with ceria,[6] platinum,[6] platinum-nickel oxide on carbon,[7, 8] and Pt modified with rubidium.[9] Pt-based catalysts, often designed with supported nanosized Pt particles for increased effectively catalytic surface areas, are one category of the most studied electrocatalysts for direct methanol fuel cells due to their high catalytic activity.[10-13]

The use of platinum in acidic electrooxidation conditions for direct alcohol fuel cells has been widely investigated using cyclic voltammetry due to its efficient oxidation of methanol.[6] However, most current research in electrooxidation of methanol has moved away from using acid media to alkaline media due to several reasons. First, some metal oxides used for supporting the platinum, such as ceria, are thermodynamically more stable in alkaline conditions.[14] They are often unstable in acidic media and tend to

dissolve into metal ions.[15] Second, alkaline media can provide more sustainable conditions in industrial applications with increased power density.[16] In addition, the potential peak area overlap for the oxidation of methanol and reduction of Pt peaks further enables the possibility of using one potential to generate a larger current than the case under acidic condition.[17] Nevertheless, the performance stability of commonly used Pt-based fuel cell catalysts are still limited in both alkaline and acid media due to the poisoning of platinum by side-products (e.g. carbon monoxide, carbonaceous species) formed during the methanol oxidation process.[17] Various oxide promoters with high oxidizing power such as ceria[6] and nickel oxide[7] have been applied as supports for Pt NPs in order to remove catalyst poisons by oxidation and/or promote the formation of Pt^0 state on the surface of these NPs.

Ceria is a common catalyst support for Pt-based direct alcohol fuel cells because of its ability to oxidize the catalyst-poisoning carbon monoxide produced in alcohol oxidation reactions.[18-20] Nanostructured ceria of various shapes (NPs, NRs, nanotubes and mesoporous structures) have been shown to enhance the catalytic activities of metal NPs towards carbon monoxide oxidation, the water gas shift reaction and reforming reactions at low temperatures.[21-23] The differences in their activities have been attributed to the ceria crystal plane facets,[24] density of oxygen vacancy sites[21] and crystallinity[25] of the ceria component. However, little is known about the size and plane-facet effect of ceria support in affecting these supported Pt NPs structure and their resulting catalytic activity in methanol electrooxidation. Therefore, morphological and chemical studies of nanostructured ceria and Pt NPs are necessary to elucidate the relationship between the catalytic activity and the ceria support.

Herein, we report our study of nanostructured ceria supports on the influence of the electrocatalytic activity of Pt NPs towards methanol oxidation in alkaline media. Nanostructured ceria in the form of NRs and NPs with comparable diameters and surface areas were used as supports for Pt NPs with a 20 wt.% Pt loading. Transmission electron microscopy (TEM) and X-ray photoelectron spectroscopy (XPS) were applied to elucidate the size, shape and chemical state of the deposited Pt NPs on these ceria supports. Cyclic voltammetry (CV) and chronoamperometry (CA) were applied in the half-cell studies of anodes coated with these two catalysts for investigating their effectiveness in methanol oxidation.

4.2 Experimental method

4.2.1 Sources of Chemical Reagents

Ceria (CeO_{2-x}, $0 \leq x < 0.5$) NPs were purchased from Nanoscale Inc. (Manhattan, KS). Cerium (III) sulfate hydrate ($Ce_2(SO_4)_3 \cdot xH_2O$), platinum acetylacetonate ($Pt(C_5H_7O_2)_2$) and sodium hydroxide (NaOH) were purchased from Sigma-Aldrich (St. Louis, MO). Hydrogen peroxide 30% (H_2O_2) was purchased from VWR SP (Batavia, IL). Fumion® was obtained from FuMA-Tech GmbH (St. Ingbert, Germany). All chemicals were used without further purification unless otherwise noted. A Millipore Synergy system was used to produce the deionized (DI) water of 18 MΩ·cm resistivity.

4.2.2 Catalyst Preparation

Two types of nanostructured ceria (CeO_{2-x}, $0 \leq x < 0.5$), ceria NPs and NRs, supported Pt NPs (loading: 20 wt.% Pt) catalysts were studied. Ceria NPs of *ca.* 2 to 6 nm were purchased from a commercial vendor. Ceria NRs with dimensions of about 5 to 10

nm in diameter and 15 to 50 nm in length were synthesized using our previously published procedure.[21] In the ceria NRs synthesis process, 0.5 g of $Ce_2(SO_4)_3 \bullet xH_2O$ and 40 mL of 10 M NaOH were mixed and added to a 50-mL capacity Teflon-lined stainless steel autoclave. The chemicals in the autoclave were hydrothermally treated for 15 h. at 120 °C in a convection oven to generate cerium (III) hydroxide ($Ce(OH)_3$) nanorods. The product was filtered with a 3.0-μm pore size polycarbonate filter membrane (Millipore, Billerica, MA), rinsed with three aliquots of 50 mL water and placed in the convection oven for an initial oxidation at 50 °C for 2 h. During this oxidation process, most $Ce(OH)_3$ was converted to cerium oxide composed of both Ce_2O_3 and CeO_{2-x}. Then, 25 mL of 30% aqueous H_2O_2 was added to the mixture and sonicated for 30 min., followed by stirring for 30 min. to allow the reaction to reach completion. After stirring, the resulting catalyst was filtered with a 3.0-μm pore size polycarbonate membrane, rinsed with 50 mL of water and dried for 4 h. at 50 °C in a convection oven. Afterwards, the synthesized material was activated at 400 °C in simulated air (20% O_2, 80% N_2) at 100 standard cubic centimeters per minute for 30 min. in a horizontal quartz tube annealing furnace with an operating pressure of 2.0 Torr for activation.

The deposition of 20 wt.% Pt NPs on ceria support was achieved by sonicating a mixture of 30 mg ceria (NRs or NPs) with 9 mL of ethanol and 6 mL of glacial acetic acid for 30 min., followed by an addition of 15.12 mg of platinum acetylacetonate and subsequent sonicating for 30min, and then heated with stirring at 100 °C until dry.[26] The product was finally activated at 400 °C in nitrogen at 1.0 Torr for 30 min.

4.2.3 Physical Characterization of Catalysts

The crystal structures of catalysts were determined using powder X-ray diffraction (XRD) (Bruker Discover D8) with a Cu K_α source of average wavelength 1.544 Å. TEM images of the catalysts were recorded using a JEOL JEM-2200FS operated at 200 kV. The TEM images were recorded either in bright field TEM mode or in scanning TEM (STEM) mode using the high-angle annular dark-field (HAADF) detector. The chemical composition of the catalyst and the oxidation states of elements in the catalyst were determined using XPS performed in a PHI 5600ci spectrometer with a hemispherical electron analyzer. A monochromatic Al Kα X-ray source operated at 15 kV and 350 W was used. All the recorded binding energies were calibrated using the carbon 1s peak at 284.15 eV. Pt 4f XPS data fitting analysis was performed with the software XPSPEAK. Elemental analysis of the bulk samples were performed using a Thermo Jarrell Ash IRIS Advantage inductively coupled plasma optical emission spectroscopy (ICP-OES). Typically, 25 mg of catalyst was dissolved in 10 mL of freshly made aqua regia (70% concentrated HCl: 30% concentrated HNO_3) at 110 °C for 1 h. in an acid digestion autoclave. The obtained solution was further diluted with water to a 25 mL total volume solution for the elemental analysis. The surface areas of nanostructured ceria were measured by the Brunauer–Emmett–Teller (BET) method (ASAP 2010).

4.2.4 Electrochemical Property Characterization

Pt/ceria catalyst coated glassy carbon (GC) electrodes were prepared for methanol oxidation evaluations. Typically, 8 µL of a catalyst “ink” paste consisting of 1 mg of a Pt/ceria catalyst suspended in a 100 µL Fumion® (5% w/w polyarylene sulfonic acid

polyelectrolyte dissolved in water/isopropanol) was deposited onto a GC electrode and allowed to dry for 1 h.

The electrochemical characterization of the Pt/ CeO_{2-x} modified electrodes material was performed under ambient conditions using cyclic voltammetry and chronoamperometry in alkaline media using a potentiostat system (Model Number 1240B, CH Instruments, Inc. Austin, TX). Catalyst coated glassy carbon working electrode, Ag/AgCl reference electrode and a platinum counter electrode were arranged in a typical three-electrode half-cell configuration. All electrolyte solutions were bubbled with argon gas for 10 min. before the experiments were carried out. The surface areas of platinum on the anodes were calculated using the hydrogen adsorption/desorption potential region from the cyclic voltammograms in alkaline medium (0.50 M KOH solution). Cyclic voltammetry was performed at a scan rate of 100 mV/s between -0.500 V and 0.250 V vs. Ag/AgCl in 1.0 M methanol/ 0.50 M KOH aqueous solution at room temperature. The onset potential for each catalyst was determined at 5% of the maximum anodic peak current density for the methanol oxidation reaction at a scan rate of 1 mV/s. Chronoamperometry experiments for Pt/ceria NRs and NPs were carried out with an applied potential of -0.350 V vs. Ag/AgCl in 1.0 M methanol/ 0.50 M KOH aqueous solution at room temperature. The current density was normalized by the weight of Pt loading. All electrochemical impedance spectroscopy (EIS) experiments were done in an Autolab Potentiostat/Galvanostat EGSPAT 12/30. A 1.0M methanol/ 0.50M KOH solution was used for methanol oxidation studies at an applied potential of -0.400 V vs. Ag/AgCl for catalysts. EIS was performed using a sine wave with an amplitude of 10 mV in the frequency range from 100 kHz to 1 MHz.

4.3 Results and Discussion

4.3.1 Structural and Chemical Composition Characterization

4.3.1.1 Crystal Structure and Chemical Composition Identification of Catalysts

To identify the crystal structures of ceria supports and Pt crystals, both Pt/ceria NRs and NPs were characterized by XRD. The XRD patterns of ceria supports displayed diffraction peaks corresponding to those of the fluorite structured cubic ceria ($Fm\bar{3}m$, JCPDS 00-34-0394). The Pt nanoparticles present in the catalyst were found to be $Fm\bar{3}m$ cubic platinum from the XRD peaks indexed against the ICDD reference (ICDD 00-004-0802) (Figure 4.1). The elemental compositions measured by ICP-OES confirmed that both catalysts contained an average of 20-24 wt.% Pt. The BET data indicated that before the Pt deposition step, the ceria NRs and NPs had similar initial surface areas (90 m^2/g vs. 83 m^2/g).

4.3.1.2 Morphology and Chemical State Study of Nanorod Catalysts

The STEM-HAADF images of Pt/ceria NRs showed uniform dispersions of Pt NPs on the ceria support (Figure 4.2a). The chemical contrast in the STEM images between ^{58}Ce and ^{78}Pt (Pt appears brighter) allowed for locating the Pt NPs. The diameter of Pt NPs was about 2 to 5 nm. The lengths and diameters of ceria NRs were 21.5 ± 8.5 nm and 7.3 ± 1.4 nm, respectively. Figure 4.2b shows a typical TEM image of the product that mainly contained faceted "hemispherical" shaped Pt nanocrystals. Side view images usually displayed solid anchoring of Pt NPs on ceria NRs as indicated by their faceted "hemispherical" shapes, suggesting a strong inter-diffusion between the Pt NPs and ceria. For examples, Figure 4.2b shows a Pt NP anchored on a ceria NR which grew

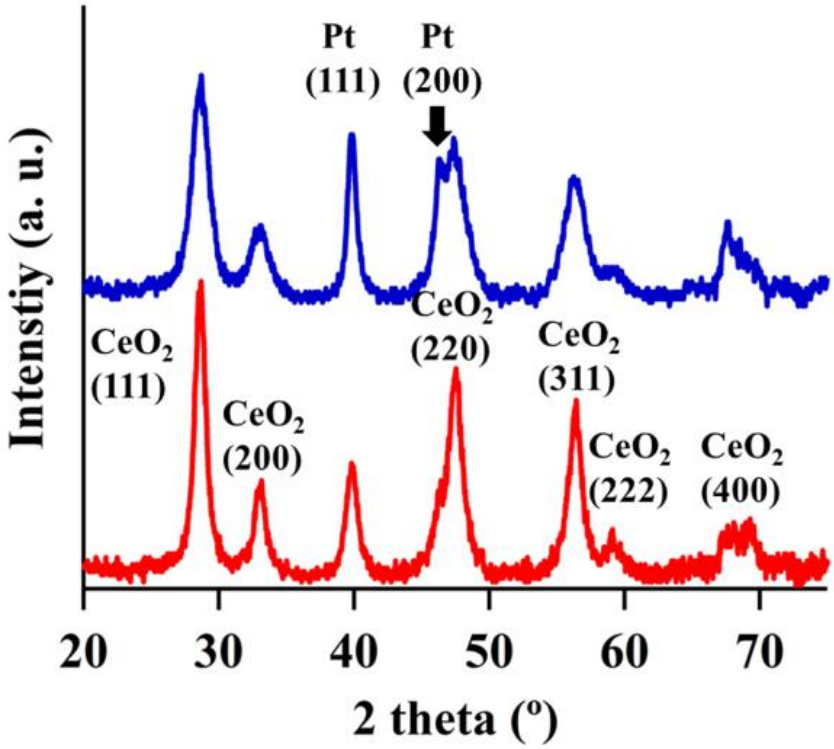

Figure 4.1 X-ray diffraction patterns of (top) Pt/ceria NPs catalyst and (bottom) Pt/ceria NRs catalyst.

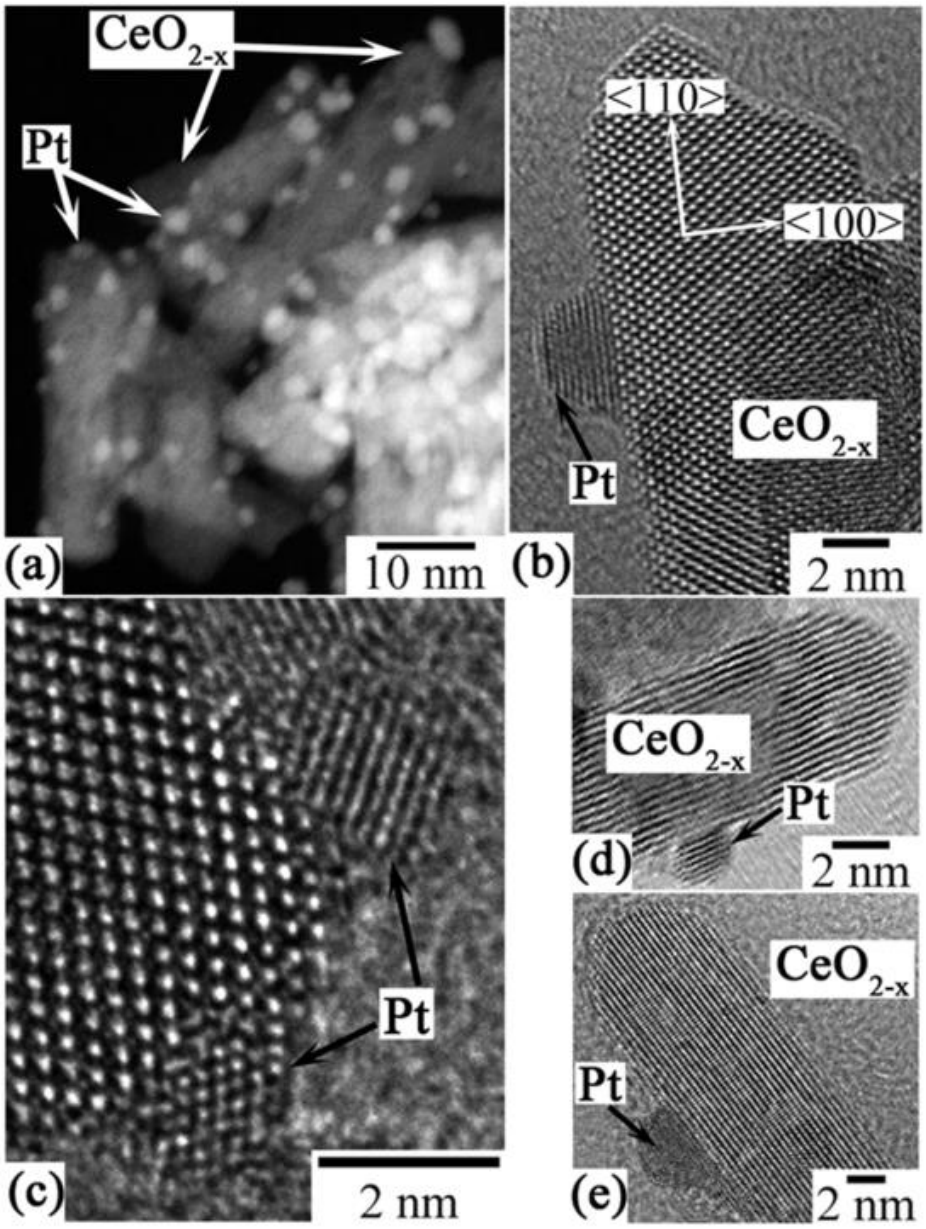

Figure 4.2 a) STEM HAADF and b, c, d and e) TEM images of the Pt/ceria NRs catalyst

along the <110> direction. Two Pt NPs anchored on the tip of a nanorod are shown in Figure 4.2c. The images in Figure 4.2d and 4.2e are typical and indicate that Pt NPs were solidly anchored on the NR surfaces. Indeed, a good anchorage of the Pt NPs is beneficial to avoid their agglomeration and segregation.

The XPS Ce 3d binding energy region for Pt/ceria NRs suggests the presence of Ce^{3+} and Ce^{4+} species (see Figure 4.3a). The Ce 3d spectrum was composed of two multiplets (v and u). These multiplets correspond to the spin-orbit splitting of $3d_{5/2}$ and $3d_{3/2}$ core electrons. The peaks labeled with v^0, v', u^0 and u' are indicative of Ce^{3+} peaks as opposed to those at v, v", v"', u, u" and u"' indicating the presence of Ce^{4+} states.[27] The XPS spectrum of Pt/ceria NRs has two spin-orbit splitting doublets Pt $4f_{7/2}$ and $4f_{5/2}$. The peaks at 71.1 and 72.8 eV binding energies are attributed to Pt^0 and Pt^{2+} states, respectively[28] (Figure 4.3b). The peak at 71.7 eV is ascribed to Pt-O-M peak which corresponds to slightly ionized Pt. M has been assigned to be either a Ce cation or an oxygen vacancy site.[25] The Pt 4f spectrum fitting indicated that the Pt NPs were composed of Pt^0 and a significant portion of Pt^{2+} and Pt^{4+} states. 53% of all Pt species in Pt/ceria NRs catalyst are in the Pt^0 state, whereas the other 47% species were composed of Pt-O-M, Pt^{2+} and Pt^{4+}. (See the fitting parameters in Table 4.1) The formation of higher oxidation states of Pt necessitates charge transfer from the Pt to ceria support and indirectly suggests strong interfacial interactions between the deposited Pt NPs and ceria NRs.[28] This strong interaction may alter the crystallography and electronic structure of the Pt NPs and consequently affect the morphology of the catalyst, such as immobilizing the Pt NPs and preventing the Pt NPs from aggregation.

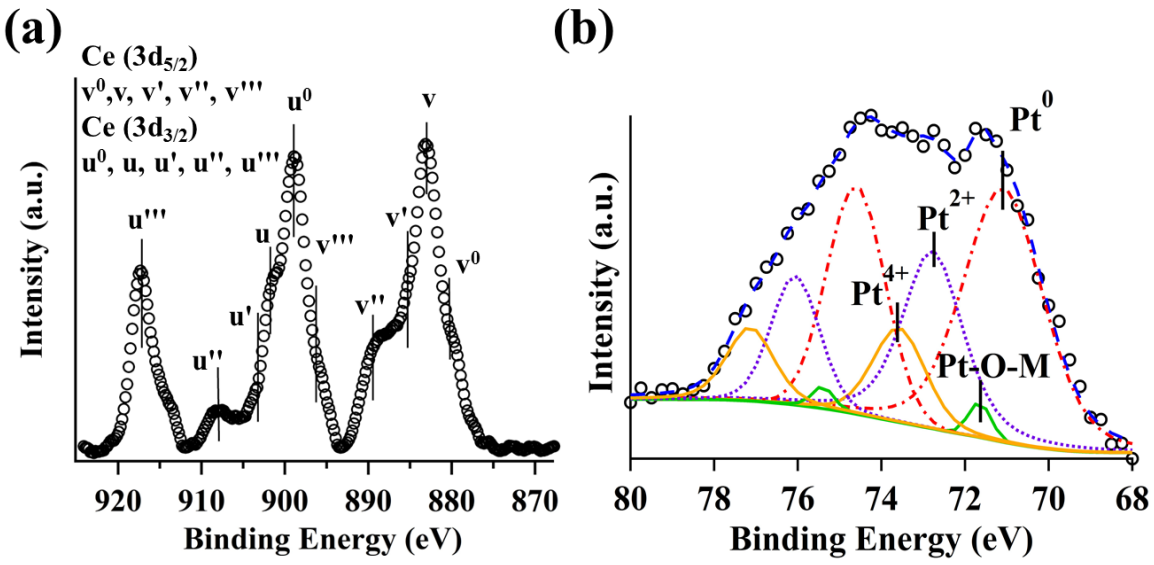

Figure 4.3 X-ray photoelectron spectra and analysis of a) Ce 3d and b) Pt 4f binding energy regions for Pt/ceria NRs.

Table 4.1 The fitting parameters for Pt 4f XPS data of Pt/ceria NRs.

Peak	Binding Energy (eV)	FWHM (eV)
Pt^0 ($4f_{7/2}$)	71.1	2.2
Pt-O-M ($4f_{7/2}$)	71.7	0.6
Pt^{2+} ($4f_{7/2}$)	72.8	1.7
Pt^{4+} ($4f_{7/2}$)	73.6	1.5
Pt^0($4f_{5/2}$)	74.6	1.7
Pt-O-M ($4f_{5/2}$)	75.4	0.6
Pt^{2+} ($4f_{5/2}$)	76.1	1.4
Pt^{4+} ($4f_{5/2}$)	77.1	1.3

4.3.1.3 Morphology and Chemical State Study of Nanoparticle Catalysts

In contrast, for Pt/ceria NPs, the supported Pt NPs, which had similar sizes as ceria NPs, were observed to be dispersed among the ceria NPs (See Figure 4.4). The sizes of ceria NPs were between 2 to 6 nm, similar to those of supported Pt NPs (2-5 nm). The Pt NPs were more spherical than the faceted hemispherical ones on ceria NRs. In Figure 4.4a, the top right inset shows two HAADF-STEM images demonstrating the presence and distribution of ceria and Pt NPs where the Pt NPs appear brighter. The other inset image is a higher magnification of the boxed area where one Pt NP and one ceria NP were identified. The shape of Pt NPs also appeared to be less impacted by the ceria NPs. They did not seem to anchor well on the ceria supports and their shape appeared very much like the free standing particle (See Figure 4.4b and 4.4c), suggesting insignificant atomic inter-diffusion between the Pt NPs and ceria support.

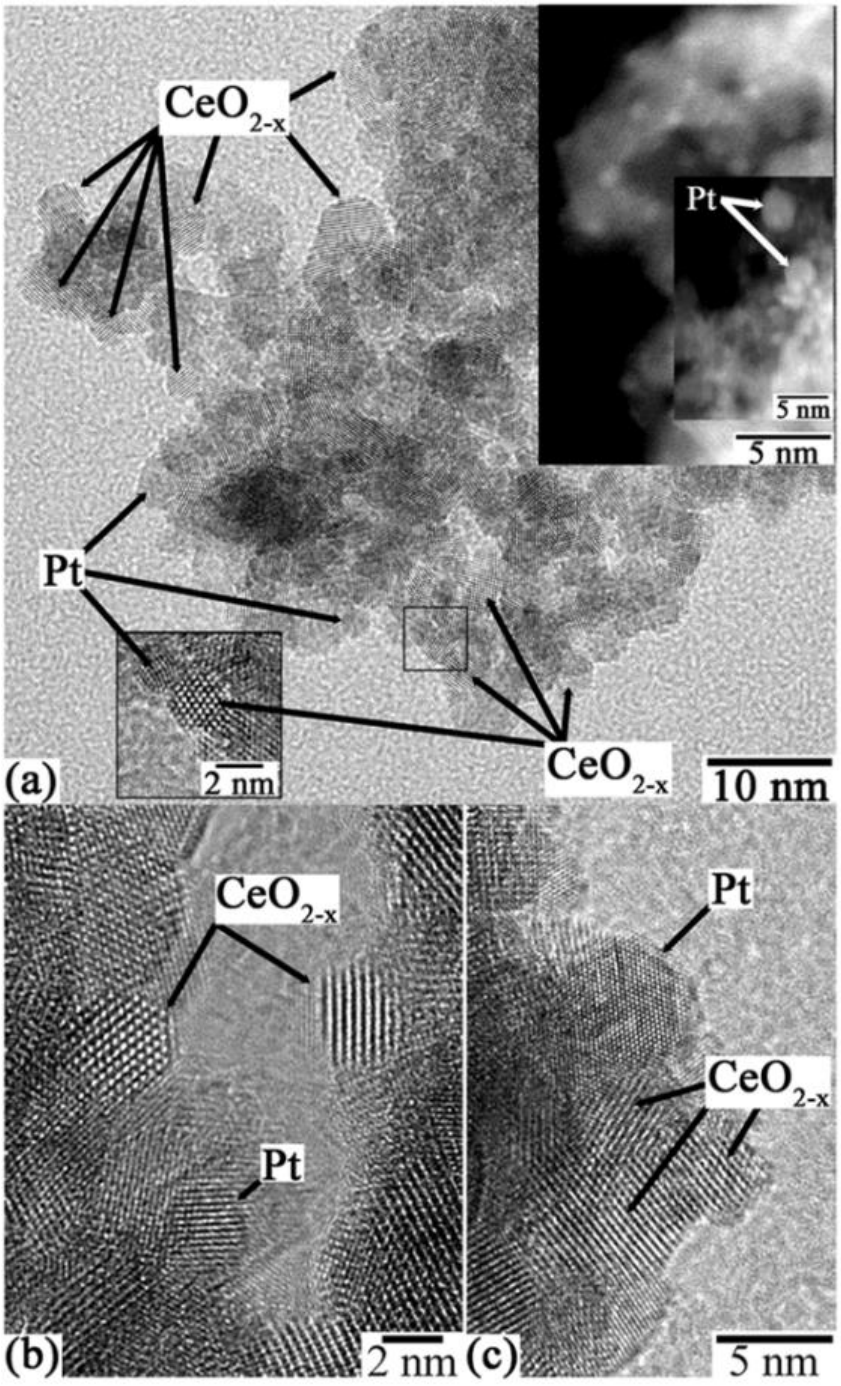

Figure 4.4 a, b and c) TEM images of the Pt/ceria NPs catalyst. The insets of 4a show two HAADF-STEM images.

Similar to the case of Pt/ceria NRs, XPS Ce 3d spectrum analysis also indicated the presence of both Ce^{3+} and Ce^{4+} states (see Fig. 5a). XPS Pt 4f spectrum revealed that the dominant species in the Pt NPs of Pt/ceria NPs were Pt^0 (71%). These Pt particles also contained a significant proportion of Pt in the 2+ state (28%) (See Fig. 5b). (See fitting parameters in Table 4.2) No Pt^{4+} state fitting peaks were found necessary to reconstruct the Pt spectrum. The Pt-O-M species present in Pt/ceria NPs (1%) were considerably less than those in the Pt/ceria NRs, suggesting less interactions between Pt NPs and ceria NPs. Moreover, the much larger proportion of Pt NPs in Pt^0 state suggests reduced charge transfers and weaker interactions between Pt NPs and ceria NPs when compared with the one in Pt/ceria NRs. The XPS analysis confirmed the data obtained from TEM experiments. With weaker interactions at the Pt/ceria interface, Pt nanocrystals easily agglomerate to form "spherically" shaped NPs.

4.3.2 Electrocatalytic Performances of Catalysts Electrodes Towards Methanol Oxidation

The electrocatalytic activities of both Pt/ceria catalysts towards methanol oxidation were investigated using CV in 0.50 M KOH at room temperature. The CVs showed redox peaks in the region of -300 mV to 200 mV, corresponding to methanol oxidation and in agreement with reported data (Figure 4.6a).[20, 29, 30] However, the current density per gram of Pt loading for the methanol electrooxidation with Pt/ceria NPs catalysts was about 2-5 folds larger than that with the Pt/ceria NRs catalysts from four data sets. This clearly reflects that the involvement of ceria NPs significantly increased the catalytic activity of the anode with the same Pt loadings. In addition, in Fig. 6a, the

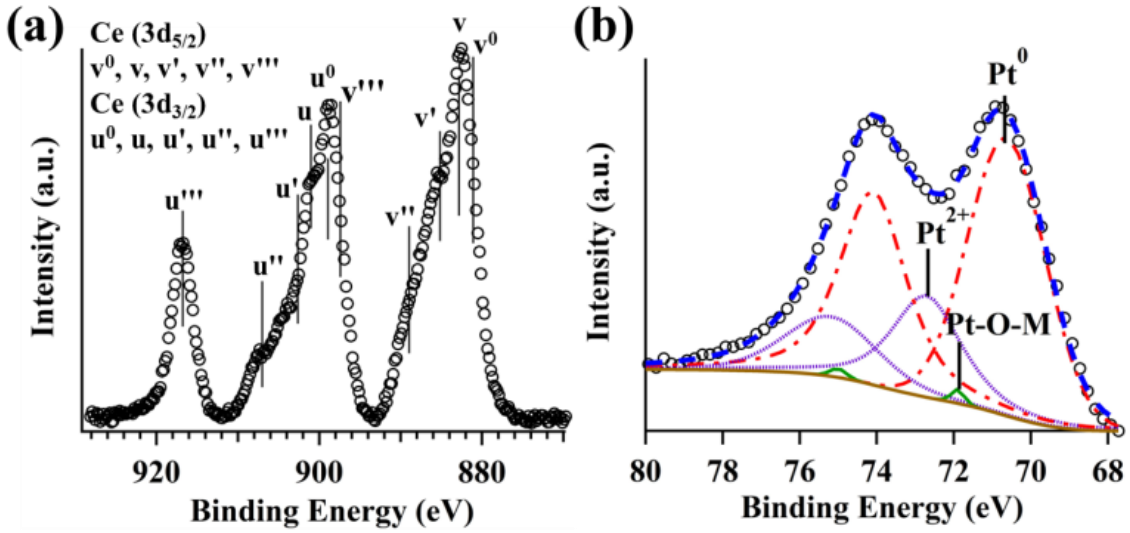

Figure 4.5 X-ray photoelectron spectra and analysis of (a) Ce 3d and (b) Pt 4f data of Pt/ceria NPs.

Table 4.2 The fitting parameters for Pt 4f XPS data of Pt/ceria NPs.

Peak	Binding Energy (eV)	FWHM (eV)
Pt^0 ($4f_{7/2}$)	70.6	2.4
Pt-O-M ($4f_{7/2}$)	71.9	0.4
Pt^{2+} ($4f_{7/2}$)	72.7	2.1
Pt^0($4f_{5/2}$)	74.1	2.0
Pt-O-M ($4f_{5/2}$)	75.0	0.5
Pt^{2+} ($4f_{5/2}$)	75.2	2.8

peak potential of anodic sweep for Pt/ceria NPs is -0.103 V vs. Ag/AgCl, while it is -0.082 V for Pt/ceria NRs. The peak potential shift indicates that the methanol oxidation on Pt/ceria NPs electrode is more active than that on Pt/ceria NRs electrode, which is consistent with the conclusion from our current density results.[20] The onset potential values of both catalysts also suggested that Pt/ceria NPs is a higher-performance anode catalyst since the onset potential is smaller than the one in Pt/ceria NRs. Thus, thermodynamically, the electrooxidation of methanol is more favorable with Pt/ceria NPs catalyst. The onset potential values defined at 5% of the maximum peak current density for the methanol oxidation reaction performed with the catalysts coated anodes are shown in the forward sweep of the cyclic voltammograms obtained at a scan rate of 1 mV/s in Figure 4.6b. Pt/ceria NPs exhibited an onset potential of -0.367 V vs. Ag/AgCl while that of Pt/ceria NRs is slightly higher at -0.333V vs. Ag/AgCl.

The electrocatalytic activity of Pt/ceria catalysts is mostly attributed to the Pt^0 species of the Pt NPs. Pt^0 provides the most catalytically active sites for methanol electrooxidation.[31] The electrocatalytic performance of these catalysts suggests that Pt/ceria NPs had more catalytically active sites than Pt/ceria NRs. This is confirmed by the Pt active surface area measurements via hydrogen adsorption/oxidation potential region of the CV data (Figure 4.7). This finding also corroborates our XPS data that Pt/ceria NPs catalysts contain more Pt^0 states, but less oxidized Pt species. The higher catalytic activity of Pt/ceria NPs is also reflected indirectly by its lower electrical resistance in our EIS study. Nyquist plots were used to compare the resistance of charge transfer in both catalysts in 1.0 M MeOH/ 0.50 M KOH at an applied potential of -400

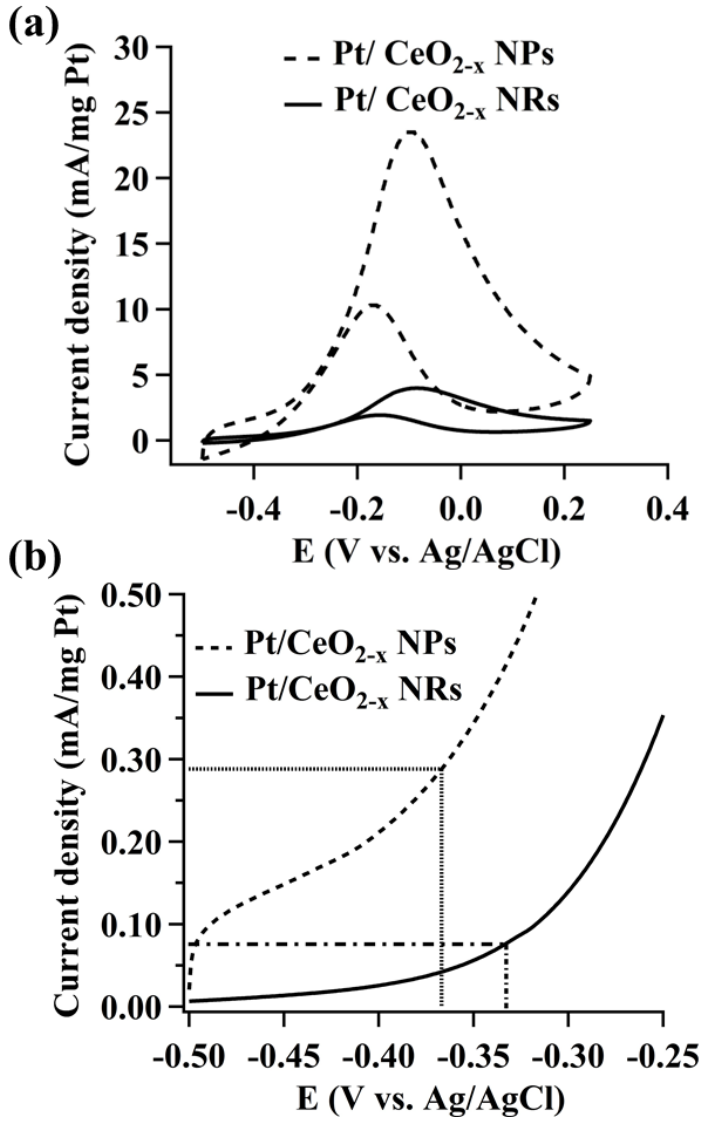

Figure 4.6 (a) Cyclic voltammograms of Pt NPs on (solid) ceria NRs and (dotted) ceria NPs for alkaline methanol oxidation at a scan rate of 100 mV/s in 1.0 M MeOH/ 0.50 M KOH solutions. (b) Onset potential determination of Pt/ceria NRs and Pt/ceria NPs for alkaline methanol oxidation at a scan rate of 1 mV/s.

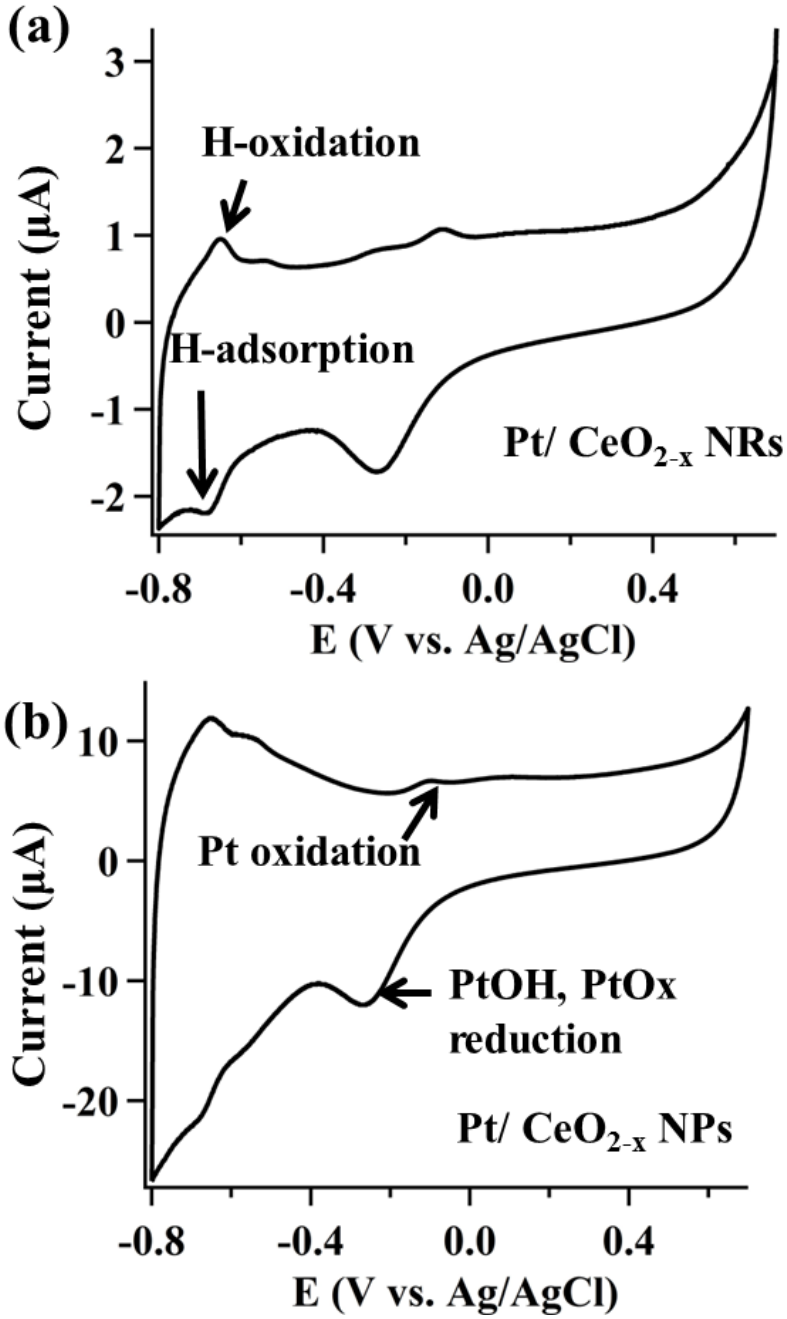

Figure 4.7 Cyclic voltammetry of (a) Pt/ceria NRs and (b) Pt/ceria NPs catalysts in 0.50 M KOH at 50 mV/s. The hydrogen adsorption and Pt oxidation and PtOH reduction are identified.

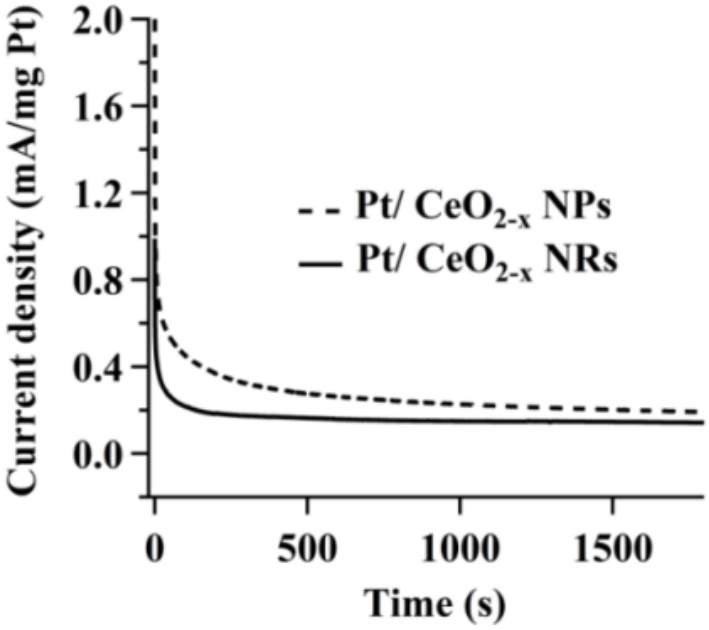

Figure 4.8 Chronoamperometric responses of Pt/ceria NRs and Pt/ceria NPs catalysts performed at an applied potential of -0.350 V vs. Ag/AgCl in 1.0 M methanol/ 0.50 M KOH solutions.

mV vs. Ag/AgCl. The charge-transfer resistance was significantly smaller for the catalysts with ceria NPs than for the NRs catalysts. This result allows us to conclude that the methanol electrooxidation in alkaline media has more favourable conditions when using the ceria NPs catalyst than the NRs material.

The catalytic activity of the catalyst-coated electrodes was also examined using chronoamperometry at an applied potential of -0.350 V vs. Ag/AgCl in 1.0 M methanol/ 0.50 M KOH solutions (Figure 4.8). The observed current density for both catalysts decayed to *ca.* 0.2 mA/mg of Pt at 30 min. However, the Pt/ceria NPs exhibited slower decaying rate and slightly higher steady current density than those of Pt/ceria NPs. This observation confirms our CV results and is ascribed to the higher proportion of metallic Pt in the Pt/ceria NPs.

From the experimental results, the morphological differences between Pt/ceria NRs and NPs can be summarized in Scheme 1. The observed physical morphology and oxidation states of Pt NPs on the ceria NRs and NPs supports and their resulting catalytic activities can be attributed to the relative size differences and the degree of interactions between the Pt NPs and the ceria crystal plane facets. The ceria NRs provided relatively larger sized facets which allowed the deposited Pt NPs to spread and adopt an approximately faceted "hemispherical" morphology during the catalyst thermal activation step (Left model in Scheme 4.1). In contrast, Pt NPs were found to attain more "spherical" shapes among the ceria nanoparticle aggregates. This was likely because, during the thermal activation process, the curvature-driven surface self-diffusion[32] of Pt atoms tended to reform NPs on jagged surfaces of aggregated ceria NPs upon thermal treatments (Right model in Scheme 4.1). The several surface contact points between each

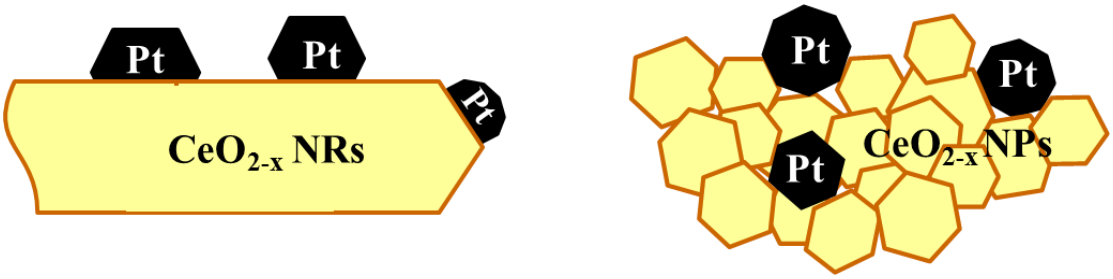

Scheme 4.1 Schematic of the postulated structural relationship between Pt NPs and ceria support for (right) Pt/ceria NRs and (left) Pt/ceria NPs. Pt NPs: black; ceria (CeO_{2-x}): yellow.

Pt NP with multiple ceria NPs of similar sizes may promote the Pt NPs to adopt more "spherical" shapes. The Pt NPs formed on ceria NRs contained more oxidized Pt species than those on ceria NPs. This implied that the ceria NRs had stronger interactions with supported Pt NPs than the case of ceria NPs. The strong metal support interactions were postulated to alter the morphology, increase the oxidation states of Pt and consequently decrease the availability of metallic Pt^0 sites and catalytic activity for methanol electrooxidation.

4.4 Conclusions

In summary, nanostructured ceria supports (NRs and NPs) were found to have significant effects on the chemical states of Pt NPs and hence their catalytic activities towards methanol oxidation in alkaline media. Pt NPs had a tendency to anchor strongly on ceria NRs due to their larger facets. However, Pt/ceria NRs showed higher concentrations of oxidized Pt species, therefore causing a decrease in their catalytic activity towards the electrooxidation of methanol in an alkaline media than in the case of Pt/ceria NPs. Our results suggest that though ceria has been widely explored as the promoter oxides for many metal-NPs-based electrocatalysts, the choice of morphology and size of the oxide promoter supports should also be carefully considered in the catalyst design.

4.5 References

1 M. Warshay and P. R. Prokopius, *J. Power Sources*, 1990, **29**, 193-200.

2 R. E. Martin and M. A. Manzo, *Proc. Intersoc. Energy Convers. Eng. Conf.*, 1988, 23rd, 301-304.

3 V. I. Matryonin, A. T. Ovchinikov and A. P. Tzedilkin, *Int. J. Hydrogen Energy*, 1997, **22**, 1047-1052.

4 V. S. Bagotzky and Y. B. Vassilyev, *Electrochim. Acta*, 1967, **12**, 1323-1343.

5 A. Hamnett, *Catal. Today*, 1997, **38**, 445-457.

6 A. M. Feltham and M. Spiro, *Chem. Rev.*, 1971, **71**, 177-193.

7 Z. L. Zhang, H. Song, S. B. Liu, Y. B. Li, X. G. Hao, D. H. Duan and Y. P. Sun, *Rare Metal Mat. Eng.*, 2012, **41**, 58-63.

8 R. S. Amin, R. M. A. Hameed, K. M. El-Khatib, M. E. Youssef and A. A. Elzatahry, *Electrochim. Acta*, 2012, **59**, 499-508.

9 N.-Y. Hsu, C.-C. Chien and K.-T. Jeng, *Appl. Catal. B*, 2008, **84**, 196-203.

10 M. M. P. Janssen and J. Moolhuysen, *Electrochim. Acta*, 1976, **21**, 869-878.

11 J. Zhao, L. Zhang, H. Xue, Z. Wang and H. Hu, *RSC Adv.*, 2012, **2**, 9651-9659.

12 B. Singh and E. Dempsey, *RSC Adv.*, 2013, **3**, 2279-2287.

13 F. Si, L. Ma, C. Liu, X. Zhang and W. Xing, *RSC Adv.*, 2012, **2**, 401-403.

14 S. A. Hayes, P. Yu, T. J. O'Keefe, M. J. O'Keefe and J. O. Stoffer, *J. Electrochem. Soc.*, 2002, **149**, C623-C630.

15 D. R. Ou, T. Mori, K. Fugane, H. Togasaki, F. Ye and J. Drennan, *J. Phys. Chem. C*, 2011, **115**, 19239-19245.

16 C. Bianchini and P. K. Shen, *Chem. Rev.*, 2009, **109**, 4183-4206.

17 E. H. Yu, K. Scott and R. W. Reeve, *J. Electroanal. Chem.*, 2003, **547**, 17-24.

18 H. B. Yu, J.-H. Kim, H.-I. Lee, M. A. Scibioh, J. Lee, J. Han, S. P. Yoon and H. Y. Ha, *J. Power Sources*, 2005, **140**, 59-65.

19 Q. Tang, Z. Mao, S. Ma and K. Huang, *RSC Adv.*, 2012, **2**, 11465-11471.

20 C. W. Xu and P. K. Shen, *Chem. Commun.*, 2004, 2238-2239.

21 N. J. Lawrence, J. R. Brewer, L. Wang, T.-S. Wu, J. M. Wells-Kingsbury, M. M. Ihrig, G. Wang, Y.-L. Soo, W. N. Mei and C. L. Cheung, *Nano Lett.*, 2011, **11**, 2666-2671.

22 D. Valechha, S. Lokhande, M. Klementova, J. Subrt, S. Rayalu and N. Labhsetwar, *J. Mater. Chem.*, 2011, **21**, 3718-3725.

23 D. Zhang, X. Du, L. Shi and R. Gao, *Dalton Trans.*, 2012, **41**, 14455-14475.

24 Z. Wu, M. Li and S. H. Overbury, *J. Catal.*, 2012, **285**, 61-73.

25 K. Fugane, T. Mori, D. R. Ou, A. Suzuki, H. Yoshikawa, T. Masuda, K. Uosaki, Y. Yamashita, S. Ueda, K. Kobayashi, N. Okazaki, I. Matolinova and V. Matolin, *Electrochim. Acta*, 2011, **56**, 3874-3883.

26 L. Cunci, C. Rao, C. Velez, Y. Ishikawa and C. Cabrera, *Electrocatalysis*, 2013, **4**, 61-69.

27 S. Deshpande, S. Patil, S. V. N. T. Kuchibhatla and S. Seal, *Appl. Phys. Lett.*, 2005, **87**.

28 Q. Fu, H. Saltsburg and M. Flytzani-Stephanopoulos, *Science*, 2003, **301**, 935-938.

29 S. S. Mahapatra and J. Datta, *Int. J. Electrochem.*, 2011, **2011**, 1-16.

30 E. Hao Yu, K. Scott and R. W. Reeve, *J. Electroanal. Chem.*, 2003, **547**, 17-24.

31 D. Santiago, G. G. Rodriguez-Calero, H. Rivera, D. A. Tryk, M. A. Scibioh and C. R. Cabrera, *J. Electrochem. Soc.*, 2010, **157**, F189-F195.

32 C. V. Thompson, *Annu. Rev. Mater. Res.*, 2012, **42**, 399-434.

CHAPTER 5

PREPARATION AND CHARACTERIZATION OF PLATINUM/CERIUM OXIDE CATALYSTS FOR SMALL CHAIN ALCOHOL ELECTROOXIDATION

5.1 Introduction

Fuel cells are efficient and low-to-zero pollutant emission sources of energy which have a wide range of potential applications in transportation vehicles and portable devices.[1] Alkyl alcohols with short carbon chains such as methanol, ethanol and n-butanol have been commonly proposed as alternative fuels because they possess higher energy density per weight when compared to gas fuels.[2] Among the direct alcohol fuel cells (DAFCs), direct methanol fuel cells (DMFC) have been extensively studied and evaluated for vehicle transportation applications partially because of the ease of large scale industrial methanol production.[3] The bio-renewable nature of ethanol and its lower toxicity make it as another attractive alternative of alcohol fuels. [4, 5] Though the energy densities of ethanol are 30+% higher than that of methanol (8.01 kWh kg^{-1} versus 6.09 kWh kg^{-1}),[6] the current efficiency of direct ethanol fuel cells reported in literature is typically less than those observed with direct methanol fuel cells. Despite the fact that n-butanol has even higher energy density (9.95 kWh kg^{-1}), comparable to that of petrol fuel,[7] the reported performances of n-butanol in direct fuel cells are generally even poorer. The major reasons for the lower performances of ethanol and n-butanol are commonly attributed to the severe difficulty to break the C-C bonds in these short carbon chain structures and the poisoning of noble metal catalysts used in traditional DAFC designs.[8]

To mitigate the poisoning of commonly used platinum (Pt) catalysts in fuel cells, various oxide promoters such as WO_3,[9] TiO_2,[9] Ta_2O_5,[10] NbO_2[11] and CeO_{2-x}[12] have been

studied. These oxides were designed to support the Pt catalyst and assist oxidizing catalyst poisons such as carbon monoxide and other partially oxidized carbonaceous by-products from the alcohol electrooxidation process. Cerium oxide (ceria, CeO_{2-x}, $0<x\leq0.5$) is one of the promising promoter oxide [13-15]due to its high oxidizing power and its excellent oxygen storage and release ability to abate these by-products.[8,15,16] Ceria are typically applied as embedded materials in composites with platinum, platinum-ruthenium, platinum-carbon catalysts.[17-21] Various methods of fabricating Pt-ceria composite anodes have been employed, such as occlusion deposition,[22] chemical vapor deposition,[23] sputtering[24] and "catalyst paste" mixtures of metal precursors, support and conducting polymers.[25] Since different shapes of nanostructured ceria possessed different oxidizing power based on the density of oxygen vacancy defects,[26-28] many different shapes of ceria catalyst, including nanoparticles,[22] nanorods[29] and nanowires[30] have been studied. Ceria nanorods were found to possess larger density of oxygen vacancy defects and exhibit higher catalytic activity towards reactions, such as CO oxidation.[31]

Preparation methods and pre-treatments of Pt-ceria catalysts are critical in altering their resulting structures, chemical states and hence catalytic performance. For example, Ou et al. recently reported that annealing of Pt decorated polycrystalline ceria nanorods support in hydrogen could promote Pt nanoparticles to "invade" into the ceria structure and create a composite of smaller nanocrystalline ceria particles decorating on the Pt particles.[32] The "invasion" of Pt in the ceria support under highly reducing environment suggests that more gentle catalyst preparation process for ceria supported Pt catalysts should be further explored.

Literature reports investigating the performance of Pt-ceria catalyst on alcohol electrooxidation reveal that the optimum Pt/ceria molar ratio of this catalyst system varies significantly for different alcohol fuels.[33] Importantly, such an optimum ratio was found to strongly depend on the Pt-ceria interaction, which is significantly impacted by the catalyst preparation methods. Since ceria is a wide band-gap semiconductor and has low current conductance, a large content of pure ceria in the catalyst generally is expected to suppress the current produced from alcohol electrooxidation because of the increase in electrode resistance and the blocking of platinum catalytic sites.[34] Nonetheless, few literatures focused on studying the impedance effect of ceria support to seek to improve the effectiveness of the Pt-ceria catalyst system.

Herein we report a multi-functional composite catalyst made of platinum nanoparticles supported on 2 wt.% Pt decorated CeO_{2-x} nanorods for the electrooxidation of methanol, ethanol and n-butanol in alkaline media. Our study focuses on using an anode "ink paste" composite catalyst composed of 2 wt.% Pt decorated ceria ($Pt:CeO_{2-x}$) nanorods, electrochemically deposited Pt nanoparticle clusters and conducting polymers. The composite catalysts (abbreviated as $Pt/Pt:CeO_{2-x}$) were synthesized by a multi-step method. The $Pt:CeO_{2-x}$ nanorods were synthesized using an adapted hydrothermal method, followed by wet impregnation of platinum salts to increase their electrical conductivity.[28] Pt nanoparticles were then electrochemically synthesized and deposited at a controlled potential onto glassy carbon (GC) electrodes pre-coated with a catalyst "ink-paste" composed of $Pt:CeO_{2-x}$ nanorods and Fumion® polyelectrolytes. Highly crystalline ceria nanorods were chosen over other nanostructures because it was reported to have higher oxidizing power when thermally activated under low pressure.[28] Composite

catalysts of Pt nanoparticle clusters and Pt:CeO_{2-x} nanorods were further demonstrated in enhancing the efficiency of direct alcohol oxidation over similarly prepared anode catalysts with pure ceria nanorods and also the Pt nanoparticles catalyst. These findings provide further perspectives on increasing the electrical conductance of the promoter oxide and thus improvement of the direct electrooxidation of alcohols.

5.2 Experimental Method

5.2.1 Preparation of Platinum/Cerium Oxide Catalysts

2 wt.% Pt:CeO_{2-x} nanorods were prepared using a modified hydrothermal procedure for synthesizing ceria nanorods.[28] A mixture of 0.5 g of cerium (III) sulphate and 40 mL of 10 M sodium hydroxide in a 50-mL capacity Teflon-lined stainless steel autoclave was hydrothermally treated at 120 °C for 15 h. in a convection oven to produce cerium (III) hydroxide nanorods. The filtered product was rinsed with three aliquots of 50 mL of water and then placed in a convection oven for another 2 h. at 50 °C for further oxidation. Subsequently, 25 mL of water, and 1.536 mL of 0.02 M potassium tetrachloroplatinate(II) (K_2PtCl_4) solution were mixed with the nanorods and stirred for 20 min. Afterwards, 25 mL of 30 % aqueous hydrogen peroxide was added to the mixture and sonicated for 30 min., followed by mechanical stirring for an additional 30 min. to achieve complete reaction. The resulting products were filtered, rinsed with three aliquots of 50 mL of 18 MΩ·cm deionized water, and dried for 4 h. at 50 °C in a convection oven. Before use, the synthesized materials were activated at 400 °C in a flow of 100 SCCM (standard cubic centimeter per minute) of simulated air (20 % O_2/ 80 % N_2) for 30 min. in a horizontal quartz tube furnace at an operating pressure of 2.0 Torr.

5.2.2 Preparation of Catalyst Coated Glassy Carbon (GC) Electrodes

Coating of Pt nanoparticles/Pt:CeO_{2-x} nanorods (Pt/Pt:CeO_{2-x}) catalyst onto glassy carbon (GC) electrodes was accomplished using a two-step process. For the first step, the catalyst "ink" paste mixture was made by mixing 1 mg of 2 wt.% Pt:CeO_{2-x} nanorods, 100 µL of nanopure water of 18 MΩ·cm resistivity, 200 µL of isopropanol, and 8 µL of Fumion® (5 % w/w polyarylene sulfonic acid polyelectrolyte dissolved in water/isopropanol, FuMA-Tech GmbH, St. Ingbert, Germany). Afterwards, the "ink" mixture was sonicated for 60 s and stirred for 10 min. to increase its composition uniformity. 8 µL of the "ink" paste was then drop-casted onto the surface of a clean GC electrode. Typically, the deposited "ink" dried on the electrode after 30 min. of exposure to ambient conditions. For the second step, Pt nanoparticles were electrodeposited onto the modified GC electrode by applying a constant potential of -0.200 V vs. Ag/AgCl for 30 s at room temperature while the electrode was immersed in an aqueous 1 mM K_2PtCl_6/ 0.5 M H_2SO_4 solution.

Coating of Pt nanoparticles/CeO_{2-x} nanorods (Pt/CeO_{2-x}) catalyst onto GC electrodes for the control experiments was performed similarly as that for the Pt/Pt:CeO_{2-x} coated GC electrodes except that CeO_{2-x} nanorods were used instead. Pt nanoparticles coated GC electrodes were fabricated by electrodepositing Pt nanoparticles to a modified "ink" paste (without 1 mg CeO_{2-x} nanorods catalyst) deposited GC electrodes by applying a constant potential of -0.200 V vs. Ag/AgCl for 30 s at room temperature while the electrodes were immersed in aqueous 1 mM K_2PtCl_6/ 0.5 M H_2SO_4 solutions.

5.2.3 Characterization of Catalysts Morphology, Structure and Composition

The structure and chemical identity of the 2 wt.% Pt:CeO_{2-x} nanorods was studied by transmission electron microscopy (TEM), energy dispersive X-ray spectroscopy (EDX), X-ray powder diffraction (XRD), inductive coupled plasma optical emission spectroscopy (ICP-OES) and X-ray photoelectron spectroscopy (XPS). TEM micrographs and selected area electron diffraction of the samples were obtained using a Tecnai G^2 F20 S-Twin field-emission TEM operated at 200 kV (FEI Company, Hillsboro, OR). The EDX spectra of the imaged sample were determined with an Oxford Instruments EDX system (Oxford Instruments, Oxfordshire, UK). The crystal structures of the nanorods were examined with a Bruker Discover D8 (Bruker AXS, Madison, WI). The XRD instrument was equipped with a Cu Kα X-ray source of average wavelength 1.544 Å. Elemental composition of the 2 wt.% Pt:CeO_{2-x} nanorods was analyzed using a Thermo Jarrell Ash IRIS Advantage Inductively Coupled Plasma Optical Emission Spectrometer. The XPS analysis of the nanorods was performed using a PHI 5600ci spectrometer equipped with a hemispherical electron analyser and a monochromatic Al Kα X-ray source operated at 15 kV and 350 W. The recorded binding energy data was calibrated using the carbon 1s peak. The software XPSPEAK was used for the Pt 4*f* XPS data fitting analysis.

The morphology of the catalysts-coated GC electrodes was investigated using a scanning electron microscope (SEM) operated at 2 to 5 kV (Hitachi High Technologies America, Inc., Pleasanton, CA). Elemental mapping of the catalysts-coated electrodes was obtained using a FEI Nova NanoSEM450 (FEI Company, Hillsboro, OR) operated at

20 kV and equipped with an Oxford Instruments EDX system (Oxford Instruments, Oxfordshire, UK).

5.2.4 Cyclic Voltammetry and Constant Potential Experiments

All cyclic voltammetry (CV) experiments were performed in a 3-electrode conventional electrochemical cell using a potentiostat (Electrochemical System PARC EG&G Instruments and CHI Model 1200B) by applying a direct current voltage at 100 mV/s vs. Ag/AgCl at room temperature. The counter electrode was a Pt wire. All electrolyte solutions were bubbled with argon gas for 10 min. before use. The active surface areas of platinum on the catalyst coated anodes (working electrodes) were calculated from the cyclic voltammograms in 0.1 M KOH solutions using the adsorption/desorption of hydrogen method. The half-cell studies were performed in 1 M alcohol (methanol, ethanol or n-butanol)/ 0.1 M KOH solutions. The controlled potential experiments to study the catalytic activity of the composites were performed at the onset potential in 1 M alcohol/ 0.1 M KOH solution as well.

5.2.5 CO Stripping Experiment

For the CO stripping experiment in alkaline medium, the electrodes were placed in a solution of 0.1M KOH using an Ag/AgCl reference electrode and a Pt wire as the counter electrode. The first step was to bubble high purity N_2 gas to purge the solution for 20 min. Then, CO gas was bubbled into the solution at a potential of -0.7 V vs. Ag/AgCl for 10 min. Afterwards, the potential of -0.7 V vs. Ag/AgCl was applied while high purity N_2 gas was bubbled to purge the remaining CO present in solution. The final step

was to perform a linear sweep voltammetry (LSV) from -0.7 V to 0.7 V vs. Ag/AgCl with a sweep rate of 20 mV/s.

5.3 Results and Discussion

5.3.1 Morphology, Structure and Chemical Composition of Anode Catalysts

The structure and chemical identity of 2 wt.% Pt:CeO_{2-x} nanorods were verified by our TEM and XRD studies. From the TEM images in Figure 5.1a, the as-synthesized materials were found to have nanorod shapes with diameters of 10-20 nm and lengths of 30-200 nm. Figure 5.1b shows the XRD diffraction pattern for the 2 wt.% Pt:CeO_{2-x} catalysts. The XRD pattern exhibited fluorite crystal structure similar to that of cerium(IV) oxide (CeO_2).[35] Neither platinum, platinum hydroxide nor platinum oxide species were revealed by our TEM or XRD data, likely due to the well-dispersed platinum on the ceria nanorods and the detection limit of these techniques. Nonetheless, ICP-OES analysis verified the weight percentage of Pt to be 2 wt.% in the Pt:CeO_{2-x} nanorod samples.

The deposited Pt forms different species on the surface of the ceria nanorods support. The Pt species also modifies the ceria nanorods due to the strong metal support interaction. The XPS spectrum of 2 wt.% Pt:CeO_{2-x} nanorods has two spin-orbit splitting doublets Pt $4f_{7/2}$ and $4f_{5/2}$. The peaks at 70.5 eV and 72.9 eV binding energies were attributed to Pt^0 and Pt^{2+} states, respectively.[36] (Figure 5.2) The peak at 71.9 eV was assigned to Pt-O-M peak which corresponds to slightly ionized Pt. M has been assigned

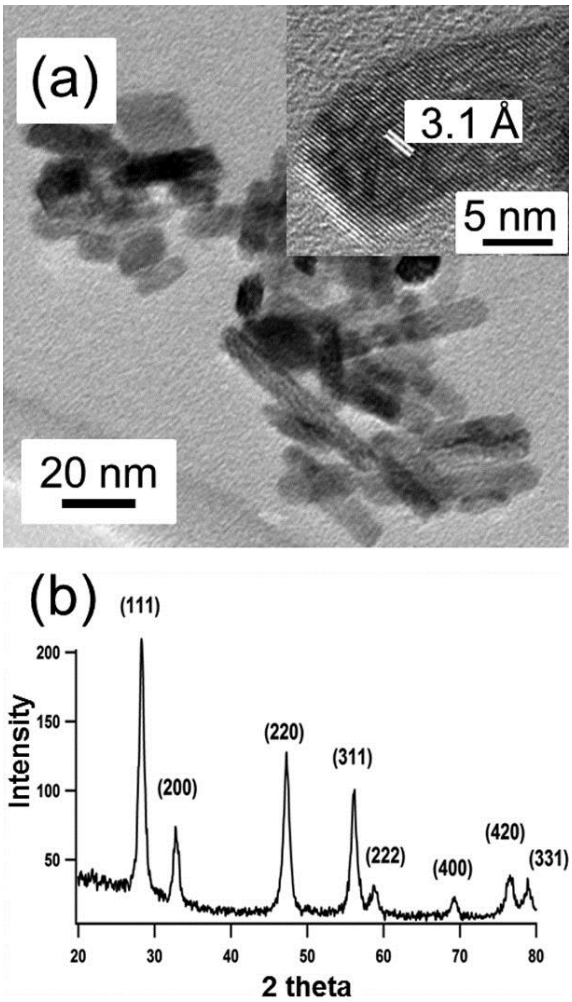

Figure 5.1 (a) TEM image of 2 wt.% Pt:CeO_{2-x} nanorods. (Inset) High-resolution TEM image of one nanorod. (b) XRD pattern of the Pt:CeO_{2-x} nanorods (Peaks indexed against fluorite-structured ceria)

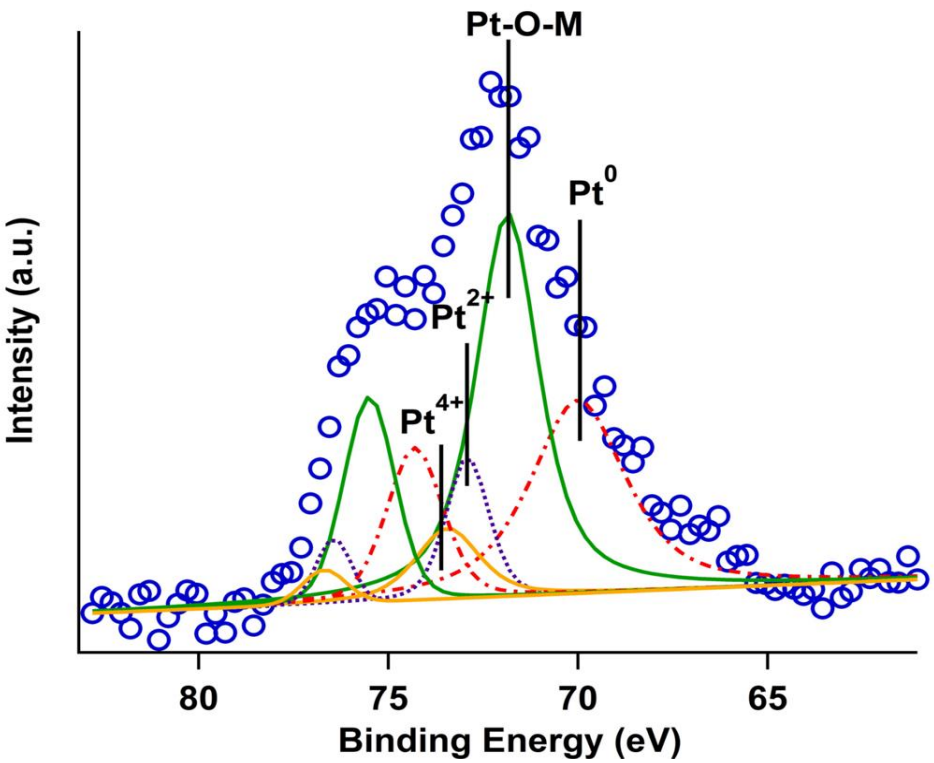

Figure 5.2 X-ray photoelectron spectra and fitting analysis of Pt 4*f* binding energy regions for 2 wt.% Pt:CeO_{2-x} nanorods.

to be either a Ce cation or an oxygen vacancy site.[37] At the binding energy of 73.4 eV, a small peak was fitted according to Pt^{4+}. The fitting analysis of the Pt 4*f* spectrum suggests that the Pt species on the ceria nanorods composed a significant portion of Pt^0 states (36%) and Pt-O-M states (46%). Small percentages of Pt species are in the states of Pt^{2+} (10%) and Pt^{4+} (8%).

Figure 5.3a is a schematic representation of the final composite electrode with an ink paste and platinum electrodeposited nanoparticles. The surface morphology of the Pt/Pt:CeO_{2-x} catalyst coating on a GC anode typically displays complex structures of Pt nanoparticle clusters among Pt:CeO_{2-x} nanorods/Fumion® "ink paste". Under SEM, the "ink paste" of Pt:CeO_{2-x} nanorods often existed as either rod or irregularly shaped structures with sizes ranging from a few 100 nanometers to a few microns as indicated by thin arrows in Figure 5.3b. The agglomeration of Pt:CeO_{2-x} nanorods to form larger particles were likely promoted by the Fumion® polymer. The electrochemically deposited clusters of Pt nanoparticles have diameters of 100 to 600 nm and are dispersed on the top of the catalyst coating. (Thick arrows in Figure 5.3b) The size distribution is similar to those of electrodeposited Pt nanoparticles on only Fumion® coated GC electrodes. The presence and distribution of platinum, cerium and oxygen in this catalyst composite coating is confirmed by EDX elemental mapping analysis. (Figure 5.4) The fluorine and sulfur signatures verify the presence of the Fumion®.

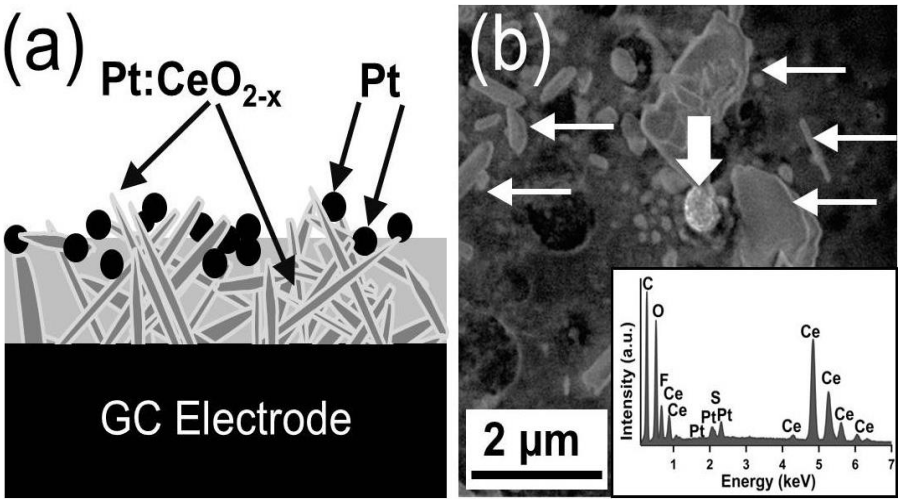

Figure 5.3 (a) Cross-sectional schematic of Pt/Pt:CeO_{2-x} catalyst coating on a glassy carbon (GC) electrode. (rods) Pt:CeO_{2-x} nanorods, (black circles) electrodeposited Pt nanoparticle clusters and (light grey) Fumion® polymeric conductor layer. (b) SEM image of an electrocatalyst Pt/Pt:CeO_{2-x}/ Fumion® coating on a glassy carbon electrode. (Thin arrows: Pt/Pt:CeO_{2-x} catalyst clusters; thick arrows: Pt nanoparticle clusters)

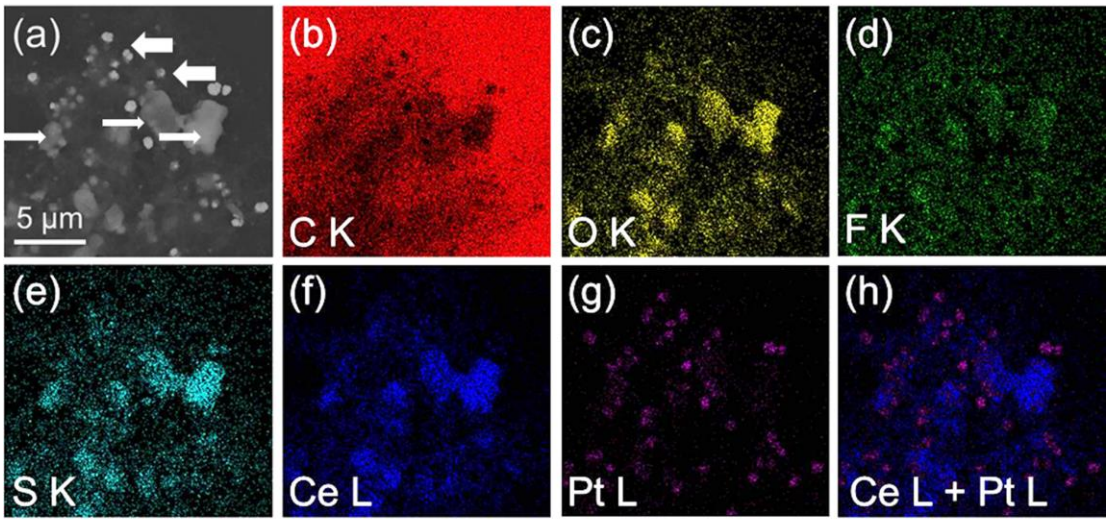

Figure 5.4 (a) SEM image of an electrocatalyst Pt/Pt:CeO_{2-x}/ Fumion® coating on a glassy carbon electrode. (Thin arrows: Pt/Pt:CeO_{2-x} catalyst clusters; thick arrows: Pt nanoparticle clusters) EDX elemental mapping of (b) carbon (red), (c) oxygen (yellow), (d) fluorine (dark blue), (e) sulfur (cyan), (f) cerium (green) and (g) platinum (magenta) of the catalyst coating in (a). (h) Combined mapping image of both Ce and Pt. The X-ray signals indicating the presence of fluorine and sulfur are from the Fumion® polyelectrolyte.

5.3.2 KOH Cyclic Voltammetry and Surface Area Determination

Figure 5.5 shows the CV in 0.1 M KOH for the platinum (Pt nanoparticles), Pt/Pt:CeO_{2-x} and Pt/CeO_{2-x} composite electrodes. The platinum surface of platinum nanoparticles electrode is higher than those of Pt/Pt:CeO_{2-x} and Pt/CeO_{2-x} electrodes. This is likely ascribed to the fact that the presence of ceria makes the GC surface less conductive. This caused difficulties in depositing platinum and resulted in fewer platinum nanoparticles that contribute to the total surface area.

Table 5.1 shows the Pt loading, the Pt weight percentage and the Pt surface area for the three different kinds of catalyst-deposited GC electrodes. The final platinum loadings on the electrodes were calculated by integrating the current–time curves used for the Pt electrodeposition with the Faraday law and accounting for the contributions of the 2 wt.% Pt content from the Pt:CeO_{2-x} nanorods. All dilution factors were taken into consideration in the calculations of the final Pt loadings on these evaluated electrodes. Among all three electrodes, the electrodes with only Pt nanoparticles have the highest Pt loading, wt.% of Pt and active surface area of Pt. Comparing the data for the two composite-catalyst coated electrodes with ceria nanorods, the additional contribution of Pt from decorated Pt on the ceria nanorods only increases 0.5 total wt.% of Pt in the final catalyst-composite.

5.3.3 Methanol Electrooxidation

Our cyclic voltammetry study indicates that the Pt/Pt:CeO_{2-x} catalyst consistently outperformed anode catalysts composed of similar “ink paste” than with pure CeO_{2-x} nanorods (Pt/CeO_{2-x}) or just platinum nanoparticle clusters towards the electrooxidation

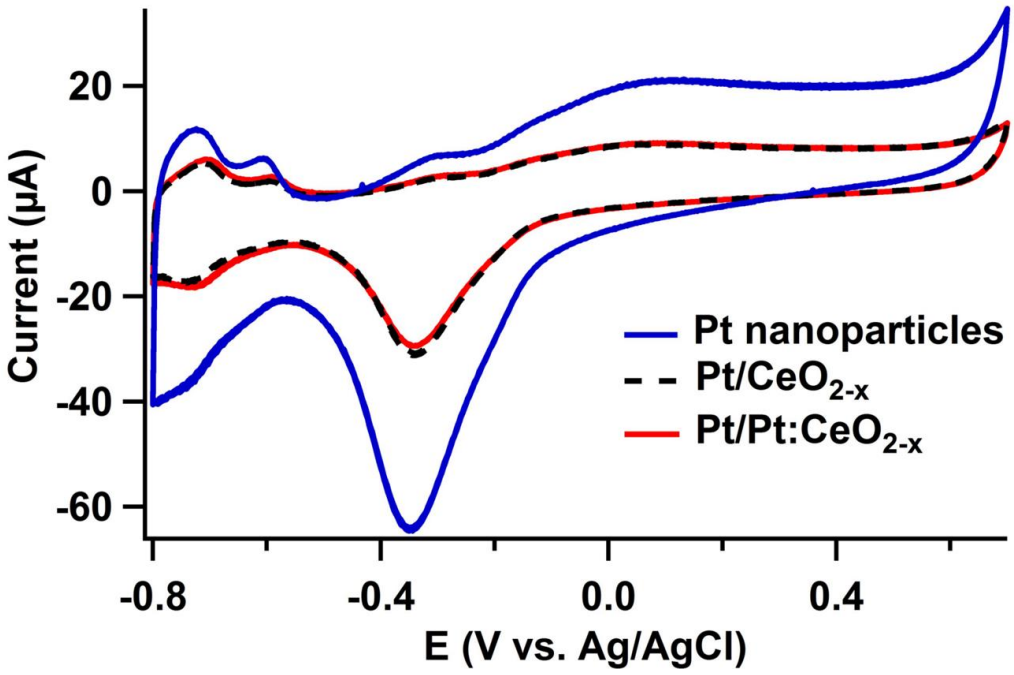

Figure 5.5 Cyclic Voltammetry at 100 mV/s in 0.1 M KOH for the final composite electrodes. Initial potential was -0.5 V vs. Ag/AgCl. Total number of cycles = 10. Note that the CV data of Pt/CeO_{2-x} coated electrodes (dotted line) almost overlaps that of the electrode coated with $Pt/Pt:CeO_{2-x}$ (black line).

Table 5.1 Platinum loadings, platinum percentage and platinum surface areas of three catalyst-coated glassy carbon working electrodes.

Catalysts	**Loading (µg of Pt)**	**Wt.% Pt**	**Surface Area (cm^2 of Pt)**
Pt/CeO_{2-x}	1.53	5.6	0.031
$Pt:Pt/CeO_{2-x}$	1.69	6.1	0.039
Pt only	2.31	8.2	0.095

of methanol. (Figure 5.6a) CVs of methanol oxidation using these three anode catalysts typically displayed a peak potential (E_p) at about 0.05 V vs. Ag/AgCl. The onset potential (E_s) for methanol oxidation is at -0.35 V vs. Ag/AgCl which is consistent with the Pt/ceria catalyzed methanol oxidation in literature.[18]

The maximum current densities of the three catalysts are 18.5 (Pt/Pt:CeO_{2-x}), 17.5 (Pt/CeO_{2-x}), and 11.5 mA/ cm^2 of Pt (Pt nanoparticle clusters), respectively. The order of these catalysts performances was consistent with three other trials of experiments. Xu et al [34] postulated that ceria support functions a similar bifunctional role as that of ruthenium (Ru) in Pt-Ru/C catalysts. Oxygen-rich species such as hydroxyls adsorbed on the ceria surface may transfer to the surface of Pt poisoned with adsorbed CO-like species, transform the CO species into gaseous CO_2, and free up more Pt surface catalytic sites for further alcohol electrooxidation. Figure 5.7a shows the LSVs of the methanol oxidation at 1 mV/s for the three composite electrodes. The idea of using this small sweep rate is to minimize the contribution of the double-layer current and maximize the contribution of faradic current. The electrode with Pt/Pt:CeO_{2-x} catalyst demonstrated the lowest onset potential, followed by Pt/CeO_{2-x} and platinum nanoparticles electrodes. This indicates that the Pt/Pt:CeO_{2-x} catalyst is the most catalytically active one towards methanol oxidation among the three evaluated catalysts.

Chronoamperometry responses from the Pt/Pt:CeO_{2-x}, Pt/CeO_{2-x}, and Pt nanoparticles catalysts were obtained to determine the stability of catalysts during the alcohol electrooxidation. Figure 5.6d shows that the obtained current densities for methanol oxidation were stable for at least 1800 s for the half-cell study with the

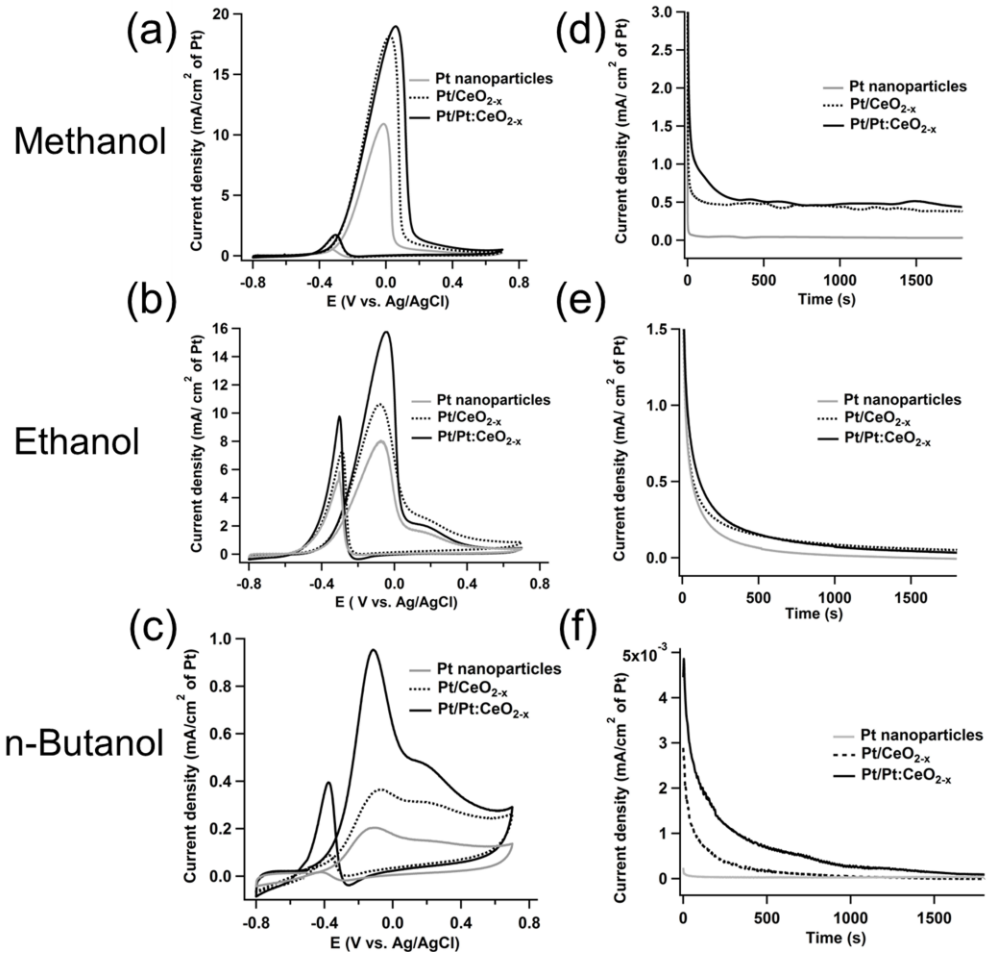

Figure 5.6 Electrochemical characterization of glassy carbon electrodes coated with platinum nanoparticles, platinum nanoparticles/CeO_{2-x} nanorods (Pt/CeO_{2-x}), or platinum nanoparticles/2 wt.% Pt:CeO_{2-x} nanorods (Pt/Pt:CeO_{2-x}) for the electrooxidation of methanol (a and d), ethanol (b and e) and n-butanol (c and f) in 0.1 M KOH at 100 mV/s. (a-c) Cyclic voltammograms; (d-f) chronoamperometric responses at a potential of -350 mV vs. Ag/AgCl.

Pt/Pt:CeO_{2-x} and Pt/CeO_{2-x} anode catalyst. However, the anode with Pt nanoparticle clusters yielded a shorter stable period and much lower current density, 0.02 mA/cm^2 of Pt compared with 0.5 mA/cm^2 obtained from the Pt/Pt:CeO_{2-x} and Pt/CeO_{2-x} anode catalysts. This is likely because Pt particles are more susceptible to the poisoning of CO by-product produced during the methanol electrooxidation. The better performance of the Pt/Pt:CeO_{2-x} and Pt/CeO_{2-x} catalysts in comparison to the Pt nanoparticles catalyst is attributed to the poisoning resistance of the composite catalysts. Likely, the ceria support functions similarly as ruthenium in the composite catalyst, which promotes the CO oxidation by providing oxygen-rich species to the Pt surface.[19]

5.3.4 Ethanol Electrooxidation

Ethanol is a popular bio-renewable alcohol-based fuel.[38] CVs of ethanol oxidation using these three anode-catalysts typically displayed two major oxidation peaks at -0.35 V and -0.08 V vs. Ag/AgCl. (Figure 5.6b) The current densities at -0.08 V are 7.8 mA/cm^2 for Pt nanoparticles, 10.2 mA/cm^2 for Pt/CeO_{2-x} and 15.5 mA/cm^2 for Pt/Pt:CeO_{2-x}, respectively. The Pt/Pt:CeO_{2-x} catalyst yielded almost two times higher current density than that of pure Pt nanoparticles coated anode. However, these current densities are smaller than the ones obtained for methanol. Figure 5.7b shows the LSV ethanol electrooxidation in 1 M ethanol/ 0.1M KOH solution at 1 mV/s. The onset potential decreases in this corresponding order: Pt nanoparticles > Pt:CeO_{2-x} > Pt/Pt:CeO_{2-x}. Again, the Pt/Pt:CeO_{2-x} composite is the most active catalyst in oxidizing ethanol thermodynamically among the three evaluated anode catalysts. Chronoamperometric responses for the ethanol system are shown in Figure 5.6e. The results are also consistent with the LSV data and the CV electrooxidation experiment.

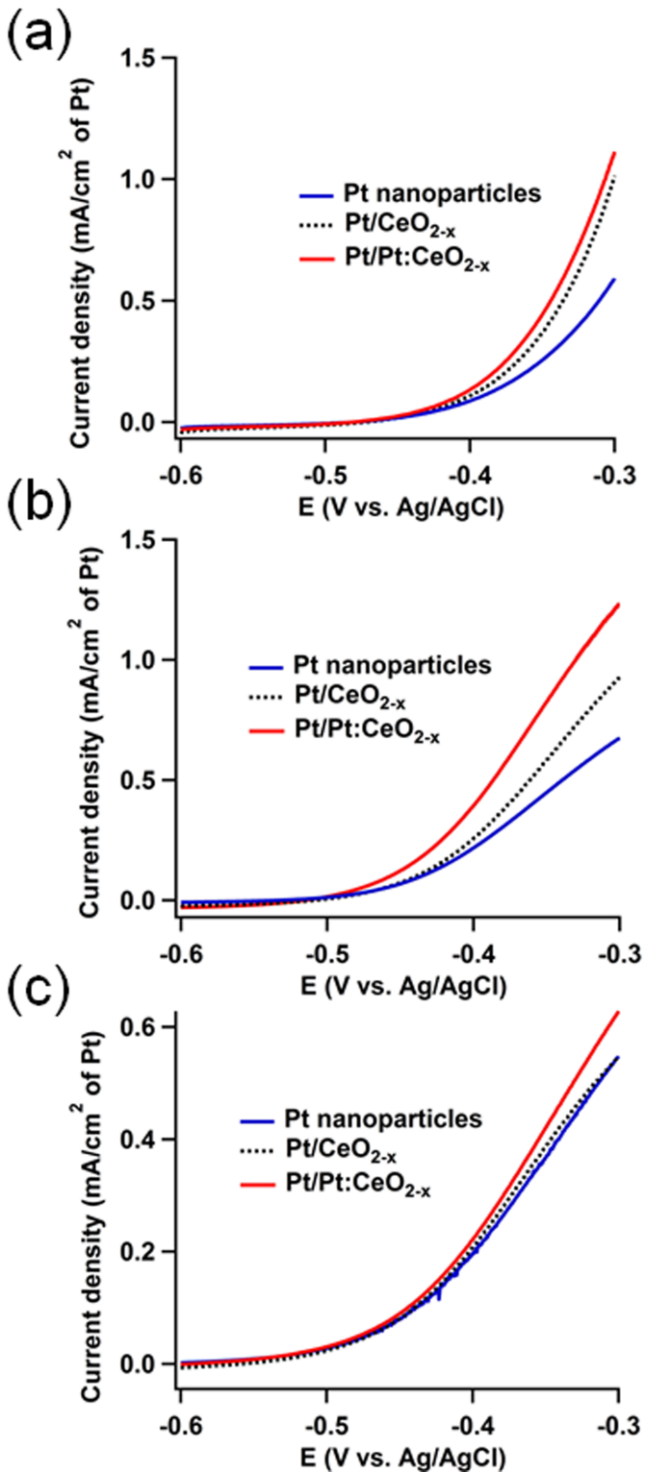

Figure 5.7 Onset potentials of alcohol electrooxidation for the Pt/Pt:CeO_{2-x}, Pt/CeO_{2-x} and Pt only electrode catalysts at 1 mV/s. (a) 1 M methanol/ 0.1M KOH, (b) 1 M ethanol/ 0.1 M KOH and (c) 1 M n-butanol/ 0.1 M KOH.

5.3.5 n-Butanol Electrooxidation

n-Butanol, though it has comparable energy density to petro fuel, has not been demonstrated as a viable fuel source because of the severe difficulty to fully electrochemically oxidize this chemical and extract the thermodynamically predicted energy content. All three catalyst systems showed about 10x smaller but noticeable current density in the half-cell study. The CVs of n-butanol oxidation using these three anode catalysts typically displayed three major oxidation peaks at -0.4 V, -0.05 V and 0.1 V vs. Ag/AgCl. (Figure 5.6c) The onset potential for the electrooxidation of n-butanol and the associated current density for Pt/Pt:CeO_{2-x} coated anodes are -530 mV vs. Ag/AgCl and 0.950 mA/cm^2, whereas those for Pt nanoparticle clusters anodes are -402 mV vs. Ag/AgCl and 0.203 mA/cm^2, respectively. The 100 mV difference between the two values of E_s for the anodic reaction is significant in DAFCs. The decrease of E_s with Pt/Pt:CeO_{2-x} coated anodes indicated that the activity for n-butanol oxidation was higher than the other two catalysts due to improved kinetics.[39] The chronoamperometric responses (Figure 5.6f) from these three catalyst-coated anodes yield very low current, suggesting the poor oxidative ability of n-butanol with these catalysts. However, the Pt/Pt:CeO_{2-x} coated anodes exhibit the slowest decay rate in current density, which implies the poisoning abating effect of Pt:CeO_{2-x} in this reaction. In the LSV data in 1 M n-butanol/ 0.1 M KOH solution, (Figure 5.7c) the electrode with Pt:Pt/CeO_{2-x} catalyst again demonstrated the lowest onset potential, and the trend is the same as those in methanol and ethanol solutions. This indicates that the Pt:Pt/CeO_{2-x} catalyst is the most catalytically active one towards n-butanol oxidation among the three evaluated catalysts.

5.3.6 Effect of Promoter Oxide Support on the Electrooxidation of Small Chain Alcohols

Among the three evaluated alcohol electrocatalysts, Pt/Pt:CeO_{2-x} exhibited higher catalytic performance than those of Pt nanoparticles and Pt/CeO_{2-x}. Interestingly, the relative enhancement in electrocatalytic activity for Pt/Pt:CeO_{2-x} for n-butanol oxidation is higher than those for methanol and ethanol electrooxidation when compared with Pt:CeO_{2-x} and pure Pt nanoparticles coated anodes. In methanol oxidation, the enhancement factors are 1.06 and 1.23 for Pt:CeO_{2-x} and pure Pt nanoparticles, respectively. In ethanol oxidation, the corresponding values are 1.52 and 1.99. In contrast, for n-butanol oxidation, the enhancement factors are 2.96 and 4.75.

The distinct improvements are likely due to the presence of 2 wt.% of Pt in the CeO_{2-x} nanorods, which might have enhanced the electrical conductivity of CeO_{2-x} nanorods Better conductive catalysts are expected to result in less resistance and thus more efficient electrooxidation. Doping the ceria with metal ions can increase the ionic conductivity.[40] In our case, from our XPS study, most of the Pt species in the 2 wt.% Pt decorated on the ceria nanorods are in the form of Pt^0 (36 %) and Pt-O-M (46 %) which corresponds to slightly ionized Pt. (as shown in Figure 5.2) The large percentage of Pt species in the Pt-O-M indicates strong interactions between Pt and the ceria support. Such strong interactions likely lead to changes in the electronic structure of the Pt:CeO_{2-x} and its crystal lattice distortion, which will affect the ionic conductivity of ceria.[41] According to previous studies, dopants are often reported to increase the electrical conductivity of ceria support and promote its use as anode materials.[42, 43] The considerable proportion of Pt species in the Pt^0 state on ceria surface also possibly provides another pathway to

enhance the conductivity of Pt:CeO_{2-x} catalyst during the electrochemical reaction. Hence, the catalyst with Pt decorated ceria deposited on the electrode (Pt/Pt:CeO_{2-x}) is likely more conductive and with smaller impedance for facilitating the current transfer from solution to the electrode. The ceria nanorods in the composite catalysts functioned to remove catalyst poisoning as well boosting the catalytic activity of Pt/Pt:CeO_{2-x} catalysts. Our results revealed that the catalytic activity of the "ink paste" composite catalyst can be increased significantly with only a small percentage (2 wt.%) Pt decorated on the ceria support.

5.3.7 CO Stripping Study

To evaluate the effect of Pt:CeO_{2-x} nanorods and ceria nanorods in mitigating the CO poisoning of the platinum nanoparticles electrodeposited on the anode catalyst coatings, linear sweep voltammetry was used to strip the CO from these platinum nanoparticles of the three evaluated anode catalysts after they were saturated with CO gas. Since CO is a common by-product of alcohol electrooxidation, it is expected that the catalysts with better performance in alcohol electrooxidation will require lower potential to strip the adsorbed CO. Figure 5.8 shows the CO stripping sweep voltammetry in alkaline medium (0.1 M KOH) for the prepared catalysts on the composite electrodes.

The CO stripping peak for the Pt nanoparticle clusters-coated anode takes place at a potential of -217 mV vs. Ag/AgCl, which is a higher value than the potential of -227 mV and -248 mV vs. Ag/AgCl for the Pt/CeO_{2-x} and Pt/Pt:CeO_{2-x} catalysts coated anodes, respectively. All CO was removed during the first scan. Only the first scans are shown

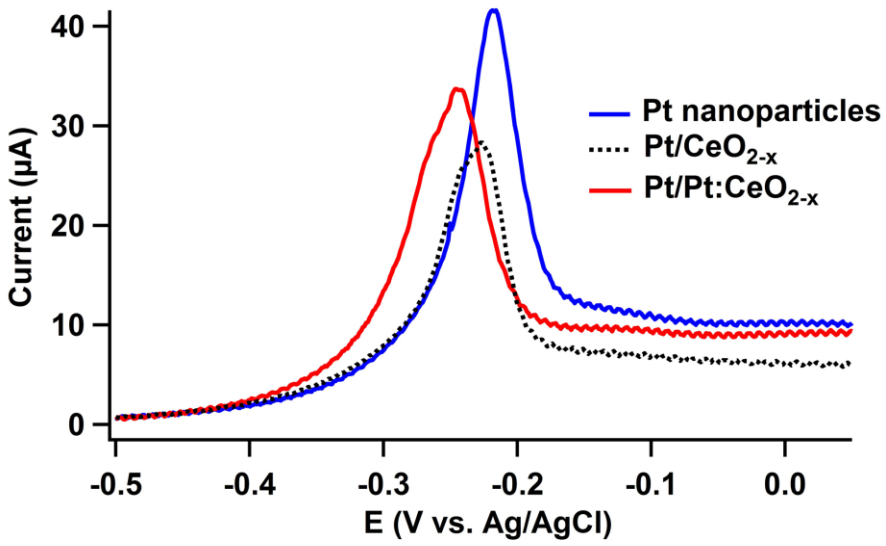

Figure 5.8 Variation of the potential of CO stripping with Pt/Pt:CeO_{2-x}, Pt/CeO_{2-x} and Pt only electrode catalysts in 0.1M KOH. All CO stripping data was recorded at 20 mV/s from -0.7 V to 0.7 V vs. Ag/AgCl.

since the major interest is the shift in stripping potentials. Our data suggests that it is thermodynamically more favorable to electrooxidize CO to CO_2 in the presence of ceria than solely platinum nanoparticle clusters on GC electrodes without ceria coating. Ceria can promote CO removal by oxidation with oxygen stored in ceria's lattice.[44] The ability of ceria to release oxygen assists the Pt:CeO_{2-x}catalysts in carrying out the oxidation of CO to CO_2 and removing the adsorbed CO.[28, 36, 45]

5.4 Conclusions

An "ink paste" electrocatalyst composed of Pt:CeO_{2-x} was prepared and confirmed that the composite catalysts generate higher electro-oxidation current densities than the only Pt electrodes towards alkaline electrooxidation of small chain molecular alcohols (methanol, ethanol and n-butanol). The catalytic activity can be attributed to the presence of active CeO_{2-x} support. CO stripping experiments showed that the desorption potential of CO depends on the composition of the composite electrode. The improvement in electrocatalytic responses of our catalyst for the oxidation of short-chained alcohols validates the critical use of high-activity oxidizing support with higher conductivity in designs of fuel cell anodes.

5.5 References

1 P. Waszczuk, J. Solla-Gullón, H. S. Kim, Y. Y. Tong, V. Montiel, A. Aldaz and A. Wieckowski, *J. Catal.*, 2001, **203**, 1-6.

2 Y. Ma, R. Wang, H. Wang and S. Ji, *Int. J. Electrochem. Sci.*, 2013, **8**, 6085 - 6093.

3 A. O. Neto, E. G. Franco, E. Aricó and M. Linardi, *Port. Electrochim. Acta*, 2004, **22**, 93-101.

4 C. Lamy, S. Rousseau, E. M. Belgsir, C. Coutanceau and J. M. Léger, *Electrochim. Acta*, 2004, **49**, 3901-3908.

5 S. Song, W. Zhou, Z. Zhou, L. Jiang, G. Sun, Q. Xin, V. Leontidis, S. Kontou and P. Tsiakaras, *Int. J. Hydrogen Energy*, 2005, **30**, 995-1001.

6 W. Zhou, *Appl. Catal. B*, 2003, **46**, 273-285.

7 N. Savage, *Nature*, 2011, **474**, S9-11.

8 A. Tabet-Aoul and M. Mohamedi, *Phys. Chem. Chem. Phys.*, 2012, **14**, 4463-4474.

9 J. Shim, C.-R. Lee, H.-K. Lee, J.-S. Lee and E. J. Cairns, *J. Power Sources*, 2001, **102**, 172-177.

10 O. A. Baturina, Y. Garsany, T. J. Zega, R. M. Stroud, T. Schull and K. E. Swider-Lyons, *J. Electrochem. Soc.*, 2008, **155**, B1314.

11 K. Sasaki, L. Zhang and R. R. Adzic, *Phys. Chem. Chem. Phys.*, 2008, **10**, 159-167.

12 M. A. Scibioh, S.-K. Kim, E. A. Cho, T.-H. Lim, S.-A. Hong and H. Y. Ha, *Appl. Catal. B*, 2008, **84**, 773-782.

13 X. Feng, Y. Shi and H. Zhou, *J. Rare Earth*, 2012, **30**, 29-33.

14 W. C. Chueh, Y. Hao, W. Jung and S. M. Haile, *Nat. Mater.*, 2012, **11**, 155-161.

15 M. A. Scibioh, S.-K. Kim, E. A. Cho, T.-H. Lim, S.-A. Hong and H. Y. Ha, *Appl. Catal. B*, 2008, **84**, 773-782.

16 Hariyanto, W. W. Purwanto, R. W. Seomantojo and U. Stimming, *J. Chem. Nat. Resour. Eng.*, 2007, **2**, 47-61.

17 H. B. Yu, J.-H. Kim, H.-I. Lee, M. A. Scibioh, J. Lee, J. Han, S. P. Yoon and H. Y. Ha, *J. Power Sources*, 2005, **140**, 59-65.

18 C. Xu and P. K. Shen, *Chem. Commun.*, 2004, 2238-2239.

19 C. Xu and P. K. Shen, *J. Power Sources*, 2005, **142**, 27-29.

20 S. Huang, C. Chang and C. Yeh, *J. Catal.*, 2006, **241**, 400-406.

21 Y. Zhou, C. L. Menendez, M. J. F. Guinel, E. C. Needels, I. Gonzalez-Gonzalez, D. L. Jackson, N. J. Lawrence, C. R. Cabrera and C. L. Cheung, *RSC Adv.*, 2014, **4**, 1270-1275.

22 C. L. Campos, C. Roldán, M. Aponte, Y. Ishikawa and C. R. Cabrera, *J. Electroanal. Chem.*, 2005, **581**, 206-215.

23 H. C. Yao and Y. F. Y. Yao, *J. Catal.*, 1984, **86**, 254-265.

24 V. Matolín, M. Cabala, I. Matolínová, M. Škoda, M. Václavů, K. C. Prince, T. Skála, T. Mori, H. Yoshikawa, Y. Yamashita, S. Ueda and K. Kobayashi, *Fuel Cells*, 2010, **10**, 139-144.

25 Y. H. Lin, X. L. Cui, C. H. Yen and C. M. Wai, *Langmuir*, 2005, **21**, 11474-11479.

26 A. Trovarelli, ed., *Catalysis by Ceria and Related Materials*, ICP, London, 2002.

27 J. Xu, J. Harmer, G. Li, T. Chapman, P. Collier, S. Longworth and S. C. Tsang, *Chem. Commun.*, 2010, **46**, 1887-1889.

28 N. J. Lawrence, J. R. Brewer, L. Wang, T.-S. Wu, J. M. Wells-Kingsbury, M. M. Ihrig, G. Wang, Y.-L. Soo, W.-N. Mei and C. L. Cheung, *Nano Lett.*, 2011, **11**, 2666-2671.

29 Y. J. Guan, D. A. J. M. Ligthart, O. Pirgon-Galin, J. A. Z. Pieterse, R. A. van Santen and E. J. M. Hensen, *Top. Catal.*, 2011, **54**, 424-438.

30 S. Chauhan, G. J. Richards, T. Mori, P. Yan, J. P. Hill, K. Ariga, J. Zou and J. Drennan, *J. Mater. Chem. A*, 2013, **1**, 6262-6270.

31 S. K. Meher and G. R. Rao, *ACS Catal.*, 2012, **2**, 2795-2809.

32 D. R. Ou, T. Mori, K. Fugane, H. Togasaki, F. Ye and J. Drennan, *J. Phys. Chem. C*, 2011, **115**, 19239-19245.

33 J. M. Anderson, J. Patel, A. S. Karakoti, N. Greeneltch, D. J. Díaz and S. Seal, *Electrochim. Acta*, 2011, **56**, 2541-2545.

34 C. Xu, R. Zeng, P. K. Shen and Z. Wei, *Electrochim. Acta*, 2005, **51**, 1031-1035.

35 A. Varez, E. Garcia-Gonzalez and J. Sanz, *J. Mater. Chem.*, 2006, **16**, 4249-4256.

36 Q. Fu, H. Saltsburg and M. Flytzani-Stephanopoulos, *Science*, 2003, **301**, 935-938.

37 K. Fugane, T. Mori, D. R. Ou, A. Suzuki, H. Yoshikawa, T. Masuda, K. Uosaki, Y. Yamashita, S. Ueda, K. Kobayashi, N. Okazaki, I. Matolinova and V. Matolin, *Electrochim. Acta*, 2011, **56**, 3874-3883.

38 J. P. W. Scharlemann and W. F. Laurance, *Science*, 2008, **319**, 43-44.

39 C. W. Xu, L. Q. Cheng, P. K. Shen and Y. L. Liu, *Electrochem. Commun.*, 2007, **9**, 997-1001.

40 M. Mogensen, N. M. Sammes and G. A. Tompsett, *Solid State Ionics*, 2000, **129**, 63-94.

41 H. Wang, A. Chroneos and U. Schwingenschlogl, *J. Chem. Phys.*, 2013, **138**.

42 S. R. Wang, T. Kobayashi, M. Dokiya and T. Hashimoto, *J. Electrochem. Soc.*, 2000, **147**, 3606-3609.

43 M. Burbano, D. Marrocchelli and G. W. Watson, *J. Electroceram.*, 2014, **32**, 28-36.

44 Q. He, S. Mukerjee, B. Shyam, D. Ramaker, S. Parres-Esclapez, M. J. Illan-Gomez and A. Bueno-Lopez, *J. Power Sources*, 2009, **193**, 408-415.

45 K. Scott, E. Yu, G. Vlachogiannopoulos, M. Shivare and N. Duteanu, *J. Power Sources*, 2008, **175**, 452-457.

CHAPTER 6

REACTIVE OXYGEN SPECIES GENERATION CATALYZED BY CERIUM OXIDE

6.1 Introduction

Reactive oxygen species (ROS) are powerful oxidants which can be generated in both biological systems and natural environments. In biological systems and cells, these species are generated either as specific chemicals for cell signaling pathways or as inevitable by-products of metabolism based on oxidation-reduction reactions.[1] Due to their high oxidizing power, ROS are major contributors to serious disease such as cancer, cardiovascular disease, brain dysfunction, inflammation and aging.[2, 3] This family of species typically includes (a) the hydroxyl radical ($HO^{\bullet}$) (b) the singlet oxygen ($^1O_2$, $1\Delta g$, first excited electronic state of molecular oxygen), (c) the superoxide anion radical ($O_2^{\bullet -}$) and (d) hydrogen peroxide (H_2O_2).[4] These oxygen species easily undergo inter-conversion between each other under physiological conditions; for examples, both $O_2^{\bullet -}$ and $HO^{\bullet}$ are the precursors of $^1O_2$.[5] The $HO^{\bullet}$ is a very reactive oxygen species that has a lifetime of about 2 nanoseconds in aqueous solution and a radius of diffusion of about 20 Å.[6] The lifetime of $^1O_2$ is considerably longer, 4.4 microseconds in aqueous solutions.[7] In contrast, the superoxide ion, $O_2^{\bullet -}$, which is not a strong oxidant comparatively, has a lifetime in the order of minutes under different pH conditions.

In the natural environment, ROS can be catalytically generated and decomposed with transition metal ions due to their ability to participate in oxidation-reduction properties. Their multiple valence states allow them to take part in radical reactions and act as electron donors and acceptors. The generation of ROS from H_2O_2 by metal ions capable of adopting multiple valence states is often reported to follow the mechanism of

Fenton, Fenton-like reactions, or through Haber-Weiss reaction. Though details of these proposed mechanisms are still under-debates, the hydroxyl radical is commonly accepted as being produced in H_2O_2-involving systems. Using iron (Fe) as an example, the chemical reaction is cited as:

$$Fe^{2+} + H_2O_2 \rightarrow Fe^{3+} + OH^- + HO^\bullet$$

The $HO^\bullet$ is a short-lived transient intermediate and highly reactive. It can further react with H_2O_2 and generate superoxide ion radical by the following reaction:

$$HO^\bullet + H_2O_2 \rightarrow O_2^{\bullet-} + H^+ + H_2O$$

The generated $O_2^{\bullet-}$ could generate the singlet oxygen through the well-known Haber-Weiss reaction

$$O_2^{\bullet-} + H_2O_2 \rightarrow {}^1O_2 + OH^- + HO^\bullet$$

Another pathway for ${}^1O_2$ production oxidation is:

$$HO^\bullet + O_2^{\bullet-} \rightarrow {}^1O_2 + OH^-$$

Minerals and transition metal oxides (for e.g. iron oxides) can also catalyze the H_2O_2 disproportionation to produce singlet oxygen and possible scavenger ROS radicals but the exact mechanism is yet unknown.[8] As an example, cerium oxide nanoparticles have been reported to suppress the ROS production, acting as an antioxidant in cells by scavenging free radicals.[9] Reactions involving redox cycles between Ce^{3+} and Ce^{4+} oxidation states are proposed to allow ceria to react catalytically with superoxide and hydrogen peroxide via Fenton-like chemistry, mimicking the behavior of two key antioxidant enzymes, superoxide dismutase and catalase, potentially abating all noxious intracellular ROS via a self-regenerating mechanism.[9]

However, in the H_2O_2 dismutation (or disproportionation) catalyzed by ceria, Ghibelli *et al* proposed another mechanism which involves concerted binding of H_2O_2 onto surface OVD sites of ceria without the generation of any hydroxyl radicals.[1] Nevertheless, our study of H_2O_2 dismutation with ceria catalyst suggests the generation of singlet oxygen during this reaction. Similar results have been reported that ceria mineral (CeO_2) could generate singlet oxygen with more than 10% yield, which can be rationalized based on the higher redox couple potential, 0.78 eV of $E°$ (CeO_2/ $Ce(OH)_3$).[8] Other studies have shown that nanomaterials of other metal oxides appear to generate ROS under other circumstances; however, the results are sometimes controversial, highly based on the synthetic methods, experimental conditions and solution chemistry (e.g. ionic strength, pH) in the reported literature. Experiment evidence implied that the catalytic and mimetic activity of ceria nanoparticles positively correlated with the Ce^{3+}/Ce^{4+} ratio; yet the molecular mechanism behind this catalysis is still unknown.[10]

The study of ROS, especially singlet oxygen, production and reactivity has emerged as a rich and diverse area with implications and applications in fields of ranging from polymer science to cancer therapy. In this chapter, we just present some preliminary studies of cerium oxides catalyzing the singlet oxygen generation through H_2O_2 disproportionation. Such knowledge will help to design research plans for further studies and provide some understandings of reaction mechanism of Fenton-like reaction using cerium oxide.

6.2 Experimental Methods

6.2.1 Synthesis of Cerium Oxide Catalysts

The ceria nanorods were synthesized by using a hydrothermal method modified from that reported by Lawrence *et al*.[11] A sample of 0.5 g of $Ce_2(SO_4)_3 \bullet xH_2O$ and 40 mL of 10 M NaOH were mixed and added to a 50-mL capacity Teflon-lined stainless steel autoclave. The chemicals in the autoclave were hydrothermally treated for 15 h. at 120 °C in a convection oven to generate cerium (III) hydroxide ($Ce(OH)_3$) nanorods. The product was filtered with a 3.0-μm pore size polycarbonate filter membrane (Millipore, Billerica, MA), rinsed with three aliquots of 50 mL water and placed in the convection oven for an initial oxidation at 50 °C for 2 h. During this oxidation process, most $Ce(OH)_3$ was converted to cerium oxide composed of both Ce_2O_3 and CeO_{2-x}. Subsequently, 25 mL of 30 % aqueous H_2O_2 was added to the mixture and sonicated for 30 min., followed by stirring for 30 min. to allow the reaction to reach completion. Then, the resulting catalyst was filtered with a 3.0-μm pore size polycarbonate membrane, rinsed with 50 ml of water and dried for 6 h. at 50 °C in a convection oven. Lastly, the synthesized material was activated at 400 °C in simulated air (20 % O_2, 80 % N_2) at 100 SCCM (standard cubic centimeter per minute) for 30 min. in a horizontal quartz tube annealing furnace with an operating pressure of 0.1 Torr.

6.2.2 Characterization of Cerium Oxide Catalysts

The morphology of the catalyst particles was investigated by Transmission Electron Microscopy (TEM). The catalyst powders were dispersed in methanol. 10 μL of the suspension mixture was sonicated for 5 sec. and loaded on holey carbon films supported on copper TEM grids. TEM micrographs were collected using a Hitachi H7500

transmission electron microscope (Hitachi High Technologies America, Inc., Pleasanton CA) operated at 100 kV. High resolution TEM (HRTEM) images were collected using a Tecnai G^2 F20 S-Twin 200 kV field-emission TEM (FEI Company, Hillsboro, OR). Images were analyzed with the Digital Micrograph^{TM} software.

6.2.3 Reactive Oxygen Species Generation Catalyzed by Cerium Oxide

Singlet oxygen green sensor (SOSG, Life Technologies) was used for detecting singlet oxygen in aqueous solutions, because the SOSG can react with $^1O_2$ and emit a green fluorescence under photo-irradiation. The SOSG stock solution was prepared using 330 μL degassed methanol to obtain 500 μM. 4.8456 g of Tris base (trishydroxymethyl aminomethane, $(OHCH_2)_3CNH_2$, J. T. Baker) was dissolved in 400 ml deionized water to prepare 0.1 M Tris buffer. The pH was adjusted to 7.5 using HCl. All the reactions were performed in Tris buffer solution in order to minimize the pH fluctuation.

The catalytic activity of ceria nanomaterials was evaluated through a Fenton-like reaction in dark environment. To prepare the reagents for this reaction, 20 mg ceria was added to 10 mL of 0.1 M Tris buffer solution (pH= 7.5) and stirred for 30 min to make 2 g/L ceria aqueous suspension. 2 mM of H_2O_2 stock solution was prepared in 0.1 M Tris buffer. These two stock solutions/ suspensions were applied to prepare different concentrations of H_2O_2 mixed with 1 g/L ceria. For example, 1.5 ml of 2 mM H_2O_2 stock solution was added to a 3.5 mL quartz Fluorimeter cell and mixed with 1.5 mL of 2 g/L ceria suspension. This resulted in 1 g/L ceria in 1 mM H_2O_2 solution. 30 μL of 500 μM SOSG was added as well into the cell and the resulting concentration was 5 μM. Seal the Fluorimeter cell and invert the Fluorimeter cell to mix the suspension well. Afterwards, the cell was placed in the sample mount of the Fluorimeter (Horiba Jobin Yvon,

FluoroMax-4) for singlet oxygen detection. The fluorimeter equipped with a 150 W ozone-free xenon arc-lamp, two Czerny-Turner monochromators for excitation and emission, and two detectors for signal and reference.

Before starting any real experiment, the fluorimeter needed to be checked and calibrated. Water was used for checking the xenon lamp and detectors. Fluorescence emission at 397 nm was measured upon excitation of 350 nm using 5 nm slit widths for both excitation and emission monochromators. The acquisition of fluorescence signals was 10 min for kinetic mode. For a typical $^1O_2$ fluorescence experiment, the spectra mode was used by selecting the "Emission" type, and the excitation wavelength was 488 nm. The slits for excitation and emission were 2 nm and 0.5 nm, respectively. The scanning wavelength started from 490 to 650 nm. The integration time is 0.1 s and the increment is 1 nm. As for a fluorescence experiment with kinetics mode, the wavelengths of excitation and emission light used were 488 nm and 530 nm respectively. The slit widths for excitation and emission are 2 nm and 0.5 nm. The time intervals for detecting photobleaching were 30 s, 60s and 120 s with a total scanning time of 10 min. The temperature remained at 20.8 °C through the reaction duration time and the sample was stirred constantly.

6.3 Results and Discussion

6.3.1 Cerium Oxide Enhances Singlet Oxygen $^1O_2$ Generation

A commonly used, commercial fluorescence dye named singlet oxygen sensor green (SOSG) was used as the chemical probe to detect $^1O_2$ generated in the reaction with model ceria catalysts and H_2O_2. 0.1 M Tris-HCl buffer (pH=7.5) has been used in similar reactions due to the relatively good stability of SOSG in this buffer. SOSG reacts with

$^1O_2$ to form an endoperoxide generated by the interaction of $^1O_2$ with the anthracene component of SOSG.[12] The resulting product emitted green fluorescence, with excitation and emission maxima at 488 and 530 nm. (See Scheme 6.1) Essential control experiments included: (1) buffer + SOSG, (2) H_2O_2 solution + SOSG and (3) buffer + catalyst + SOSG. The control experiments of (1) and (3) did not demonstrate significant amount generation of $^1O_2$ compared to the (2) control experiment with H_2O_2. The reason is that small amount of reactive oxygen species, such as $OH^{\bullet}$, O^{2-} and $^1O_2$, can be generated during H_2O_2 degradation in a slow rate without catalysts. Therefore, the (2) control experiment show much higher fluorescence signal than the other two control experiments. With cerium oxide catalysts, the production of $^1O_2$ is enhanced twice compared to its control experiment (2) without ceria catalysts. (See Figure 6.1) This clearly indicates that cerium oxide exhibits reactive oxygen species production in the presence of H_2O_2. Similar results have been observed by Aubry, in which 0.02 M cerium oxide (CeO_2) mineral was shown to produce $^1O_2$ in the decomposition of 0.1 mM H_2O_2 using a water soluable rubrene derivative trapping agent.[8]

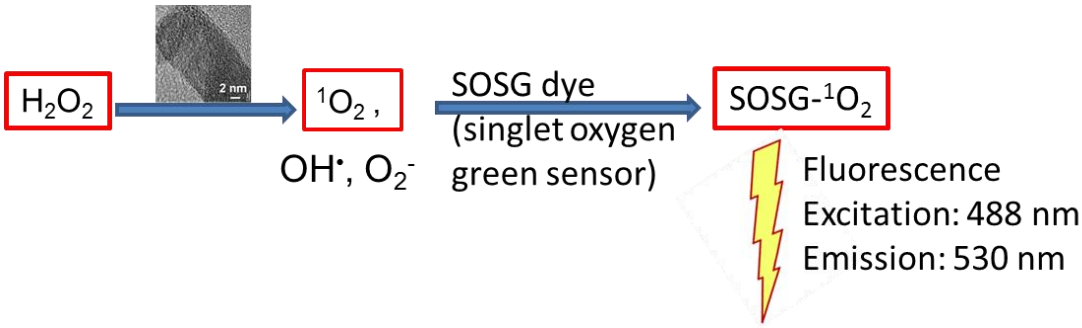

Scheme 6.1 Applying chemical trap SOSG for singlet oxygen detection generation from H_2O_2 solution with ceria nanorods as catalyst.

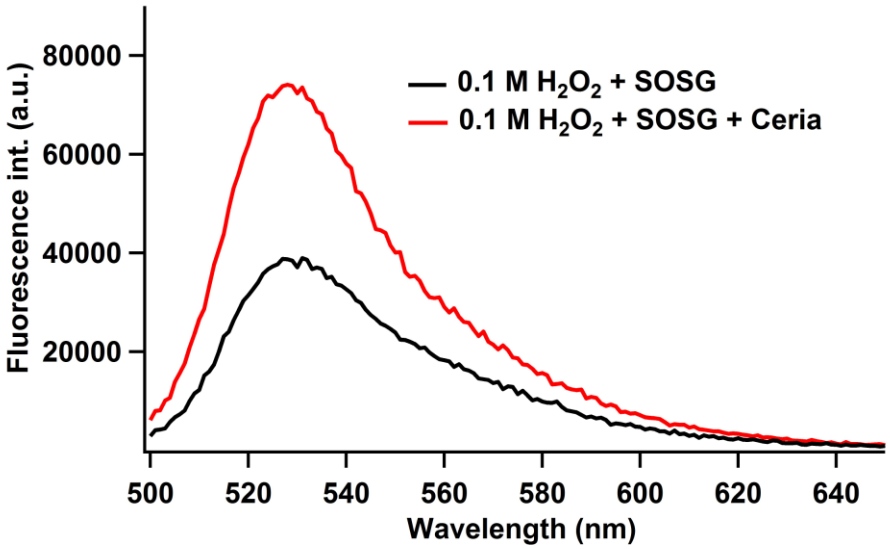

Figure 6.1 Singlet oxygen generation at room temperature with ceria nanorod catalysts compared to its control experiment in 0.1 M H_2O_2/0.1 M Tris buffer, pH = 7.5

6.3.2 Photobleaching Effect on $^1O_2$ Generation Catalyzed by Cerium Oxide

The data collection time interval has been assessed in our study to evaluate the photobleaching effect of singlet oxygen sensor SOSG. Photobleaching is a phenomenon that the fluorophore is permanently unable to fluoresce, which is caused by photon-induced chemical damage or covalent modification.[13] The endoperoxide generated by $^1O_2$ and SOSG exhibits photobleaching. The green fluorescence fades away under photo-irradiation as a consequence of SOSG photobleaching mediated by radical species. The $^1O_2$ generation kinetics with respect to different time intervals of 30 s, 60 s and 120 s have been investigated in 0.2 and 0.3 mM H_2O_2 mixed with 1 g/L ceria suspension. The apparent reaction rate has been evaluated approximately from the linear fitting of $^1O_2$ generation kinetics curve (Fluorescence signal change as a function of time). (See Figure 6.2 for example) The apparent reaction rates of 0.2 and 0.3 mM H_2O_2 disproportionation with different time intervals were listed in Table 6.1. We observe that longer time interval yields higher reaction rate in both solutions. The reaction system with 120 s data collection interval shows highest $^1O_2$ generation in 0.2 mM H_2O_2 solution. The reaction rate differences of the systems with time intervals between 30 and 60 s, and between 60 and 120 s are 14% and 12 %, respectively. Fluctuations occur in all three $^1O_2$ generation reactions indicated by the significant standard deviations. Therefore, the photobleaching effect is significant under 0.2 mM H_2O_2 solution with 1 g/L ceria nanorods. However, the photobleaching phenomenon is different in 0.3 mM H_2O_2 solution. The time interval parameter of 30 and 60 s still affects the $^1O_2$ generation rate, but not as dramatic compared to that in 0.2 mM H_2O_2 solution. The reaction rates of $^1O_2$ generation are close to each other under these two conditions, with difference less than 10%. The signal

fluctuation is also much less significant compared to the 0.2 mM H_2O_2 solution, which is clearly suggested from the smaller standard deviations. These results imply that the photobleaching effect is relatively smaller at higher concentration of H_2O_2 solutions due to their higher production of $^1O_2$. At low concentrations of H_2O_2 solutions, the photobleaching should be taken into account by use of this dye for the design of appropriate operation procedures. The SOSG photobleaching phenomenon has also been reported by Ragas *et al*. for their singlet oxygen photosensitization reaction.[14]

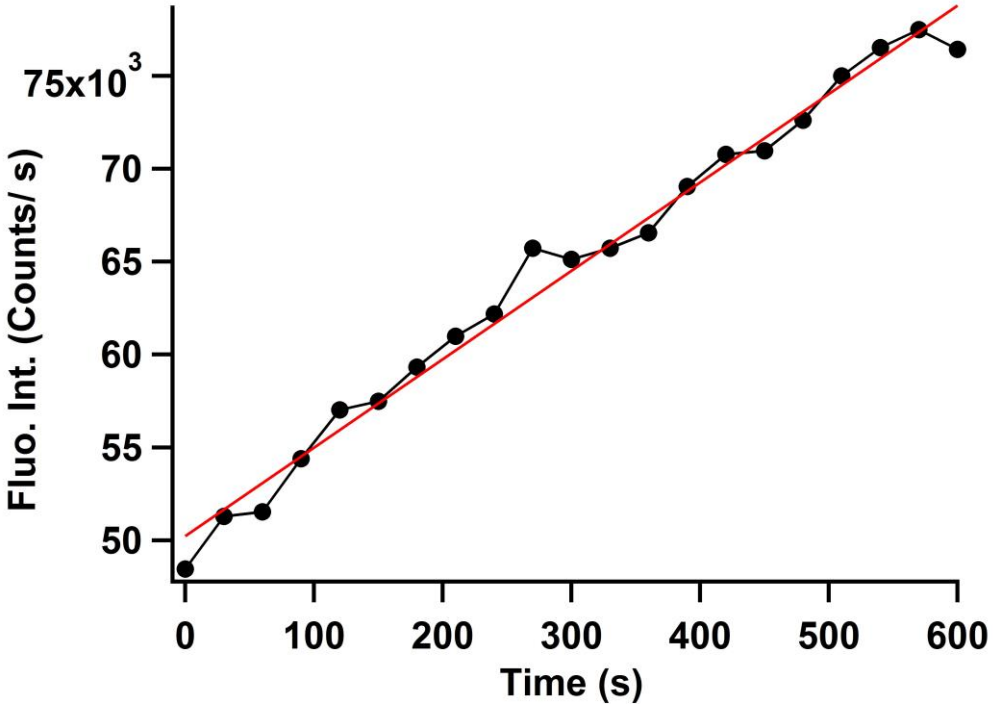

Figure 6.2 Plot of $^1O_2$ generation in 0.3 mM H_2O_2 catalyzed by 1 g/L ceria nanorods in 0.1 M Tris buffer solution as a function of time. The fitted straight line is the approximate apparent reaction rate.

Table 6.1 Approximate $^1O_2$ generation rate evaluation from ceria nanorods catalyzing H_2O_2 decomposition with concentrations of 0.2 and 0.3 mM.

Time interval	Reaction rate (Counts/s^2)	
	0.2 mM	0.3 mM
30	19.7 ± 1.0	47.6 ± 1.3
60	22.5 ± 1.6	52.2 ± 1.7
120	25.3 ± 2.7	

6.3.2 Kinetic Study of $^1O_2$ Generation as A Function of H_2O_2 Concentration

The time profile of the fluorescence intensity for SOSG in the presence of H_2O_2 and 1 g/L ceria nanorods is shown in Figure 6.3. The fluorescence intensity increases with the H_2O_2 concentration increasing, which indicates the $^1O_2$ generation is positively correlated to the H_2O_2 concentration from 0.1 to 1.0 mM. The increasing slopes of all those curves have been evaluated as a descriptor for apparent reaction rate. From 0.1 to 0.3 mM H_2O_2, all data collected in 10 min reaction duration have been used for reaction rate determination. However, only the first 5 data points have been used to obtain the apparent reaction rate from 0.4 to 1.0 mM due to the non-linear relationship in each data set. The fluorescence intensity increases faster in the first 200s and slows down afterwards. The values of slopes with standard deviations obtained from data fitting have been plotted out in Figure 6.4. The apparent reaction rate rises gradually from 0.1 to 0.2 mM H_2O_2, and then demonstrates dramatic increase from 0.2 to 0.6 mM H_2O_2. In the H_2O_2 solutions from 0.6 to 1.0 mM, the apparent reaction rate slows down the increasing rate and only shows 30% increasement in this range.

The reaction order has been determined by reaction rate law. Assume 1 g/L ceria nanorods were in excess in all these concentrations of H_2O_2 solution. Thus the reaction rate can be expressed in the following equation:

$$\text{Rate} = A\,[H_2O_2]^x$$

A is proportional to the reaction rate constant, and x is the reaction order of H_2O_2.The reaction order can be obtained by doing logarithmic operation on both sides, which is showed in the following equation:

$$\text{Log (Rate)} = \text{Log (A)} + x\ \text{Log}\,[H_2O_2]$$

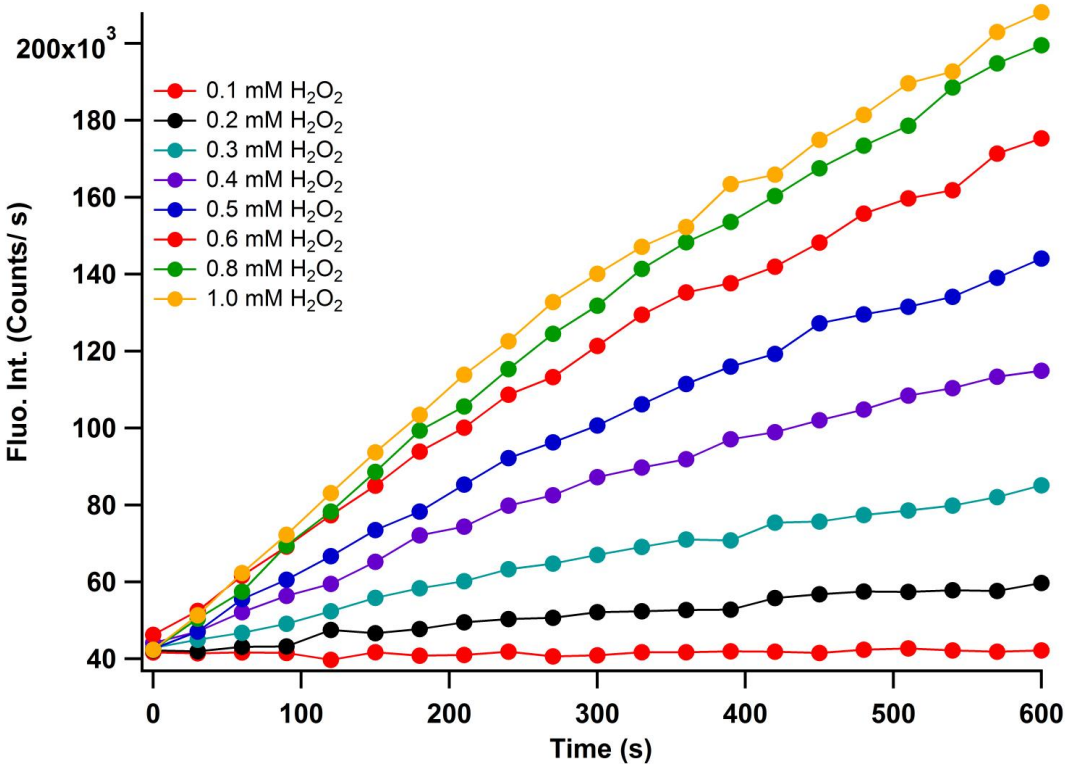

Figure 6.3 Kinetics of $^1O_2$ generation in different H_2O_2 solutions from 0.1 to 1 mM as a function of time

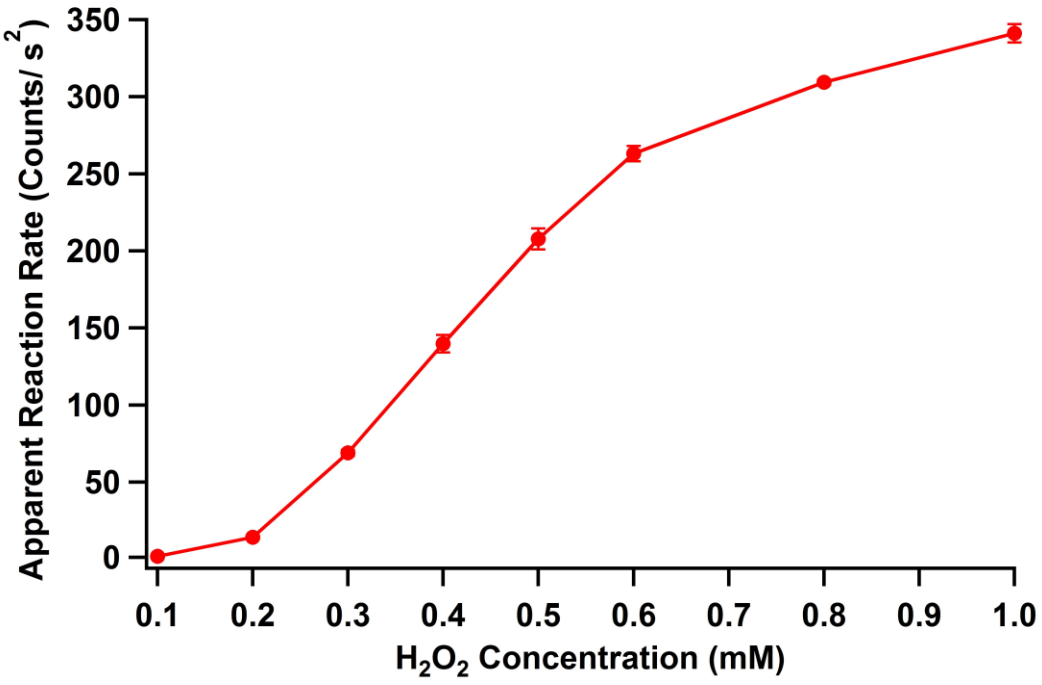

Figure 6.4 $^1O_2$ generation apparent reaction rate as a function of H_2O_2 concentration from 0.1 to 1 mM.

Figure 6.5 shows the logarithmic scale of apparent reaction rate as a function of H_2O_2 concentration. The slope value obtained from data fitting is 3.16 indicating the reaction order is 3 approximately in H_2O_2 solutions with concentrations from 0.1 to 0.4 mM. At higher concentrations of H_2O_2 solutions from 0.6 mM to 1.0 mM, the reaction rate reaches to a plateau. This result indicates that H_2O_2 is not the rate limiting reagent in these reactions. We hypothesize that the active site of ceria nanorods might be fully occupied with 0.6 mM H_2O_2 molecules, hence increasing H_2O_2 concentration would not significantly affect the reaction rate. As a result, the assumption of ceria in excess is not reliable under these conditions. The $^1O_2$ generation mechanism at higher concentration of H_2O_2 solutions with 1 g/L ceria catalysts is different from that in low concentrations of H_2O_2 solutions. In order to determine the reaction order of $^1O_2$ generation with respect to H_2O_2 at high concentrations, new experimental design is required including the concentration of both SOSG and ceria catalyst, and more efforts are needed to study this complex reaction system.

6.4 Conclusions

Ceria nanorods exhibit catalytic activity towards H_2O_2 decomposition to generate $^1O_2$. Singlet oxygen green sensor (SOSG) is a chemical trapping agent for $^1O_2$, and has been successfully applied to monitor the $^1O_2$ change during reaction. However, the $^1O_2$ mediated SOSG can lose its green fluorescence ability due to photobleaching caused by photo- irradiation. This needs to be taken into account when employing this singlet oxygen sensor in reaction systems.

The amount of $^1O_2$ generated increases as a consequence of increasing H_2O_2 concentration from 0.1 mM to 1.0 mM. The generation rate improves dramatically in the

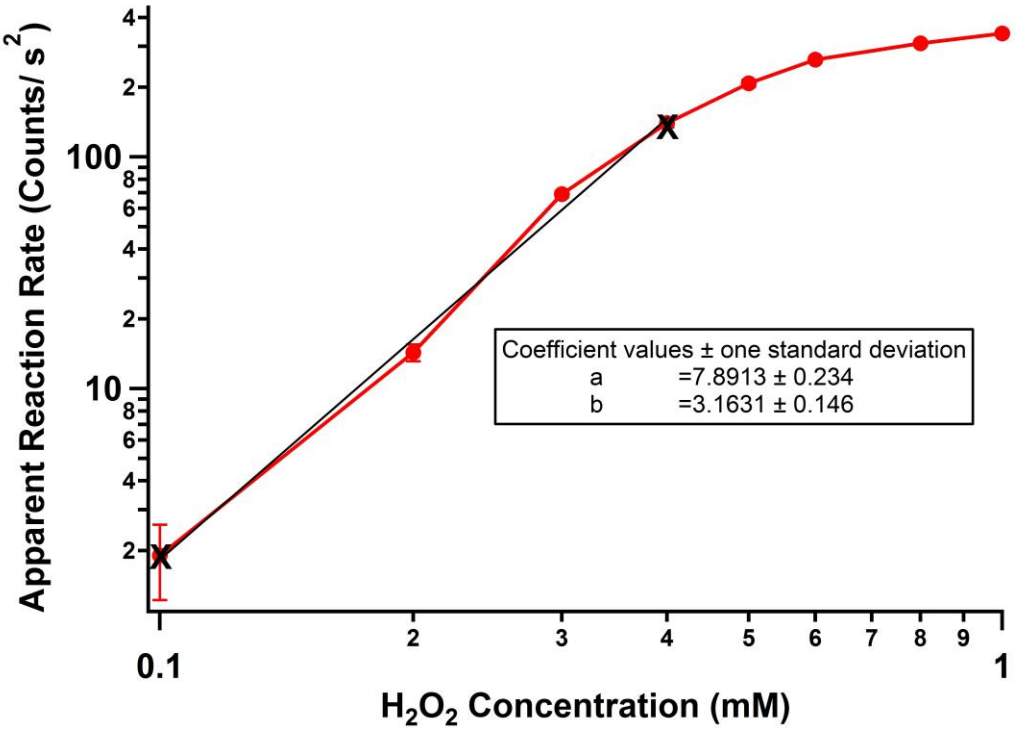

Figure 6.5 Log_{10}-Log_{10} plot of reaction rate vs. H_2O_2 concentration to determine the reaction order

H_2O_2 solution from 0.2 to 0.6 mM and slowly increases from 0.6 to 1.0 mM. The reaction order with respect to H_2O_2 is 3 in H_2O_2 solutions with concentration from 0.1 to 0.4 mM. At higher concentration of H_2O_2 solution *ca* 0.6-1.0 mM, the apparent reaction rate reaches to a plateau, indicating the H_2O_2 molecules almost occupying the active sites completely of ceria nanorods with a concentration of 1 g/L.

6.5 References

1 I. Celardo, J. Z. Pedersen, E. Traversa and L. Ghibelli, *Nanoscale*, 2011, **3**, 1411-1420.

2 T. Lu and T. Finkel, *Exp. Cell. Res.*, 2008, **314**, 1918-1922.

3 M. Valko, M. Izakovic, M. Mazur, C. J. Rhodes and J. Telser, *Mol. Cell Biochem.*, 2004, **266**, 37-56.

4 E. L. Clennan and A. Pace, *Tetrahedron*, 2005, **61**, 6665-6691.

5 I. Kruk, ed., *Envionmental toxicology and chemistry of oxygen species*, Springer, 1998.

6 P. Wardman, *Free Radical Bio. Med.*, 2007, **43**, 995-1022.

7 M. A. J. Rodgers and P. T. Snowden, *J. Am. Chem. Soc.*, 1982, **104**, 5541-5543.

8 J. M. Aubry, *J. Am. Chem. Soc.*, 1985, **107**, 5844-5849.

9 S. M. Hirst, A. S. Karakoti, R. D. Tyler, N. Sriranganathan, S. Seal and C. M. Reilly, *Small*, 2009, **5**, 2848-2856.

10 C. Korsvik, S. Patil, S. Seal and W. T. Self, *Chem. Commun.*, 2007, 1056-1058.

11 N. J. Lawrence, J. R. Brewer, L. Wang, T. S. Wu, J. Wells-Kingsbury, M. M. Ihrig, G. H. Wang, Y. L. Soo, W. N. Mei and C. L. Cheung, *Nano Lett.*, 2011, **11**, 2666-2671.

12 A. Gollmer, J. Arnbjerg, F. H. Blaikie, B. W. Pedersen, T. Breitenbach, K. Daasbjerg, M. Glasius and P. R. Ogilby, *Photochem. Photobiol.*, 2011, **87**, 671-679.

13 http://micro.magnet.fsu.edu/primer/java/fluorescence/photobleaching/.

14 X. Ragas, A. Jimenez-Banzo, D. Sanchez-Garcia, X. Batllori and S. Nonell, *Chem. Commun.*, 2009, 2920-2922.

CHAPTER 7

SUMMARY AND FUTURE STUDIES

7.1 Summary

This dissertation presents the details of nanostructure cerium oxide catalysts including their synthesis, structure characterization and their applications in different reactions. The catalytic activities and reaction mechanism were evaluated and proposed for principle understanding in order to design catalysts with improved performances.

Chapter 1 introduces the background information of cerium oxide, such as its abundance and distribution, structure, morphology and oxygen vacancy defects. Three common synthesis methods of metal oxides are discussed, as well as the characterization techniques and cerium oxide applications in various areas. Additionally, the structure and physicochemical properties of cerium oxide are also discussed in these applications because of their important roles in influencing materials' performances.

Chapter 2 describes the catalytic system of cerium oxide supported palladium particles for carbon monoxide oxidation. It illustrates the structure changes of palladium particles during the redox cycle which helps to elucidate self-regeneration mechanism of the catalyst system. The catalysts demonstrate 75% decreased catalytic activity after 24 h reaction with carbon monoxide. The activity can be regenerated and restored almost 100% of their original catalytic activity by exposing them to ambient conditions for 24 h. X-ray spectroscopy studies of the atomic structures and oxidation states of palladium in the catalyst find that the formation of disordered palladium oxide is partly accountable for its observed regenerative catalytic property.[1]

Chapter 3 presents another cerium oxide supported noble metal system. The supported gold clusters exhibits d holes through the X-ray absorption spectroscopic study. The resonance photoemission spectroscopy proves the existence of *s-d* hybridization in the supported gold clusters through O 2*p* band due to the strong metal support interaction. Density function theory (DFT) is also applied to simulate two different systems of gold clusters supported on cerium oxide. Same conclusion of *s-d* hybridization in gold clusters is observed in both gold/ cerium oxide systems. Gold *5d* band upward shift from DFT study is proposed to enhance gold/ceria activity towards O_2 involved reactions.

Chapter 4 and Chapter 5 discuss the application of cerium oxide catalysts in direct alcohol fuel cell. Electrocatalysts composed of cerium oxide and platinum are synthesized and evaluated towards short carbon chain alcohols including methanol, ethanol, and n-butanol electrooxidation. The morphology of cerium oxide support influences its catalytic activity towards methanol electrooxidation in alkaline media. X-ray photoelectron spectroscopic data indicates that platinum (Pt) nanoparticles deposited onto ceria nanorods are disproportionally composed of oxidized species rather than metallic Pt while Pt nanoparticles on ceria nanoparticles mainly consisted of metallic Pt. Stronger metal-support interactions between Pt particles and ceria nanorods are postulated to induce preferential oxidation of Pt and consequently decreased the catalytic sites and overall activity.[2] Multi-functional anode catalysts composed of platinum nanoparticles electrodeposited on 2 wt% Pt decorated ceria nanorod supports are shown to enhance the alkaline electrocatalytic oxidation of methanol, ethanol and n-butanol over electrodeposited Pt nanoparticles alone or ones supported with pure ceria nanorods. The Pt/cerium oxide nanorod support is demonstrated to increase the current density of the

investigated electrooxidation of methanol, ethanol and n-butanol by more than 30% over the other two catalysts.[3]

Chapter 6 extends the application of cerium oxide in liquid/ solid phase reaction system. Cerium oxide is shown to enhance the singlet oxygen ($^1O_2$) generation through catalyzing H_2O_2 decomposition. Chemical trap reagent, singlet oxygen green sensor (SOSG), is used to detect $^1O_2$ through fluorescence experiment. The photobleaching effect of SOSG mediated by $^1O_2$ has been observed and it affects the reaction rate obtained at low concentrations of H_2O_2 solutions. Reaction kinetics through 0.1 to 1.0 mM H_2O_2 has also been investigated to determine the reaction order with respect to H_2O_2.

7.2 Future Studies

The study of reactive oxygen species generation using cerium oxide as the catalyst isn't sufficient in Chapter 6. However, the obtained results renew our understanding in this catalytic reaction system, and inspire us to make more effort to elucidate the essential principles. In the future, we will investigate the effect of oxygen vacancy defects, facet and dopants in catalyzing $^1O_2$ generation, and detect other active species such as $OH^{\bullet}$ and $O^{2-\bullet}$ probably generated during the reaction.

7.2.1 Effect of Oxygen Vacancy Defects in Cerium Oxide on $^1O_2$ Generation

Cerium oxide's unique catalytic activity to promote redox reactions stems from its large intrinsic oxygen storage and release capacity associated with oxygen vacancy defects (OVDs) formation and density, as well as low potential redox transformation between Ce^{3+} and Ce^{4+}.[4, 5] Diverse types of surface OVDs observed under scanning tunneling microscopy include single surface and subsurface vacancy defect, triangular vacancy defect and linear vacancy defect.[4] The surface OVDs induced Ce^{3+} ions on ceria

have been postulated as potent surface sites for catalysis, because adsorbed gases or reaction intermediates could interact simultaneously with the exposed coordinatively unsaturated Ce^{3+} ions.[6, 7] They are crucial in contributing Lewis acid–base properties as well as the redox surface properties and are strongly correlated to their Ce^{3+}/Ce^{4+} ratios for various reactions.

Cerium oxides with different densities and shapes of OVDs will be synthesized to investigate the OVDs effect in $^1O_2$ generation. Recently, we demonstrated a conceptually different approach to increase the OVD density and Ce^{3+} concentration using a low-pressure thermal activation.[5] (Figure 1.7) Extended X-ray absorption fine structure spectroscopy (XAFS) study on these ceria nanorods revealed the decrease of both the coordination number (6.3) and radial distance of Ce-O (2.294 Å) in the first shell when compared with the theoretical values. This indicates fewer interatomic bonds between Ce and O, thus suggesting a higher density of OVDs in ceria nanorods. X-ray photoemission data also indicates that the ceria nanorods activated under 0.1 Torr possess higher surface Ce3+ than non-activated one, 39% vs. 19%.

In-situ X-ray absorption spectroscopy will be applied to investigate the cerium oxide structure modification under reaction with H_2O_2. The newly formed surface species on ceria, coordination number, bond length and disorder will be elucidated during the reaction. Ce^{3+} concentration in the bulk will also be monitored through X-ray near edge spectroscopy (XANES). Because it will help to provide clues for the reaction mechanism, at least demonstrates whether cerium oxide will be oxidized or reduced during this Fenton-like reaction.

7.2.2 Effect of Cerium Oxide Facets in $^1O_2$ Generation

We will synthesize different faceted ceria nanostructures (nanocubes, nano-octahedron, nanorods) with different size-distribution and categorized the populations of surface defects and Frenkel-type defects by developed hydrothermal methods.[8, 9] Cerium (III) nitrate ($Ce(NO_3)_3$), NaOH and Na_3PO_4 will be used for ceria synthesis with different shapes. To obtain the desirable shapes of nanoceria, temperature, concentration of reagents and reaction time need to be well controlled. For example, to obtain nanorods, 0.11mM of $Ce(NO_3)_3$ and 1.1M NaOH will be used while 0.35M $Ce(NO_3)_3$ is required to synthesize nanocubes. Materials including nanorods, nanocubes, nano-octahedron with exposed well-defined (111)/(110), (100) and (111) planes, respectively will be our synthesis targets. (See Figure 7.1) These different facets are considered because they can represent various types, densities and formation energies of OVDs which are crucial for studying the defects chemistry in chemical reactions.

The catalytic activity and kinetics relationship to the catalytic sites for generation of $^1O_2$ with H_2O_2 will be determined using fluorescence and spin-probe studies for providing a credible method to identify the reaction pathways. Adsorption energetics of potential reaction substrates onto optimized slabs and faceted particle models with different types of surface defects (point, cluster and linear defects), sizes and concentration of Frenkel-type defects will be calculated using density functional theory and correlated to the energetics of the surface defect dipole-dipole interactions. The results will be used to deduce possible reaction pathways and phenomenological models. Control experiments will be performed to eliminate possible influence of side reactions.

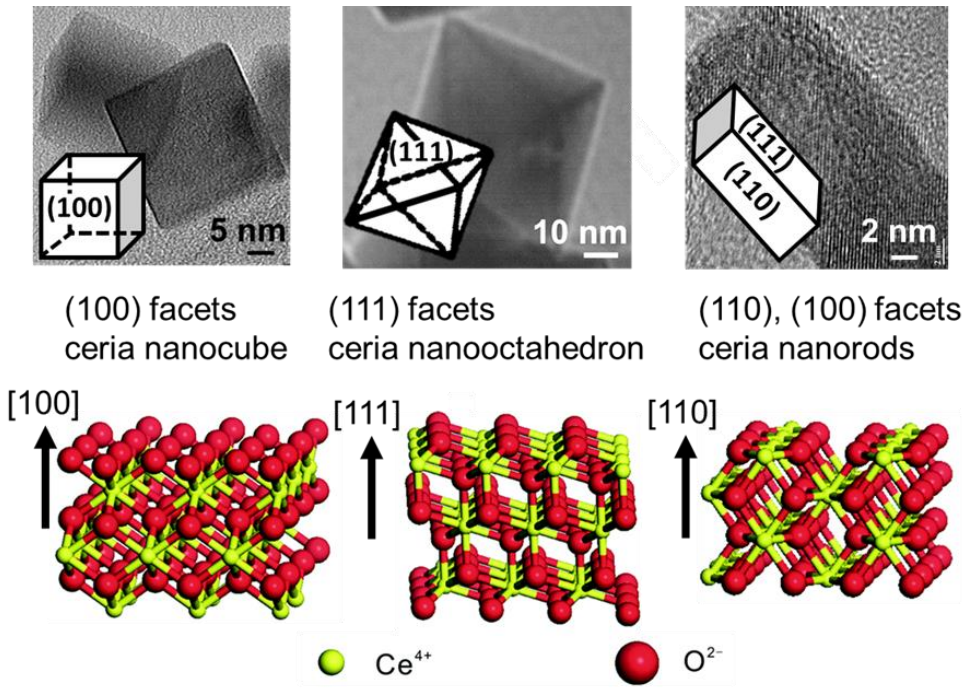

Figure 7.1 TEM images of ceria nanocubes exposing (100) facets, ceria nano-octahedra with (111) facets and ceria nanorods with (111) and (110) facets. The bottom pictures showing the surface structure of (100), (111) and (110) facets.[10]

7.2.3 Effect of Metal Dopants in Cerium Oxide on $^1O_2$ Generation

Foreign metal ions (or dopants; for e.g. Zr, lanthanide ions) which are known to form solid solution with ceria are can increase/decrease the energetics of lattice oxygen mobility, increase/eliminate internal and possibly subsurface defects such as Frenkel-type defects[11, 12] and change the lattice parameters.[13] We will introduce metal dopants into the lattices of ceria nanostructures developed previously. The changes in the lattice parameters and the population of different categorized surface defect types and subsurface Frenkel-type defects will be measured and correlated to the catalytic activity and kinetics of generation of ROS with H_2O_2 under optimized reaction conditions. Molecular adsorption energies on the modeled system with these OVDs, subsurface defects and the surface defect dipole-dipole interaction energy will be calculated and compared with the experimental results. Descriptors such as metal ion lattice (association) energies and lattice parameters will be examined as predictors for catalytic activity.

The chemical synthesis process developed in Cheung's lab will provide the basis for preparing different faceted ceria of well-defined size and morphology, OVDs densities and different foreign dopant levels. We will couple both atomic structure study using x-ray absorption fine structure (XAFS) and microscopy and effort in computational group on theoretical modeling to yield meaningful active site descriptions and to deduce the reaction pathways in the ceria-catalyzed ROS generation. This synergetic approach is expected to provide understanding of how defect chemistry influences material structure-catalytic activity relationship in nanostructured ceria.

7.3 References

1 Y. Y. Zhou, N. J. Lawrence, T. S. Wu, J. Liu, P. Kent, Y. L. Soo and C. L. Cheung, *ChemCatChem*, 2014, **6**, 2937-2946.

2 Y. Y. Zhou, C. L. Menendez, M. J. F. Guinel, E. C. Needels, I. Gonzalez-Gonzalez, D. L. Jackson, N. J. Lawrence, C. R. Cabrera and C. L. Cheung, *RSC Adv.*, 2014, **4**, 1270-1275.

3 C. L. Menendez, Y. Y. Zhou, C. M. Marin, N. J. Lawrence, E. B. Coughlin, C. L. Cheung and C. R. Cabrera, *RSC Adv.*, 2014, **4**, 33489-33496.

4 F. Esch, S. Fabris, L. Zhou, T. Montini, C. Africh, P. Fornasiero, G. Comelli and R. Rosei, *Science*, 2005, **309**, 752-755.

5 N. J. Lawrence, J. R. Brewer, L. Wang, T. S. Wu, J. Wells-Kingsbury, M. M. Ihrig, G. H. Wang, Y. L. Soo, W. N. Mei and C. L. Cheung, *Nano Lett.*, 2011, **11**, 2666-2671.

6 G. Wang, L. Wang, X. Fei, Y. Zhou, R. F. Sabirianov, W. N. Mei and C. L. Cheung, *Catal. Sci. Technol.*, 2013.

7 G. Lu, A. Linsebigler and J. T. Yates, *J. Phys. Chem.*, 1995, **99**, 7626-7631.

8 Q. G. Dai, H. Huang, Y. Zhu, W. Deng, S. X. Bai, X. Y. Wang and G. Z. Lu, *Appl. Catal. B*, 2012, **117**, 360-368.

9 Q. Yuan, H.-H. Duan, L.-L. Li, L.-D. Sun, Y.-W. Zhang and C.-H. Yan, *J. Colloid Interface Sci.*, 2009, **335**, 151-167.

10 W. Huang and Y. Gao, *Catal. Sci. Technol.*, 2014, **4**, 3772-3784.

11 G. Li, R. L. Smith and H. Inomata, *J. Am. Chem. Soc.*, 2001, **123**, 11091-11092.

12 E. Mamontov, T. Egami, R. Brezny, M. Koranne and S. Tyagi, *J. Phys. Chem. B*, 2000, **104**, 11110-11116.

13 N. Shehata, K. Meehan, M. Hudait and N. Jain, *J. Nanopart. Res.*, 2012, **14**.